Advanced Concepts and Functionalities for Symmetry-Broken Photonic Bound States in the Continuum

Lucca Kühner

München 2022

Advanced Concepts and Functionalities for Symmetry-Broken Photonic Bound States in the Continuum

Lucca Kühner

Dissertation
to obtain the doctoral degree of natural sciences (Dr. rer. nat.)
at the Faculty of Physics
of the Ludwig-Maximilians-Universität München

submitted by
Lucca Kühner
from Crailsheim

München, 09/28/2022

First referee: Dr. Andreas Tittl
Second referee: Prof. Dr. Thomas Taubner
Date of oral examination: 11/28/2022

Fortgeschrittene Konzepte und Funktionalitäten für Symmetrie-gebrochene photonisch gebundene Zustände im Kontinuum

Lucca Kühner

Dissertation
zur Erlangung des Doktorgrades der Naturwissenschaften (Dr. rer. nat.)
an der Fakultät für Physik
der Ludwig-Maximilians-Universität München

vorgelegt von
Lucca Kühner
aus Crailsheim

München, den 28.09.2022

Erstgutachter: Dr. Andreas Tittl
Zweitgutachter: Prof. Dr. Thomas Taubner
Tag der mündlichen Prüfung: 28.11.2022

Contents

Zusammenfassung xiii

Abstract xv

1. Introduction 1

2. Fundamentals of photonic bound states in the continuum 5
2.1. Mie theory . . . 5
2.1.1. Maxwell's equations in all-dielectric media . . . 6
2.1.2. Electromagnetic eigenmodes in spherical particles . . . 7
2.1.3. Mie resonances and eigenmodes in non-spherical resonators . . . 11
2.2. Bound states in the continuum . . . 12
2.2.1. Defining features and practical implementations . . . 12
2.2.2. Symmetry-protected BICs . . . 14
2.2.3. Symmetry-breaking and coupling to the continuum . . . 15
2.2.4. Connection between BIC and Fano resonance . . . 18

3. Methodology 21
3.1. General process flow . . . 21
3.2. Numerical simulations . . . 22
3.3. Nanostructure fabrication . . . 25
3.3.1. Substrate cleaning and preparation . . . 25
3.3.2. Material deposition . . . 26
3.3.3. Lithography and liftoff . . . 28
3.3.4. Reactive ion etching and hard mask removal . . . 30
3.3.5. 2D material transfer . . . 31
3.4. Optical characterization . . . 32
3.4.1. Confocal white light microscopy . . . 32
3.4.2. Chiral white light measurements . . . 34
3.4.3. Nonlinear measurements . . . 35
3.5. Data analysis . . . 35
3.5.1. Temporal coupled mode theory . . . 35

4. Radial bound states in the continuum for polarization-invariant nanophotonics 39
4.1. Numerical investigation and experimental realization . . . 40
4.1.1. State of the art and advantages of the radial arrangement . . . 40
4.1.2. Full experimental characterization of radial BICs . . . 43

4.2. Biomolecular sensing using radial BICs 49
4.2.1. Refractive index sensitivity 49
4.2.2. Biomolecular sensing performance 52
4.3. Radial BIC-enhanced second harmonic generation 53
4.3.1. Introduction to nonlinear optics 53
4.3.2. Estimation of the SHG enhancement 54
4.3.3. Experimental results 56

5. Unlocking the out-of-plane dimension for photonic bound states in the continuum to achieve maximum optical chirality 63
5.1. Height-driven linear qBICs 64
5.1.1. Analytical description and numerical simulation of height-driven qBICs 64
5.1.2. Experimental demonstration of out-of-plane symmetry breaking 68
5.2. Chirality in nanophotonics 71
5.3. Chiral qBIC metasurfaces 72
5.3.1. Description and implementation of chiral qBICs 72
5.3.2. Optical characterization of chiral qBICs 75

6. Hexagonal boron nitride metasurfaces for low refractive index bound states in the continuum 85
6.1. Introduction to 2D materials 86
6.1.1. Lattice and electronic properties of hexagonal boron nitride . . 87
6.2. Symmetry-broken BICs in hexagonal boron nitride 88
6.2.1. Numerical investigation of low-index based BIC resonator systems 90
6.2.2. Spectral tunability of hBN-based BIC metasurfaces 96
6.2.3. Enhanced second harmonic generation 99

7. Summary and outlook 103

Appendix 104

A. Nature publisher permission 105

Bibliography 107

Acknowledgements 118

List of Figures

1.1. Size overview in the (sub-)nano- and micro-world 2

2.1. Illustration of the electromagnetic scattering problem 8
2.2. Contribution of the spherical eigenmodes to the scattering spectrum . . 10
2.3. Electromagnetic eigenmodes in particles with different geometries . . . 11
2.4. Bound state in the continuum in a potential well 13
2.5. Overview of different BIC platforms 14
2.6. Prominent examples of symmetry-broken BICs 15
2.7. Symmetry-breaking induced by the incidence angle 16
2.8. C_{2z} symmetry breaking mechanisms 17
2.9. Geometrical symmetry breaking in BIC metasurfaces 18
2.10. Collapse to a Fano resonance 19

3.1. General methodology for research projects 22
3.2. Schematic setup for numerical simulations 24
3.3. Silicon ellipsometry data 25
3.4. Fabrication overview 26
3.5. Material deposition techniques 27
3.6. Mechanical exfoliation process for 2D materials 28
3.7. Fabrication I 29
3.8. Fabrication II 30
3.9. Dry-transfer of 2D materials 31
3.10. Identification of TMDC monolayers 32
3.11. Confocal white light transmission setup 33
3.12. Transmittance data normalization 33
3.13. Optical setup for the characterization of chiral samples 34
3.14. Optical setup for nonlinear measurements 35
3.15. Temporal coupled mode theory for resonant metasurfaces 36

4.1. Conceptual advantages of the radial BIC 41
4.2. Advances of the annular unit cell arrangement 42
4.3. Spectral and near-field investigation of the radial BIC mode 43
4.4. Transmittance spectra for different radial BIC asymmetries 44
4.5. Simulated spectral radial BIC responses for different radii 45
4.6. Geomtrical sweep of radial BIC parameters I 46
4.7. Geomtrical sweep of radial BIC parameters II 47
4.8. Radial BIC polarization invariance 48
4.9. Proof polarization invariance 48

4.10. Refractive index sensing 50
4.11. Simulated refractive index sensitivity 51
4.12. Molecular biosensing with radial BICs 52
4.13. Principle of SHG 54
4.14. Estimation of the electric energy and SHG 55
4.15. SHG from a $MoSe_2$ monolayer 56
4.16. Radial BIC-enhanced SHG in an $MoSe_2$ monolayer 57
4.17. Excitation polarization dependent SHG maps 58
4.18. SHG reference measurement with symmetric structures 59
4.19. SHG from pure silicon 60

5.1. Height-driven qBICs 66
5.2. Field enhancements for sub-nm asymmetries 67
5.3. Fabrication principle 68
5.4. SEM micrographs for a two-step lithography process 69
5.5. Numerical investigation of resonator shifts in the unit cell 69
5.6. Experimental characterization of height-driven linear qBICs 70
5.7. Exemplary chiral structure 71
5.8. Maximally chiral BIC metasurface 73
5.9. Numerical simulation of the reflectance spectrum 75
5.10. Optical characterization of the achiral structure 76
5.11. Optical characterization of the left- and right-handed enantiomer . . . 77
5.12. Co- and cross-polarized transmittances for different diverging angles θ . 78
5.13. Lorentz reciprocity 79
5.14. Experimental tuning of the chirality 80
5.15. Comparison between experiment and numerical simulations 81
5.16. Ellipticity check of the circular polarization 82

6.1. 2D materials for nanophotonics 87
6.2. Lattice properties and band-gap energy in bulk hBN 88
6.3. Hexagonal boron nitride metasurfaces for high-Q resonances in the visible 91
6.4. Theoretical analysis of low-index resonators for qBIC metasurfaces . . . 92
6.5. Near-field and decay lengths for low- and high-index based resonators . 93
6.6. Near-field properties for different resonator refractive indices 94
6.7. Design constraints and resonance scaling to the IR 95
6.8. Experimental realization of symmetry-broken qBIC metasurfaces in bulk hBN 97
6.9. Experimental flexibility of hBN-based qBIC metasurfaces 98
6.10. Numerical investigation of BIC-enhanced hBN-intrinsic SHG 99
6.11. Experimental demonstration of BIC-induced SHG enhancement in bulk hBN 100

List of Abbreviations

AFM	Atomic force microscopy
BIC	Bound state in the continuum
BRIS	Bulk refractive index sensitivity
CMT	Coupled mode theory
FDTD	Finite difference time domain
FEM	Finite element method
FOM	Figure of merit
FWHM	Full width at half maximum
hBN	Hexagonal boron nitride
IR	Infrared
LCP	Left circularly polarized
NIR	Near-infrared
OAM	Optical angular momentum
PL	Photoluminescence
qBIC	Quasi bound state in the continuum
RCP	Right circularly polarized
RCWA	Rigorous coupled-wave analysis
RIU	Refractive index unit
ROI	Range of interest
SEM	Scanning electron microscopy
SHG	Second harmonic generation
TCMT	Temporal coupled mode theory
TMDC	Transition metal dichalcogenide
UV	Ultraviolet
vdW	Van der Waals

Zusammenfassung

Das grundlegende Ziel der Nanophotonik ist die Kontrolle und räumliche Konzentration von Licht auf der Nanoskala. Seit kurzem sind dielektrische Materialsysteme in Erscheinung getreten, da sie nicht durch Materialverluste eingeschränkt sind und die Kontrolle der radiativen Lebensdauern von optischen Resonanzen ermöglichen. Dabei sind photonisch gebundene Zustände im Kontinuum (BICs, *englisch: Bound states in the continuum*) entscheidend für die Kontrolle der radiativen Lebensdauern in dielektrischen Metaoberflächen (MO). Insbesondere symmetriegebrochene BICs zeichnen sich durch die Korrelation zwischen der radiativen Lebensdauer dieser Resonanzen und der geometrischen Störung der MO aus und ermöglichen dadurch die Einstellung der Licht-Materie-Wechselwirkung. Bislang sind diese Zustände meist auf den infraroten Spektralbereich beschränkt und erfordern große räumliche Ausdehnungen.
Diese Arbeit zielt darauf ab, die Grenzen von BIC-MO neu zu definieren, indem die räumliche Ausdehnung der BIC-Plattform erheblich reduziert wird, neue Spektralbereiche durch die Nutzung von Materialien mit niedrigem Brechungsindex als Resonatorkomponenten erforscht werden und neue Funktionalitäten wie chiral selektive Antworten durch die Realisierung von MO mit individueller Höhenkontrolle der Resonatoren erreicht werden.
Im ersten Teil wird gezeigt, wie die geometrische Grundfläche der BIC-Plattform durch ringförmige Anordnung der MO-Einheitszellen um eine Größenordnung verkleinert wird. In Einklang damit wird gezeigt, wie die Güte der Resonatoren (Q-Faktor) erhöht wird. Dadurch steigt die Licht-Materie-Wechselwirkung an, was zu einer höheren biomolekularen Empfindlichkeit, sowie eine verbesserten Erzeugung der zweiten Harmonischen (SHG) aus einer Molybdändiselenid-Monolage führt.
Im zweiten Teil wird ein neuartiger Fabrikationsansatz gezeigt, der die Realisierung einer dielektrischen MO mit voller Höhenkontrolle der einzelnen MO-Elemente ermöglicht. Dadurch wird die Höhe zu einem zusätzlich verfügbaren MO-Parameter und wird genutzt, um Symmetriebrechungen außerhalb der Ebene für BIC-MO einzuführen. Es wird anhand dessen gezeigt, wie zwei unkorrelierte Funktionalitäten wie die Kopplung an zirkular polarisiertes Licht und die Resonanz-Güte unabhängig voneinander innerhalb einer einzigen MO angepasst und implementiert werden können.
Im dritten Teil wird gezeigt, wie Strahlungsverluste in Materialien mit niedrigem Brechungsindex durch Nutzung des BIC-Konzepts wirksam unterdrückt werden, was Resonanzen mit hoher Güte im gesamten sichtbaren Spektralbereich ermöglicht. Insbesondere wird der Einfluss von Resonatormaterialien mit niedrigem Brechungsindex auf die BIC-Resonanzen numerisch untersucht und erklärt, wie das BIC-Konzept die Nutzung von Materialien mit niedrigem Brechungsindex im Allgemeinen ermöglicht. Für die experimentelle Umsetzung wird hexagonales Bornitrid (hBN), das Rückgrat

der zweidimensionalen Materialforschung, als Resonatormaterial verwendet. Durch die Nutzung der großen Bandlückenenergie von hBN kann die feine Einstellung der BIC-verstärkten SHG im ultravioletten Spektralbereich demonstriert werden.
Die in dieser Arbeit vorgestellten Ergebnisse können somit den Bereich der 2D-Materialien mit der Nanophotonik durch den Vorschlag von hBN als Resonatormaterial vereinen. Darüber hinaus kann auch die Lücke zwischen verschiedenen Forschungsbereichen von MO geschlossen werden, um hybride und multifunktionale MO herzustellen.

Abstract

The fundamental goal of nanophotonics is the control and spatial concentration of light at the nanoscale. Recently, all-dielectric material systems have emerged since they are not limited by material losses and allow for the control of the radiative resonance lifetimes. Photonic bound states in the continuum (BICs) are instrumental for tailoring the radiative lifetimes in all-dielectric metasurfaces. In particular, symmetry-broken BICs stand out for the direct correlation between the radiative lifetimes of the resonance and the geometrical metasurface perturbations, providing direct access for the flexible tuning of light-matter interactions. So far, these peculiar states are mostly limited to the infrared spectral range and crucially require large spatial footprints.
This thesis aims to redefine the boundaries of BIC metasurfaces by significantly reducing the spatial footprint of the BIC platform, exploring new spectral regimes by harnessing low refractive index materials as resonator components, and accessing new functionalites, such as chirally selective responses, by realizing metasurfaces with individual resonator height control.
In the first part, the physical concept of symmetry-broken BICs is theoretically introduced along with the utilized methodology employed in this thesis. The concept is leveraged to drastically shrink the geometrical footprint of the BIC platform by one order of magnitude via arranging the metasurface unit cells in an annular fashion. In line with that, it is shown how the resonance quality (Q) factors are increased, boosting the light-matter interaction in terms of higher biomolecular sensitivity and enhanced second harmonic generation (SHG) from a monolayer of molybdenum diselenide.
In the second part, a novel fabrication approach is shown that allows for the realization of all-dielectric metasurfaces with full height control over individual metasurface elements, rendering the height an additionally available metasurface parameter. This degree of freedom is employed to introduce out-of-plane symmetry-breaking for BIC metasurfaces and it is demonstrated how two unrelated metasurface functionalities, such as the coupling to circularly polarized light and the resonance Q factor, can be tailored independently within a single metasurface.
In the third part, the efficient suppression of radiative losses in low refractive index materials is shown by exploiting the BIC concept, enabling high-Q resonances throughout the complete visible spectral range. In particular, the impact of low-index resonator materials on the BIC resonances is numerically studied and it is explained how the BIC concept enables the utilization of low-index materials in general. For the experimental realization, hexagonal boron nitride (hBN), the backbone of two-dimensional materials research, is utilized as resonator material. Using the large band-gap energy of hBN, fine control over the BIC-enhanced SHG in the ultraviolet spectral range is demonstrated.

The results presented in this thesis could thus merge the field of 2D materials with nanophotonics via the proposal of hBN as resonator material but also bridge the gap between different metasurface research areas to realize hybrid and multi-functional metasurfaces.

1. Introduction

Understanding the nature of light and controlling all its properties is a key question in modern optics and technology. As such, light plays a paramount role for the transmission of information and has found many applications for communication [1, 2, 3], enables nanoscale fabrication [4] and characterization [5], and provides information about matter that interacts with it [6, 7]. Following this path, light is a unique tool to non-invasively detect the presence of biologically relevant entities, such as bacteria [8], viruses [9], or drug molecules [10]. One major roadblock for the detection of such nanometer-sized objects with light is the optical diffraction limit, which sets a lower boundary for its spatial concentration to half the wavelength, commonly hundreds of nanometers. Inevitably, most of the detection species of interest are more than one order of magnitude smaller than the wavelength of light (see Fig. 1.1). Due to this large size mismatch, the interaction of light with such nanometer-sized objects is small, rendering their detection highly inefficient and limiting it to large amounts of specimen.

One way to effectively concentrate and confine light at a few nanometer length-scale is the utilization of nanoparticles with sub-wavelength sizes. Generally, either metallic or all-dielectric nanoparticles are employed although they rely only fundamentally different physical mechanisms. For metal-based systems, the incident light excites collective oscillations of the quasi-free conduction electrons, so called plasmons or plasmonic resonances [12]. On the contrary, for all-dielectric resonators, the incident light resonantly drives nanoscopic displacement currents inside the particle [13]. For both cases, the incident far-field radiation is transduced into highly enhanced and localized near fields which tremendously increase the interaction between light and nanoscale objects in the vicinity of these resonators.

Although metallic systems exhibit better light confinement, they are, beneath the radiative losses, hampered by the Ohmic losses of the quasi-free conduction electrons. Metal-based resonators hence store the energy less efficiently and provide broader resonances, characterized by smaller quality (Q) factors

$$Q = \frac{\text{Resonance frequency}}{\text{Resonance linewidth}}. \tag{1.1}$$

All-dielectric materials provide purely photonic excitations and thus enable an operation without any material-intrinsic losses. Since these materials are solely limited by radiative losses, they can exhibit larger Q factors, potentially leading to higher specimen sensitivities [14]. As a result, all-dielectric material systems have attracted much interest and hold great promise to outperform metal-based systems.

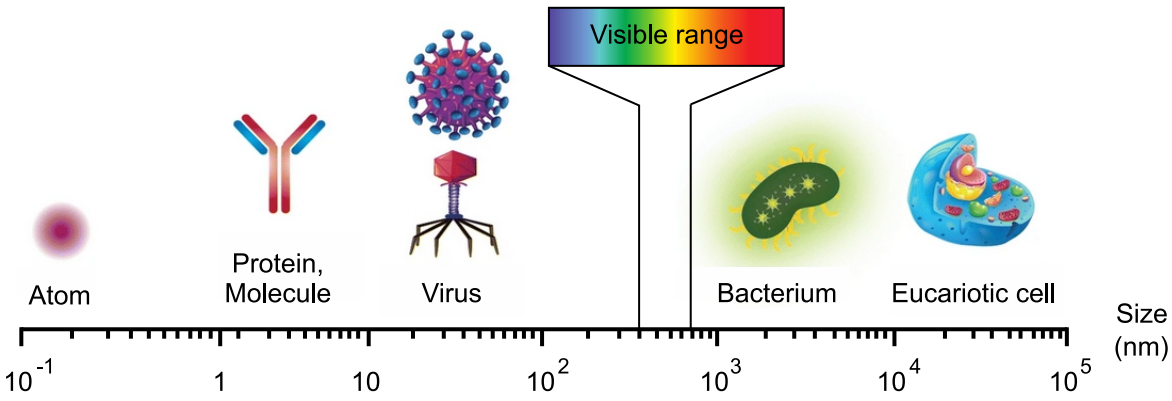

Figure 1.1.: Size overview in the (sub-)nano- and micro-world. Size comparison between the wavelength of visible light and nanometer-sized objects including viruses, DNA, proteins, and atoms but also larger objects, such as bacteria or eucariotic cells. Adapted under the terms of the CC-BY Creative Commons Attribution 4.0 International license `http://creativecommons.org/licenses/by/4.0/` [11].

In particular, bound states in the continuum (BICs) in all-dielectric materials are appealing owing to their straightforward control over the radiative losses [15, 16, 17]. Since all-dielectric resonator systems only suffer from radiative losses, BICs provide a unique toolkit to tailor the total Q factor of the resonance, enabling the realization of high-Q resonances. Most often, these peculiar states are realized in so-called optical metasurfaces, a spatial arrangement of resonators with sub-wavelength periodicities and dimensions [18, 19]. Mediated by this sub-wavelength arrangement, metasurfaces can exhibit artificial functionalities, that are not present in nature, such as a negative optical refraction [20]. Similarly, light can be perfectly trapped in an open resonator system in the case of BIC metasurfaces [21].

Even though BICs can be implemented through different mechanisms including strong mode coupling in sub-wavelength discs [22, 23], vertical dipolar modes in periodic arrays [25], and accidental destructive mode interference [26, 24], symmetry-broken BICs have garned special interest [15, 27, 28]. In particular, symmetry-broken BICs are attractive through the tailorable coupling of the photonic mode to the far field promoted by a geometric perturbation of the unit cell geometry [15]. While the unperturbed system corresponds to a dark BIC state with infinite lifetimes, the geometric perturbation unlocks the coupling to the far field, transforming the BIC into a quasi-BIC (qBIC), and controls the Q factor of the mode. Although the platform has already shown promising applications, *i.e.*, enhanced biomolecular sensitivity [28, 27], improved nonlinear effects [29, 30, 31], and emission control [32, 33], fundamental questions related to the spatial extent and multi-functional operation are still unanswered. This thesis aims to tackle three fundamental physical limitations and questions of the concept.

Chapter 2 comprises the the theoretical foundations of symmetry-broken BICs after introducing Mie theory for spherical particles. The derivations and explanations of the concept mainly focus on symmetry considerations for the introduction of the fundamental defining properties. In particular, the geometrical symmetry breaking mechanism will be analyzed and explained in detail.

Chapter 3 introduces the general methodology of this thesis with an emphasis on the complex fabrication schemes, including the well-established nanostructuring of traditional materials using electron beam lithography. Additionally, the extraction and combination of atomically thin two-dimensional (2D) materials is explained, utilizing mechanical exfoliation and a dry-transfer technique. Apart from the metasurface fabrication, the numerical simulation approach including the finite element method is explained before the data analysis for the determination of the resonance Q factors is introduced based on coupled mode theory. Finally, the optical setups, which are employed to characterize the metasurface responses with linear and circular excitation polarization, are explained along with the optical setup for the examination of nonlinear optical effects.

Chapter 4 investigates the physical limitations of symmetry-broken BICs and overcomes the stringent requirements on large spatial extents. Since symmetry-broken BICs are extended states, they rely on large geometrical footprints in two-dimensional metasurfaces. In fact, the Q factor of the qBIC even increases with the number of resonator elements [26, 34] related to a better mode coupling and formation, hindering miniaturization and on-chip integration. Within chapter 4, a superior approach for realizing symmetry-broken BIC metasurfaces is proposed by arranging the metasurface in a ring fashion. Aided by the semi-infinite arrangement, it is shown how this concept boosts the resonance Q factor and provides highly enhanced light-matter interaction, all within a footprint of 2 μm^2, down to 12 unit cells.

Chapter 5 demonstrates how to overcome the fabrication constraints of all-dielectric metasurfaces to planar structures, rendering them intrinsically achiral. Nevertheless, the efficient control and manipulation of the helicity of light is of utmost importance in quantum computing [35] but also for chiral light generation [32] and displays [36]. This chapter demonstrates how, by exploiting the individual height of metasurface elements, all-dielectric BIC metasurfaces become intrinsically chiral and introduces out-of-plane symmetry breaking for BIC platforms. In this context, the height parameter is leveraged to encode and control two independent metasurfaces responses, *i.e.*, the resonance Q factor and the coupling to circularly polarized light. Since metasurface are so far mostly limited to single applications, accessing this degree of freedom sparks hope for the realization of multi-functional and hybrid metasurfaces.

Chapter 6 addresses a fundamental nanophotonic problem, in particular, the lack of lossless and high refractive index materials in the visible range [37, 38], hampering the light-matter interaction and flat optics throughout this spectral regime. Due to the invincible correlation between the band-gap energy and the refractive index of a medium [39, 40], the utilization of low refractive index materials is unavoidable for a lossless operation in the visible. However, resonances from low refractive index materials are always associated with smaller Q factors and larger mode volumes [41]. Chapter 6 demonstrates how, through using symmetry-broken BIC metasurfaces, the radiative losses in low refractive index materials can be efficiently suppressed. Following this approach, it is shown how hexagonal boron nitride (hBN) can be leveraged for the realization of high-Q resonances throughout the complete visible spectral range.

Since hBN is the backbone of 2D materials research, it is the ideal material to provide enhanced light-matter interaction in nanostructured van der Waals (vdW) metasurfaces through the complete visible spectral regime.

Overall, this thesis provides a valuable toolkit for the implementation of the BIC concept in new material platforms and the expansion to novel functionalities with high potential for on-chip integration provided by the drastically reduced spatial footprint. On the one hand, the demonstration of hBN-based BIC metasurfaces in the visible is fundamental for quantum optics since hBN hosts room-temperature single photon sources in this spectral regime [42, 43]. As a result, BIC resonances that couple to these single photon emitters can improve the yield and indistinguishability of the single photons and thus set a milestone towards fully integrated hBN quantum circuits. Furthermore, initiated by the combination affinity of hBN with other 2D materials, this approach opens up a unique avenue for the straightforward implementation of vdW heterostructure meta-optics.

On the other hand, the demonstration of a height-driven BIC platform unlocks an additional design degree of freedom for metasurfaces in general and has high potential for the implementation of multi-functional and hybrid metasurfaces. In particular, this concept could play a major role for the unification of local and non-local metasurfaces, enabling wavefront control while providing high-Q resonances, for instance.

Finally, the drastically reduced spatial footprint through the annular arrangement of metasurface building blocks eases the on-chip integration of the concepts above. The low spatial footprint is especially appealing for multiplexed sensing applications, enabling the realization of sharp filters in compact footprints for flat optics or point-of-care devices for early disease detection and treatment.

2. Fundamentals of photonic bound states in the continuum

The following chapter presents the theoretical framework underpinning photonic bound states in the continuum based on classical electromagnetic theory. As such, the derivations and explanations within this chapter follow the relevant textbooks and review papers or are directly taken from Ref. [44, 45] and Refs. [16, 15].

For the full comprehension of bound states in the continuum (BICs) in all dielectric media, it is first necessary to gain a deeper understanding of the underlying electric and magnetic modes that exist within spherical resonators. The characteristic eigenmodes constitute a series of electric and magnetic multipoles that individually contribute to the spectral response of the particle. Indeed, these modes are not constrained to spherical particles and play a vital role for the formation of BICs in all-dielectric metasurfaces. Here, symmetry arguments and conservation laws are utilized to derive an intuitive understanding of symmetry-broken quasi BICs and how they collapse to Fano resonances. Finally, the geometrical symmetry-breaking of BIC metasurfaces is explained along with prominent unit cells from the literature.

2.1. Mie theory

In order to understand the formation and existence of electromagnetic modes in all-dielectric media, especially particles, it is insightful to explore Maxwell's equations and derive solutions for the constituent electric and magnetic fields. In 1908, Gustav Mie derived exact analytical solutions for spherical particles with dimensions on the order of the wavelength of the incident light. In particular, he found that a set of eigenmodes with electric and magnetic character are excited by the incident fields within these particles. Furthermore, he could show that the scattering and extinction of the incident field by these particles is composed of contributions from the magnetic and electric eigenmodes [46] inside these particles. For the first time, Gustav Mie could unify the different regimes of light interaction with particles, namely Rayleigh scattering for comparably small objects and geometric optics for large particles with regard to the wavelength of the incident light. Based on these analytical derivations, the full concept and existence of electric and magnetic modes in sub-wavelength particles can be understood and described without the constraint to spherical particles. As a matter of fact, these eigenmodes exist in non-spherical geometries as well, indicating why it is worth to studying and understanding Mie scattering in detail.

2.1.1. Maxwell's equations in all-dielectric media

Starting with Maxwell's macroscopic and electrostatic equations in homogeneous media, the electric displacement field $\boldsymbol{D}$[1] can be derived, that is generated by an ensemble of charges with charge density ρ. For all-dielectric particles, electrical charges are absent ($\rho = 0$) and the equations thus read

$$\nabla \cdot \boldsymbol{D} = \rho = 0, \tag{2.1a}$$

$$\nabla \cdot \boldsymbol{B} = 0, \tag{2.1b}$$

with the magnetic field $\boldsymbol{B}$. The electric displacement field $\boldsymbol{D}$ includes the macroscopic electric polarization $\boldsymbol{P}$ within the sphere via

$$\boldsymbol{D} = \varepsilon_0 \boldsymbol{E} + \boldsymbol{P}, \tag{2.2a}$$

$$\boldsymbol{B} = \mu_0(\boldsymbol{H} + \boldsymbol{M}) = \mu_0 \boldsymbol{H}, \tag{2.2b}$$

with μ_0 and ε_0 being constants. Here, $\boldsymbol{B}$ includes the magnetization $\boldsymbol{M}$ within the material, which will be neglected in the discussion since the derivation is constrained to non-magnetic media ($\boldsymbol{M} = \boldsymbol{0}$). Furthermore, by considering isotropic and linear media, the simplified constitutive equation for the electric polarization can be written as

$$\boldsymbol{P} = \varepsilon_0 \chi_e \boldsymbol{E}, \tag{2.3a}$$

leading to

$$\boldsymbol{D} = \varepsilon_0 \boldsymbol{E} + \boldsymbol{P} = \varepsilon_0(1 + \chi_e)\boldsymbol{E} = \varepsilon_0 \varepsilon \boldsymbol{E}, \tag{2.3b}$$

where the electric permittivity is defined as $\varepsilon = 1 + \chi_e$. If dynamic fields are considered in the absence of any sources ($\boldsymbol{j} = \rho = 0$), Faraday's and Ampere's law can be written as

$$\nabla \times \boldsymbol{E} = -\frac{\partial \boldsymbol{B}}{\partial t}, \tag{2.4a}$$

$$\nabla \times \boldsymbol{H} = \frac{\partial \boldsymbol{D}}{\partial t}. \tag{2.4b}$$

By combining eq. 2.4a and 2.4b and using a mathematical trick [45], the wave equation in a homogeneous and linear medium is obtained for magnetic and electric field as

$$\nabla^2 \boldsymbol{E} - \frac{1}{c^2}\frac{\partial^2 \boldsymbol{E}}{\partial t^2} = 0 \qquad \nabla^2 \boldsymbol{H} - \frac{1}{c^2}\frac{\partial^2 \boldsymbol{H}}{\partial t^2} = 0 \tag{2.5}$$

By considering time harmonic fields $\boldsymbol{E}(\boldsymbol{r}, t) = \boldsymbol{E}(\boldsymbol{r}) \cdot e^{-i\omega t}$ with frequency ω, the Helmholtz equations for the magnetic and electric are written as

$$\left[\nabla^2 + k^2\right] \boldsymbol{E} = 0 \qquad \left[\nabla^2 + k^2\right] \boldsymbol{H} = 0, \tag{2.6}$$

with the light wavenumber defined as $k = \frac{\omega}{c_0}\sqrt{\varepsilon}$ and c_0 is the speed of light in vacuum.

[1] Vectors are written in bold font.

2.1.2. Electromagnetic eigenmodes in spherical particles

One of the simplest systems to study the existence of electromagnetic modes in sub-wavelength particles is a sphere with a given radius R and refractive index n_1. The common situation is depicted in Fig. 2.1 where a plane wave with electric $\boldsymbol{E}_{\text{inc}}$ and magnetic $\boldsymbol{H}_{\text{inc}}$ field is incident on the sphere. The incident field will excite electric $\boldsymbol{E}_{\text{int}}$ and magnetic $\boldsymbol{H}_{\text{int}}$ fields that are associated with these modes. The excited modes will radiate themselves causing the incident fields to be scattered $\boldsymbol{E}_{\text{scat}}$ and $\boldsymbol{H}_{\text{scat}}$ into arbitrary directions. To characterize the spectral response of the sphere, the extinction cross section is defined as

$$\sigma_{\text{ext}}(\omega) = \sigma_{\text{scat}}(\omega) + \sigma_{\text{abs}}(\omega), \tag{2.7}$$

composed of the scattering cross section $\sigma_{\text{ext}}(\omega)$ that captures the scattered power to all solid angles of the incident fields and the absorption cross section $\sigma_{\text{abs}}(\omega)$ which is a measure of the absorbed power within the particle. In order to find the electromagnetic solutions, the Helmholtz equations in eq. 2.6 need to be solved while the solutions need to satisfy Maxwell's equations 2.1a and 2.1b as well as 2.4a and 2.4b. Since the given Helmholtz equations are vectorial and thus difficult to solve, it is beneficial to introduce a scalar field ψ which generates a set of three orthogonal vector fields

$$\boldsymbol{L} = \nabla\psi, \tag{2.8a}$$

$$\boldsymbol{M} = \nabla \times (\boldsymbol{a}\psi), \tag{2.8b}$$

$$\boldsymbol{N} = \frac{1}{k}(\nabla \times \boldsymbol{M}), \tag{2.8c}$$

termed the vector spherical harmonics. It can be easily shown that all of these vector fields satisfy the vectorial wave equation if ψ obeys the scalar wave equation

$$\nabla^2\psi + k^2\psi = 0. \tag{2.9}$$

Beneficially, by solving the wave equation for the scalar field ψ, the associated vector fields $\boldsymbol{L}$, $\boldsymbol{M}$, and $\boldsymbol{N}$, that constitute a basis for the construction of any arbitrary electric $\boldsymbol{E}$ and magnetic fields $\boldsymbol{H}$, can be deduced. Moreover, as the scattering object is spherical, it is convenient to utilize spherical coordinates that obey the symmetry of the system. The scalar wave equation in spherical coordinates is then given by

$$\underbrace{\frac{1}{r^2}\frac{\partial}{\partial r}\left(r^2\frac{\partial\psi}{\partial r}\right)}_{\text{radial part } r} + \underbrace{\frac{1}{r^2\sin\theta}\frac{\partial}{\partial\theta}\left(\sin\theta\frac{\partial\psi}{\partial\theta}\right)}_{\text{azimuthal part } \theta} + \underbrace{\frac{1}{r^2\sin\theta}\frac{\partial^2\psi}{\partial\varphi^2} + k^2\psi}_{\text{polar part } \varphi} = 0. \tag{2.10}$$

Apparently, the scalar wave equation can be separated in parts which solely depend on one variable of the spherical coordinates allowing to make the separation ansatz

$$\psi(r,\theta,\varphi) = R(r)\cdot\chi(\theta)\cdot\Upsilon(\varphi). \tag{2.11}$$

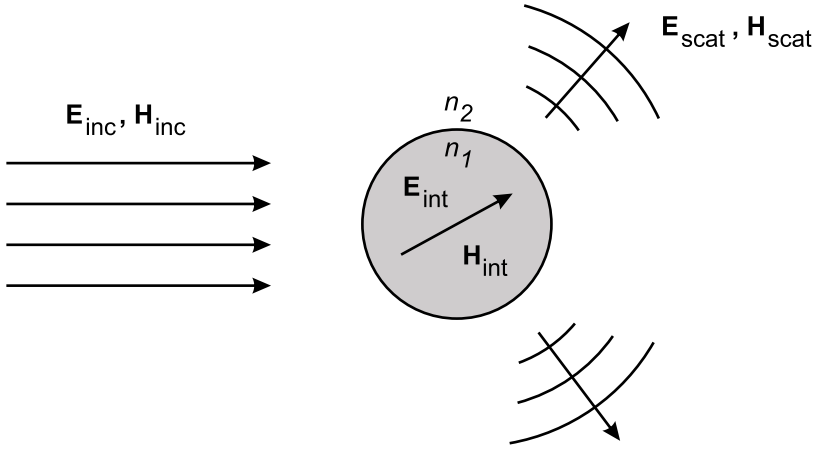

Figure 2.1.: Illustration of the electromagnetic scattering problem. An incident wave with $\boldsymbol{E}_{\text{inc}}$ and $\boldsymbol{H}_{\text{inc}}$ impinges on a small particle where it excites intrinsic electric $\boldsymbol{E}_{\text{int}}$ and magnetic $\boldsymbol{H}_{\text{int}}$ modes. Owing to the excitation of these modes, electric $\boldsymbol{E}_{\text{scat}}$ and magnetic $\boldsymbol{H}_{\text{scat}}$ fields will be scattered in arbitrary directions.

Inserting the separation ansatz into the radial scalar wave equation yields an even part ψ_{emn} and an odd part ψ_{omn} of the scalar function owing to the ambiguous polar solution

$$\psi_{emn} = \cos(m\varphi)\ \mathrm{P}_n{}^m(\cos\,\theta)\ z_n(kr) \tag{2.12}$$

$$\psi_{omn} = \sin(m\varphi)\ \mathrm{P}_n{}^m(\cos\,\theta)\ z_n(kr), \tag{2.13}$$

where $\mathrm{P}_n{}^m$ are the well-known associated Legendre polynomials. Here, $z_n(kr)$ represents the ambiguity of solutions for the radial part, *e.g.*, Bessel functions of first and second kind or any linear combinations of them, such as the spherical Hankel functions. The obtained solutions can be utilized to deduce the vector spherical harmonics as

$$\boldsymbol{M}_{omn} = \nabla \times (\boldsymbol{r}\psi_{omn}) \qquad \boldsymbol{M}_{emn} = \nabla \times (\boldsymbol{r}\psi_{emn}) \tag{2.14}$$

$$\boldsymbol{N}_{emn} = \frac{\nabla \times \boldsymbol{M}_{emn}}{k} \qquad \boldsymbol{N}_{omn} = \frac{\nabla \times \boldsymbol{M}_{omn}}{k}, \tag{2.15}$$

where $\boldsymbol{N}$ is associated as electric while $\boldsymbol{M}$ is associated as magnetic vector spherical harmonic. In order to deduce the scattered and absorbed field, all the fields involved need to be expanded in the basis of the vector spherical harmonics. Owing to the rotational symmetry of the sphere, the incident polarization can be chosen along the x direction and using the orthogonality of the spherical vector harmonics, the expansion of the incident field simplifies to

$$\boldsymbol{E}_{\text{inc}} = \sum_{n=1}^{\infty} \left(B_{o1n}\ \boldsymbol{M}_{o1n}{}^{(1)} + A_{e1n}\ \boldsymbol{N}_{e1n}{}^{(1)} \right), \tag{2.16}$$

where B_{o1n} and A_{e1n} are expansion coefficients and (1) indicates that the radial part of the vector harmonics is composed of spherical Bessel functions of first order.

The decomposition of the scattered field into spherical harmonics is equivalent to the procedure of the incident field. Following this approach, the simplified expression of the scattered field is given by

$$\boldsymbol{E}_{\text{scat}} = \sum_{n=1}^{\infty} i^n E_0 \frac{2n+1}{n(n+1)} \left(i a_n \, \boldsymbol{N}_{e1n}{}^{(3)} - b_n \, \boldsymbol{M}_{e1n}{}^{(3)} \right), \tag{2.17}$$

where a_n and b_n are the expansion coefficients. For the scattered fields, spherical Hankel functions are employed to satisfy the boundary conditions of the problem for large distances away from the sphere. At this point, additional boundary conditions are employed, which state that all tangential components of the electric and magnetic field need to be continuous at the interface between the sphere and the background

$$(\boldsymbol{E}_{\text{inc}} + \boldsymbol{E}_{\text{int}} + \boldsymbol{E}_{\text{scat}}) \times \boldsymbol{e}_r = 0 = (\boldsymbol{H}_{\text{inc}} + \boldsymbol{H}_{\text{int}} + \boldsymbol{H}_{\text{scat}}) \times \boldsymbol{e}_r. \tag{2.18}$$

Using this boundary condition, the Mie scattering coefficients are obtained as

$$a_n = \frac{\tilde{m}\psi_n(\tilde{m}x)\psi_n'(x) - \psi_n(x)\psi_n'(\tilde{m}x)}{\tilde{m}\psi_n(\tilde{m}x)\xi_n'(x) - \xi_n(x)\psi_n'(\tilde{m}x)}, \tag{2.19a}$$

$$b_n = \frac{\psi_n(\tilde{m}x)\psi_n'(x) - \tilde{m}\psi_n(x)\psi_n'(\tilde{m}x)}{\psi_n(\tilde{m}x)\xi_n'(x) - \tilde{m}\xi_n(x)\psi_n'(\tilde{m}x)}, \tag{2.19b}$$

where $x = kR$ is the size parameter, $\tilde{m} = \frac{n_1}{n_2}$ is the ratio of the refractive indices of the two media and $\xi_n(kr) = kr \cdot h_n{}^{(1)}(kr)$ incorporates the spherical Hankel function of first order. Here, prime denotes the derivative of the function with respect to its argument. Although the coefficients look lengthy and complicated, they are extremely powerful since they determine the scattering and extinction spectra of the spherical particle. By remembering the definition of the extinction and scattering cross sections with the Poynting vector $\boldsymbol{S}_{\text{inc}} = \boldsymbol{E}_{\text{inc}} \times \boldsymbol{H}_{\text{inc}}$,

$$\sigma_{\text{ext}} = -\frac{1}{|\boldsymbol{S}_{\text{inc}}|} \int \frac{c}{8\pi} \Re \left(\boldsymbol{E}_{\text{inc}} \times \boldsymbol{H}_{\text{scat}}{}^{*} + \boldsymbol{E}_{\text{scat}} \times \boldsymbol{H}_{\text{inc}}{}^{*} \right) d\boldsymbol{f}, \tag{2.20a}$$

$$\sigma_{\text{scat}} = -\frac{1}{|\boldsymbol{S}_{\text{inc}}|} \int \frac{c}{8\pi} \Re \left(\boldsymbol{E}_{\text{scat}} \times \boldsymbol{H}_{\text{scat}}{}^{*} \right) d\boldsymbol{f}, \tag{2.20b}$$

the expanded fields are inserted in the above equations and integrated over a spherical surface $d\boldsymbol{f}$ which yields the scattering and extinction cross section for spherical particles

$$\sigma_{\text{ext}} = \frac{2\pi}{k_0{}^2} \sum_{n=1}^{\infty} (2n+1) \, \Re \left(a_n + b_n \right), \tag{2.21a}$$

$$\sigma_{\text{scat}} = \frac{2\pi}{k_0{}^2} \sum_{n=1}^{\infty} (2n+1) \left(|a_n|^2 + |b_n|^2 \right). \tag{2.21b}$$

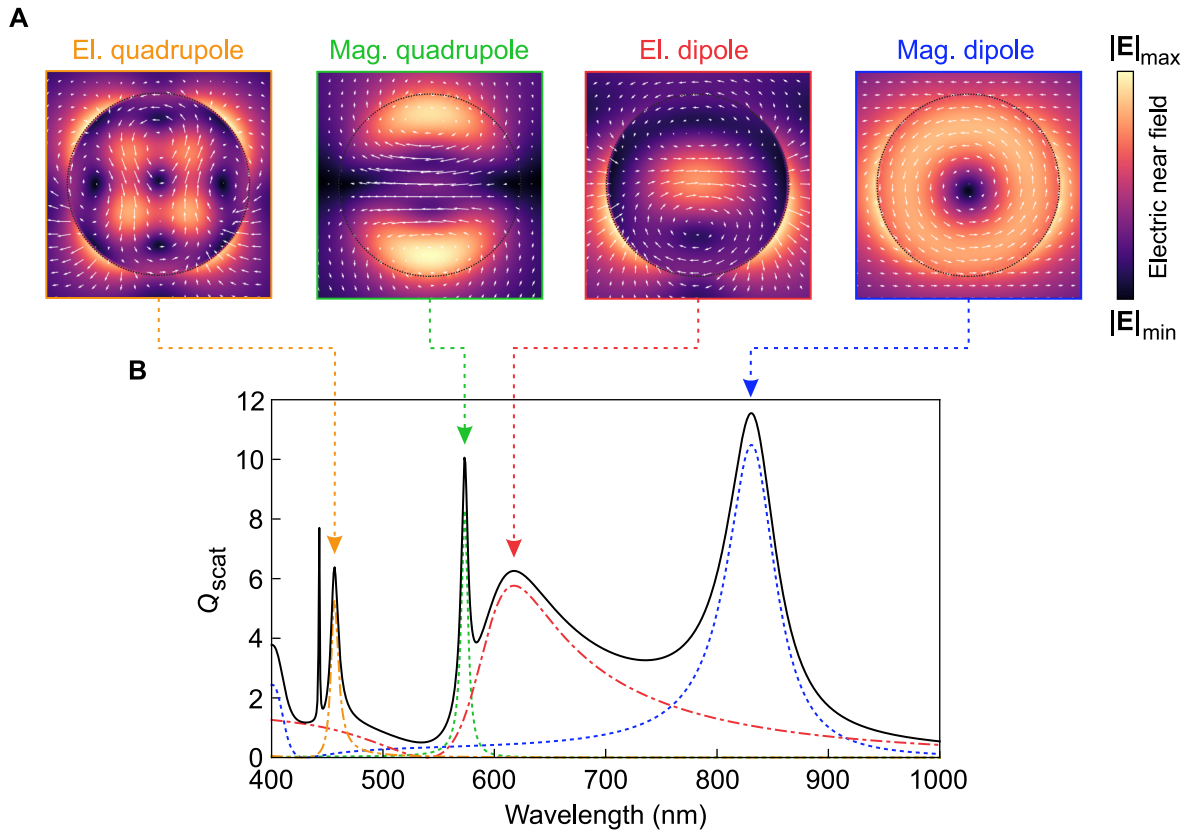

Figure 2.2.: Contribution of the spherical eigenmodes to the scattering spectrum (**A**) Electric and magnetic eigenmodes in a spherical particle up to the second harmonic. (**B**) Normalized scattering cross section from Mie theory for a spherical particle. The contributions of the normal modes are plotted as dashed lines. For the calculation, a refractive index contrast $\tilde{m} = 4$ is assumed with a particle radius of $R = 100$ nm.

The result is intriguing since it shows that, for instance, the scattering cross section is composed of contributions from every harmonic n. The scattering channels can be separated into an electric contribution associated with the coefficients a_n and a magnetic contribution associated with b_n. In essence, the scattering cross section is composed of the sum of the magnetic and electric scattering channel for all harmonics that are excited within the sphere. Fig. 2.2 illustrates the electromagnetic eigenmodes within an all-dielectric spherical subwavelength particle. For simplicity, only electric and magnetic modes up to the second harmonic are considered. The respective contributions from the electric and magnetic eigenmodes can be clearly attributed to the spectral features by selectively considering the respective contribution. As an example, in Fig. 2.2 the scattering cross section σ_{scat} is normalized to the particle's geometrical cross section σ_{geo}

$$Q_{\text{scat}} = \frac{\sigma_{\text{scat}}}{\sigma_{\text{geo}}} = \frac{\sigma_{\text{scat}}}{\pi R^2} \tag{2.22}$$

and plotted for the interesting wavelength regime. Evidently, the scattering cross section is larger than the geometrical cross section at the resonance ($Q > 1$), indicating the ability of the resonant modes to spectrally allocate energy.

2.1.3. Mie resonances and eigenmodes in non-spherical resonators

In contrast to the scattering problem at spherical particles, most of the scattering problems involving different geometrical shapes cannot be solved analytically anymore. For this purpose, numerical solutions of the scattering problem within these geometries are obtained by utilizing finite difference time domain simulations. The structures are excited by a plane wave and their scattering responses are captured and plotted as depicted in 2.3.

Apparently, the obtained numerical scattering spectrum of the spherical particle shows excellent agreement with the analytically obtained result in Fig. 2.2B. Interestingly, the electric and magnetic eigenmodes of the spherical particle do not only exist in spheres but also in other shapes, such as cylinders and cuboids. Albeit the different boundary conditions, they show very similar scattering spectra as depicted in Fig. 2.3 composed of the same eigenmode contributions with slight spectral shifts. Through solving the scattering problem at spherical particles, the obtained eigenmodes can be understood and generalized for a variety of geometries. Fur this purpose, they will serve as constituent modes for the realization of bound states in the continuum, especially in cuboid resonators, which will be discussed in the next section.

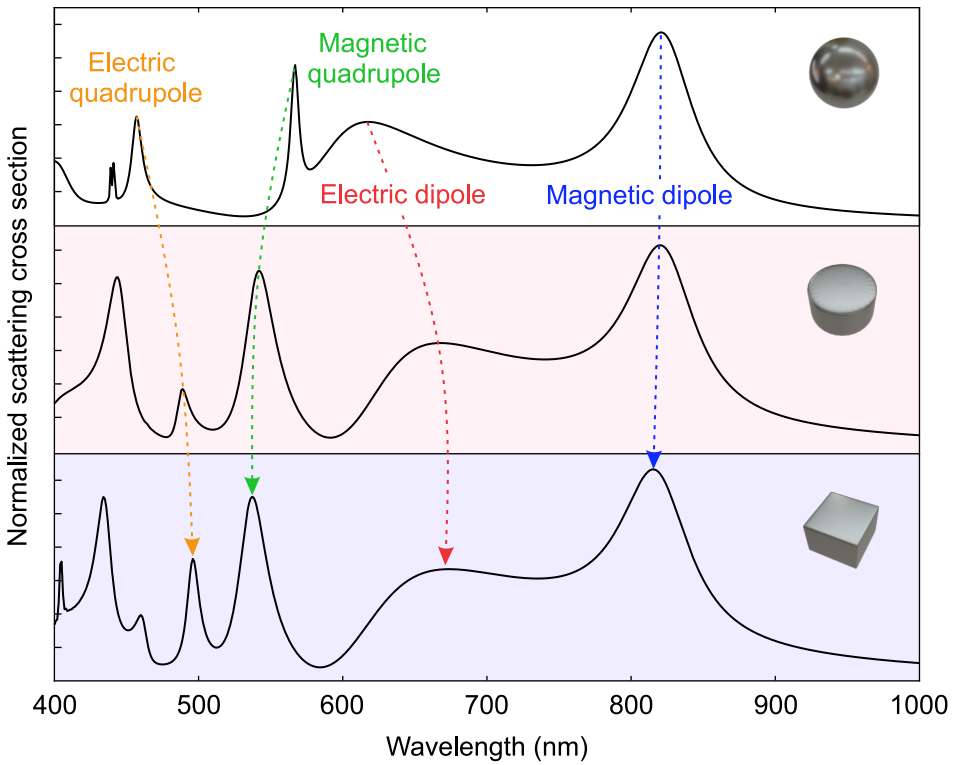

Figure 2.3.: Electromagnetic eigenmodes in particles with different geometries. Numerically obtained and normalized scattering cross sections of a subwavelength sphere (top panel), cylinder (middle panel), and a cuboid (bottom panel) for the same geometrical cross sections. The eigenmodes of the spherical resonator exist equivalently in non-spherical geometries.

2.2. Bound states in the continuum

Within this section, an introduction and overview of the various photonic realizations of bound states in the continuum (BICs) is given with a focus on symmetry broken BICs that are utilized in this thesis. In particular, it will be demonstrated how to confine light perfectly in an open resonator and how to tailor the constituent Mie modes via the perturbation of the unit cell geometry to break this confinement. Along with this, it is explained how BIC resonances are fundamentally linked to Fano resonances. The detailed derivations and explanations can be found in Refs. [16, 15].

2.2.1. Defining features and practical implementations

The confinement of light in optical resonators led to a variety of breakthroughs by effectively increasing the interaction of light with matter in the vicinity of the resonator. One prominent example is the realization of lasers [48], but connections to polariton physics in cavity quantum electrodynamics can also be drawn [49].

Traditionally, light was confined or trapped in closed resonator systems, such as Fabry-Perot cavities consisting of highly reflective mirrors opposing each other. The efficiency of the light trapping is commonly characterized by the Q factor of the resonance, which is just a comparison between the stored energy $h\nu_{\mathrm{res}}$ at the resonance frequency ν_{res} and the energy loss $h\Delta\nu$ with the resonance linewidth $\Delta\nu$

$$Q = \frac{h\nu_{\mathrm{res}}}{h\Delta\nu} = \frac{\nu_{\mathrm{res}}}{\Delta\nu}. \tag{2.23}$$

In the case of closed cavities, the light is trapped due to the reflections at the cavity mirrors, preventing most of the light from leaking. On the contrary, open resonator systems, such as resonances based on bound states in the continuum, have garned widespread interest. These systems are intriguing because they confine light in an open environment, for instance in a photonic crystal slab. In opposite to closed systems, the confinement originates from a destructive interference or suppression of the constituent modes within the slab, leading to a vanishing radiation into the far field with diverging Q factors ($Q \to \infty$).
The phenomenon was first predicted in atomic physics as an eigenvalue embedded in the continuum of freely propagating modes [50]. In this context, the authors designed an artificial potential well that leads to eigenvalues with energies above the potential well, so called bound states in the continuum (see Fig. 2.4). In contrast to leaky modes, the BIC is perfectly localized within the potential well and does not couple to the continuum.

Similarly, in photonics, a bound state in the continuum (BIC) is a photonic dark state which is localized at least in one dimension and is perfectly confined in time ($\Delta\nu = 0$). In analogy to the potential well, a photonic BIC cannot couple to freely propagating far-field modes, explaining why the dark state can neither be excited from the far field nor emit radiation into the far field. Since BICs are a general wave phenomenon, these

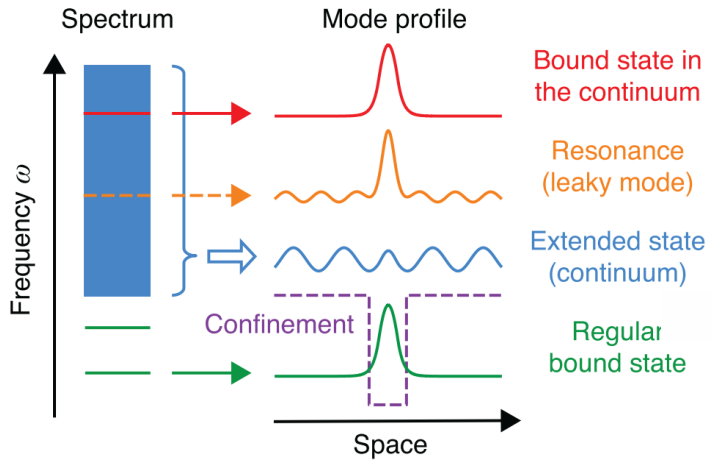

Figure 2.4.: Bound state in the continuum in a potential well. A bound state in the continuum can be realized through tailoring the potential of the well, leading to a bound state within the continuum of freely propagating modes. Adapted with permission [17], Copyright 2016, The authors, published by Springer Nature.

bound states have already been observed as acoustic waves [51, 52], as water waves in ocean science [53], and in nanophotonics [54, 55, 24]. For photonic systems, there are different approaches to realize bound states in the continuum as depicted in Fig. 2.5, which constitute the most relevant systems for this thesis.

Among the systems, three prominent physical mechanisms are differentiated here. First, one of the most prominent approaches comprises **symmetry-protected BICs** (Fig. 2.5A) usually realized in all-dielectric metasurfaces [15] or photonic crystals [56]. Owing to symmetry constraints, which will be discussed in more detail later, these states cannot couple to incident or outgoing plane waves in the normal direction and can thus not radiate energy into the far field.
Apart from the symmetry breaking approach, **accidental BICs** [57, 24] (Fig. 2.5B) exist in periodic structures where, through careful tailoring of the resonator geometry, the emission of the excited modes within individual resonators interferes destructively in the far-field and the radiative losses of the state thus goes to infinity for a certain angle (eventually also the normal direction).
The third prominent approach comprises **single particle BICs** (Fig. 2.5C), which relies on the coupling of electromagnetic modes within a sub-wavelength particle [22, 23]. Commonly, all-dielectric cylindrical resonators are employed for which a Mie mode in the cylindrical plane couples to a Fabry-Perot mode along the cylinder axis [22]. One of the hybridized modes will then exhibit infinite lifetimes initiated by the coupling of the two modes, again, only for precisely configured cylinder geometries.

Owing to the fragility of the accidental BIC and the single particle BIC platform, symmetry-protected BICs pose a major route for achieving highly flexible cavity designs with on-demand tailoring of the resonator lifetimes. Initiated by the robustness of the symmetry-broken BICs, they are chosen as resonator platform in this thesis and will be discussed in more detail.

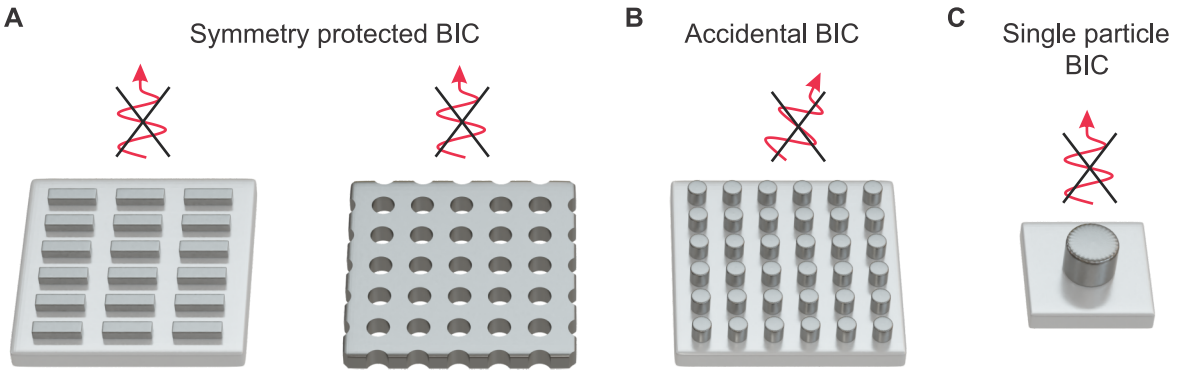

Figure 2.5.: Overview of different BIC platforms. Relevant BIC platforms for this thesis comprise symmetry-protected BICs (**A**), accidental BICs (**B**), and BICs through mode coupling in single resonators (**C**). Apart from the accidental BIC, all BICs cannot emit radiation normal to the sample plane.

2.2.2. Symmetry-protected BICs

The possibilities for designing a symmetry-protected photonic BIC state are vast [47]. A prominent approach to confine light in open resonator systems is by tailoring the mode structure $E_{x,y}$ of a resonant mode within the metasurface unit cell, such that the general coupling amplitude $D_{x,y}$ of the resonant mode to plane-waves vanishes [15]

$$D_{x,y}(k) = -\frac{k}{2\sqrt{S_0}} \int \underbrace{E_{x,y}(\boldsymbol{r'})}_{\text{Mode symmetry}} \cdot \left[\varepsilon(k, \boldsymbol{r'}) - 1\right] \cdot \underbrace{e^{i\boldsymbol{k}\boldsymbol{r'}}}_{\text{Incidence angle}} d\boldsymbol{r'}. \tag{2.24}$$

To reach this condition, two constraints regarding the mode symmetry and the incidence angle need to be fulfilled. First, a periodic arrangement of resonators as depicted in Fig. 2.6A is needed, which is at least periodic in one dimension. By virtue of Noether's theorem [58], the inherent translational invariance of the periodic arrangement requires the in-plane momentum of the incident light to be conserved. In case of normally incident light, the in-plane momentum is zero, commonly known as the Γ-point in reciprocal space. Consequently, normally incident light can only couple to modes that exist at the Γ-point within the periodic structure and vice versa.
Second, the resonant mode and the plane wave both necessarily need to belong to the same symmetry class. The mode coupling amplitude D_x between the normally incident plane wave $\boldsymbol{E}_{\text{inc}} = \boldsymbol{e_x} e^{-ikz'}$ polarized in x-direction and the resonant mode E_x is then given by

$$D_x(k) = -\frac{k}{2\sqrt{S_0}} \int d\boldsymbol{r'} \left[\varepsilon(k, \boldsymbol{r'}) - 1\right] E_x(\boldsymbol{r'}) e^{ikz'}, \tag{2.25}$$

where the integration domain is the unit cell resonator volume with dielectric permittivity $\varepsilon(k, \boldsymbol{r'})$.
An intuitive understanding how the mode coupling vanishes can be gained through regarding the underlying symmetries of the incident plane wave and the resonant mode.

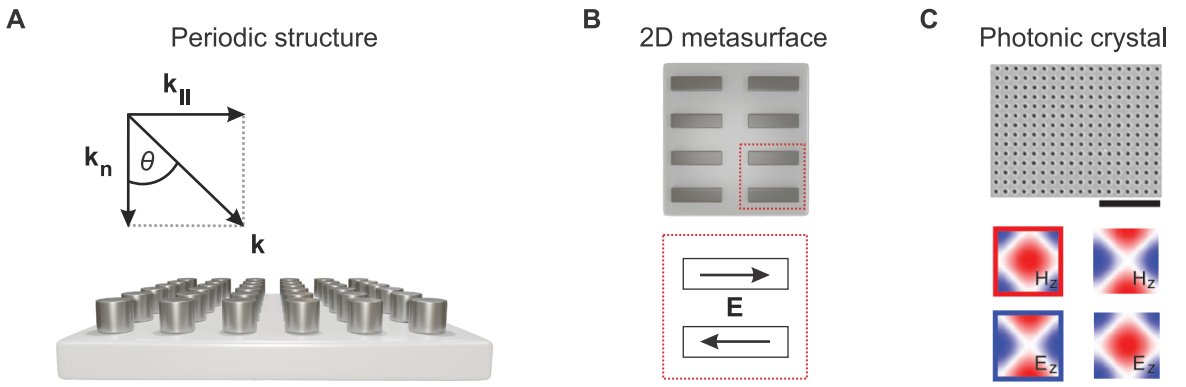

Figure 2.6.: Prominent examples of symmetry-broken BICs. (**A**) Illustration of a periodic structure under illumination with an incident beam with wave vector $\boldsymbol{k}$. Exemplary C_{2z}-symmetric modes in metasurfaces (**B**) or photonic crystals (**C**) cannot couple to plane waves at the Γ-point owing to the symmetry mismatch and are thus perfectly bound in the z direction within the periodic structure. Graphs in (**C**) adapted with permission [17], Copyright 2016, The authors, published by Springer Nature.

As such, plane waves are odd under a π rotation around the normal (here z) axis and thus do not possess C_{2z} symmetry since the polarization of the plane wave is inverted under this symmetry operation. By assuming a constant permittivity throughout the resonator volume ($\varepsilon(k, \boldsymbol{r'}) = \varepsilon(k)$) and splitting the integral into a part in z-direction and a part within the sample plane, the coupling amplitude can be written as

$$D_x(k) = -\frac{k}{2\sqrt{S_0}} [\varepsilon(k) - 1] \int_z e^{ikz'} dz' \int_A E_x(\boldsymbol{r'}) dA. \tag{2.26}$$

Obviously, the coupling coefficient given by eq. 2.26 will vanish for any C_{2z}-symmetric mode since every contribution $E_x(\boldsymbol{r_1})$ will cancel out with its C_{2z}-symmetric analogon $E_x(-\boldsymbol{r_1}) = -E_x(\boldsymbol{r_1})$. Owing to this symmetry mismatch, all modes that are C_{2z} symmetric[2] will not couple to normally incident plane waves at the Γ-point. Therefore, all C_{2z} symmetric modes at the Γ-point are BICs since they do not couple to any radiation and are perfectly localized within the periodic structure in the normal direction.

2.2.3. Symmetry-breaking and coupling to the continuum

The strength of the symmetry-protected BIC concept originates from the controllable coupling of the dark state to the radiation continuum, transforming the BIC into a quasi-BIC (qBIC) with finite Q factors. In principle, a BIC state can be coupled to the continuum by breaking one of the constraints given in eq. 2.24.
One approach is to deviate from the normal incidence illumination as demonstrated in periodic metasurfaces [25] and photonic crystals [56]. In particular, symmetry-protected BICs will start to couple to the continuum once an in-plane momentum of the incident light is provided, meaning $\boldsymbol{k}_{\parallel} \neq 0$ (Fig. 2.7A). For this situation, the

[2]For the sake of simplicity, only C_{2z} modes are considered but it should be noted that also modes of higher symmetry, such as C_{4z} can decouple from the continuum.

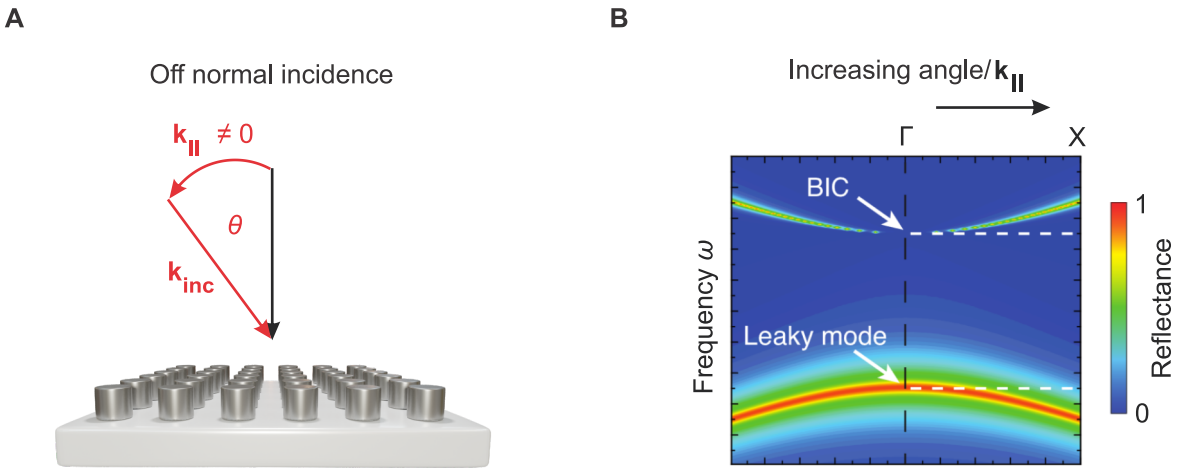

Figure 2.7.: Symmetry-breaking induced by the incidence angle. (**A**) Off normal incidence illumination opens new radiation channels with $\boldsymbol{k}_{\parallel} \neq 0$ for the BIC to couple to and turns the BIC into a leaky resonance as obvious from the dispersion relation in (**B**). Graph adapted with permission [59]. Copyright 2018, American Physical Society.

incident far-field radiation starts to couple to the mode, transforming the BIC into a qBIC. This symmetry-breaking is accompanied with a collapse of the dark state to a Fano resonance, as explained in the last section. One example of the angle-induced coupling to the continuum is depicted in Fig. 2.7B, the dispersion of a one dimensional dielectric chain. Here, the dispersion of a one-dimensional dielectric chain shows a strong dependence of the resonance linewidth and position on the in-plane wave vector $\boldsymbol{k}_{\parallel}$ or incidence angle.

Furthermore, the coupling channel to the far field can be opened through breaking the inherent C_{2z} symmetry by a geometrical perturbation of the unit cell as depicted in Fig. 2.8. In this way, the coupling of the former dark mode to the continuum can be described by the coupling amplitudes D_x (for x-polarized light) and D_y (for $y-$polarized light) between the qBIC and the zero order diffraction channels (reflection/transmission normal to the substrate plane) via [15]

$$\frac{\gamma_{\mathrm{rad}}}{c} = |D_x|^2 + |D_y|^2. \tag{2.27}$$

The Q factor or radiative loss rate γ_{rad} is then directly correlated through eq. 2.26 with the multipolar elements that constitute the mode within the unit cell area S_0 via

$$D_{x,y} = -\frac{k_0}{\sqrt{2S_0}}\left(p_{x,y} \mp \frac{1}{c}m_{y,x} + \frac{ik_0}{6}Q_{xz,yz}\right), \tag{2.28}$$

where higher order elements are neglected. Due to the symmetry of the mode normal to the substrate, the magnetic dipolar $m_{x,y}$ and electric quadrupolar contribution $Q_{xz,yz}$ vanish, along with $D_y = 0$, yielding

$$\frac{\gamma_{\mathrm{rad}}}{c} = \frac{{k_0}^2}{2S_0}|p_x|^2. \tag{2.29}$$

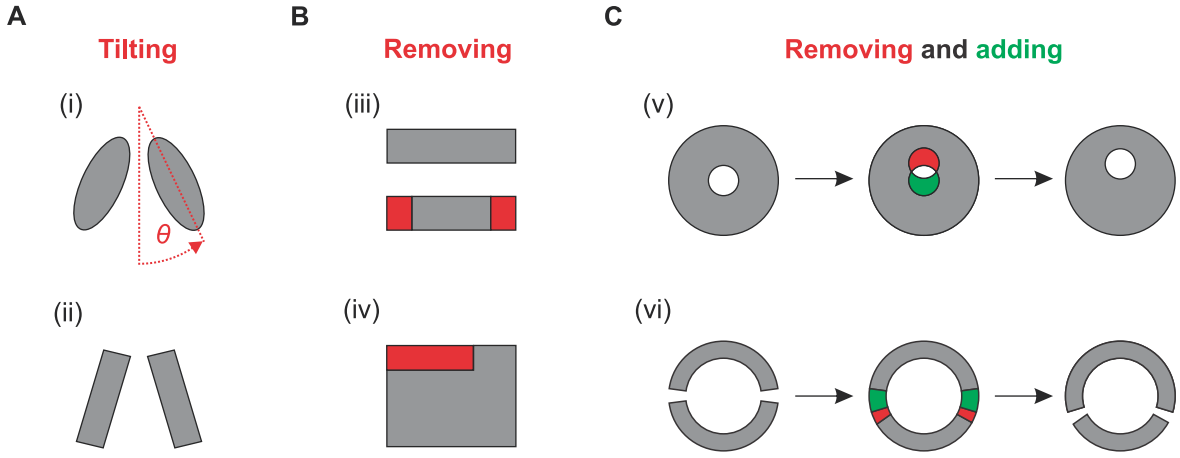

Figure 2.8.: C_{2z} symmetry breaking mechanisms. C_{2z} symmetry breaking relying on the tilting of resonators (**A**), removing resonator area or volume (**B**), and removing and adding parts (**C**) within the unit cell.

Considering only the presence of radiative losses, $Q_{\mathrm{tot}} = Q_{\mathrm{rad}} = \omega_0/\gamma_{\mathrm{res}}$, the radiative Q factor can be obtained as

$$Q_{\mathrm{rad}} \propto \frac{S_0}{2k_0}\,\alpha^{-2}, \tag{2.30}$$

where α is a small geometric perturbation and proportional to the effective dipolar moment $p_{x,y}$ within the unit cell. The asymmetry is calculated relatively, *e.g.*, as removed volume ΔV, cross section area ΔS, or length ΔL of the resonator within the unit cell with respect to the unpertubed dimension of the resonator

$$\alpha = \frac{\Delta V}{V} = \frac{\Delta S}{S} = \frac{\Delta L}{L}. \tag{2.31}$$

Most importantly, the dependence described by equation 2.30 is a hallmark feature of symmetry-broken BIC resonances and confirms the intuitive picture of the inherent correlation between the effective dipolar moment of the qBIC resonance and the geometrical asymmetry α. In particular, the direct connection between the Q factor of the BIC resonance and the geometrical asymmetry eases the experimental access to manipulate the radiative decay rates, rendering the symmetry-broken BIC concept powerful for tunable light-matter interaction.

An exemplary asymmetry sweep is depicted for an ellipse unit cell in Fig. 2.9A, where the asymmetry is introduced by the tilt angle θ. This tilt angle is continuously increased from the BIC condition ($\theta = 0°$). Apparently, the BIC is decoupled from the continuum for preserved in-plane or C_{2z} symmetry for zero tilt angle and starts to couple to the continuum via increasing the tilt angle which manifests itself in an increased linewidth as indicated by the uncertainty bars of the eigenmode in Fig. 2.9A. As expected, the radiative losses and thus the width of the mode increases quadratically with the increased asymmetry, *i.e.*, the tilt angle here.
As a matter of fact, the quadratically inverse scaling law can be generalized to all

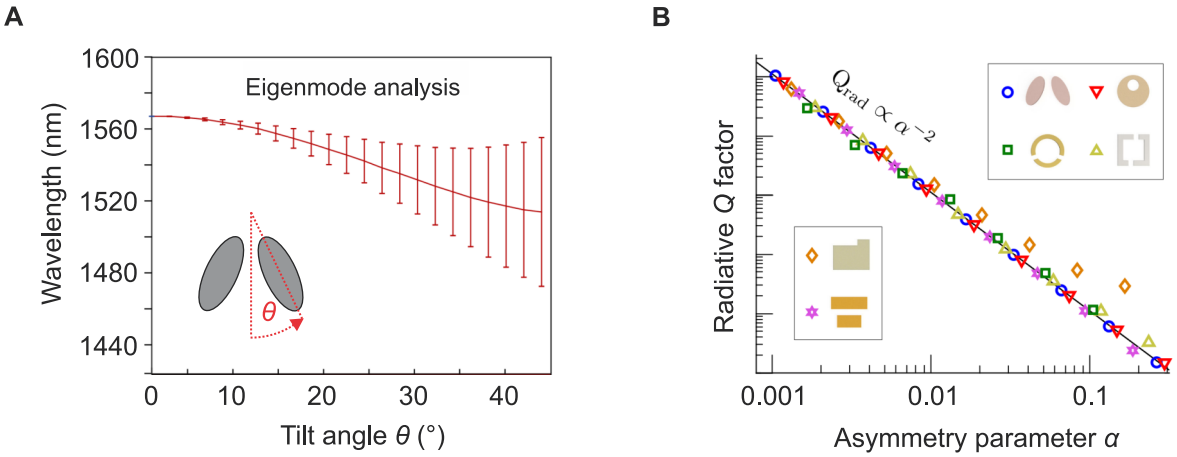

Figure 2.9.: Geometrical symmetry breaking in BIC metasurfaces. (**A**) The eigenmode analysis for two ellipses with increased tilt angle θ illustrates the dispersion and quadratically increasing linewidth for increased tilt angles. (**B**) The general trend for the radiative Q factor for all depicted unit cells follows the predicted α^{-2} behaviour. Graphs adapted with permission [15]. Copyright 2018, American Physical Society.

geometrically symmetry-broken qBICs as depicted in Fig. 2.9B, where all the six depicted geometries follow the α^{-2} behaviour in the double logarithmic plot.

In general, qBIC metasurfaces can be implemented by utilizing a one-element or two-element unit cell as depicted in Fig. 2.8. In essence, the mode structures are controlled by the multipolar moments via the resonator shape and geometry as already introduced in section 2.1.3 or via the relative alignment of elements or geometric perturbations. The simplest option to break the C_{2z} symmetry is to tilt two initially parallel aligned elliptical or rectangular rods by a certain angle θ as illustrated in Fig. 2.8 panel A. Further C_{2z} symmetry breaking can be achieved by locally removing parts of the unit cell as obious from Fig. 2.8 panel B. Finally, another approach is to remove resonator volume at one place and add it add another place, exemplarily depicted for two different symmetry-broken unit cells in Fig. 2.8 panel C.
Apart from the C_{2z} symmetry breaking mechanisms demonstrated above, a variety of options to break the C_{2z} symmetry exist. These involve the shift of single elements in more complex unit cells [47] or the introduction of a symmetry-breaking coupler [60].

2.2.4. Connection between BIC and Fano resonance

A common feature of all qBIC resonances is the coupling of the formerly dark state to the radiation continuum. Initiated by this coupling of the narrow-band BIC with the broad radiation continuum, the qBIC manifests itself with a Fano lineshape. Originally, Fano resonances arised in the context of atomic physics where Ugo Fano described the asymmetric lineshapes in the auto-ionization process of helium atoms [61]. Analogously, the concept can be applied to any wave phenomenon to describe the interference or coupling of a broad and a narrow band photonic mode, in this case the radiation

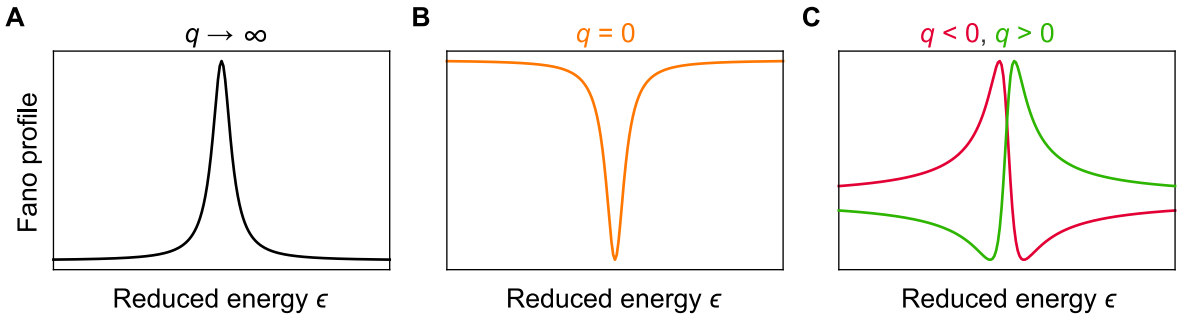

Figure 2.10.: Collapse to a Fano resonance. Different regimes of the interference between the qBIC state and the radiation continuum for the uncoupled discrete state in (**A**) and the continuum in (**B**) along with different interference scenarios for different asymmetry parameters q in case of an interference.

continuum and the qBIC mode [62]. In general, the Fano profile is often written as

$$\sigma(\varepsilon) = \frac{(q+\epsilon)^2}{(1+\epsilon)^2}, \tag{2.32}$$

with the resonance asymmetry parameter q, and the reduced energy $\epsilon = \frac{E-E_0}{\Gamma/2}$ composed of the resonance energy E_0 of the Fano resonance and the corresponding linewidth Γ. This approach captures different regimes of the interaction between the continuum and the discrete state as illustrated in Fig. 2.10.
If the qBIC does not couple to the continuum and only the discrete state is driven, the asymmetric Fano lineshape will transform into a symmetric Lorentz shape while the asymmetry parameter q will diverge ($q \to \infty$) as shown in Fig. 2.10A.
Similarly, if the incident light does not couple to the qBIC due to a large energetic separation between the qBIC and the radiation continuum, the lineshape of the resonance is a quasi-Lorentz with zero asymmetry parameter ($q = 0$) as obvious from Fig. 2.10B.
For all coupled cases with similar resonance energies, the Fano resonance will be asymmetric depending on the magnitude and the sign of the asymmetry parameter q, as shown in Fig. 2.10C.

3. Methodology

This chapter describes the general methodology utilized in this thesis. The first part of this chapter focuses on the numerical simulation method followed by the explanation of the fabrication process, including the extraction of 2D materials and the transfer on top of the metasurfaces. After that, the third part describes the three optical characterization techniques, which were employed in this thesis, and the last part gives a short introduction to the data analysis and fitting routines for the evaluation of the data.

3.1. General process flow

The major work packages are summarized in Fig. 3.1. In general, each project presented in this thesis was carried out according to that process flow, where each step is optimized before moving on to the next.

Usually, a research idea is proposed in scientific meetings or discussions and within that step, the simplest nanophotonic system is determined for its realization. Once the system is set, numerical simulations are performed to characterize the optical response of the target system. The obtained results are used to optimize the design or, eventually, propose a new design with better optical performance.

After the optimization of the numerical simulations, the design is implemented through the nanostructuring of metallic or dielectric compounds. The sample preparation is based on top down fabrication method in a clean room environment. Commonly, the nanostructuring requires fine tuning of the fabrication parameters for each geometry. Moreover, for every material, the etching recipes need to be established and chemical intolerances of the resonator material towards all involved chemicals need to be excluded. In order to target specific resonance positions and for a deeper understanding of the photonic modes, a sweep of the geometrical resonator sizes is performed.

The fabricated structures are then characterized by optical transmission spectroscopy in the visible spectral range or by exciting the SHG through an intense pulsed laser. Depending on the design of the structures, a commercial white light confocal microscopy setup is available for linear excitation polarization along with a custom-built transmission microscope equipped with circularly polarized excitation light for the characterization of chiral structures.

The obtained data are then analyzed with a dedicated fitting routine based on a coupled mode theory model to fit the lineshape of the resonance and to extract the Q fac-

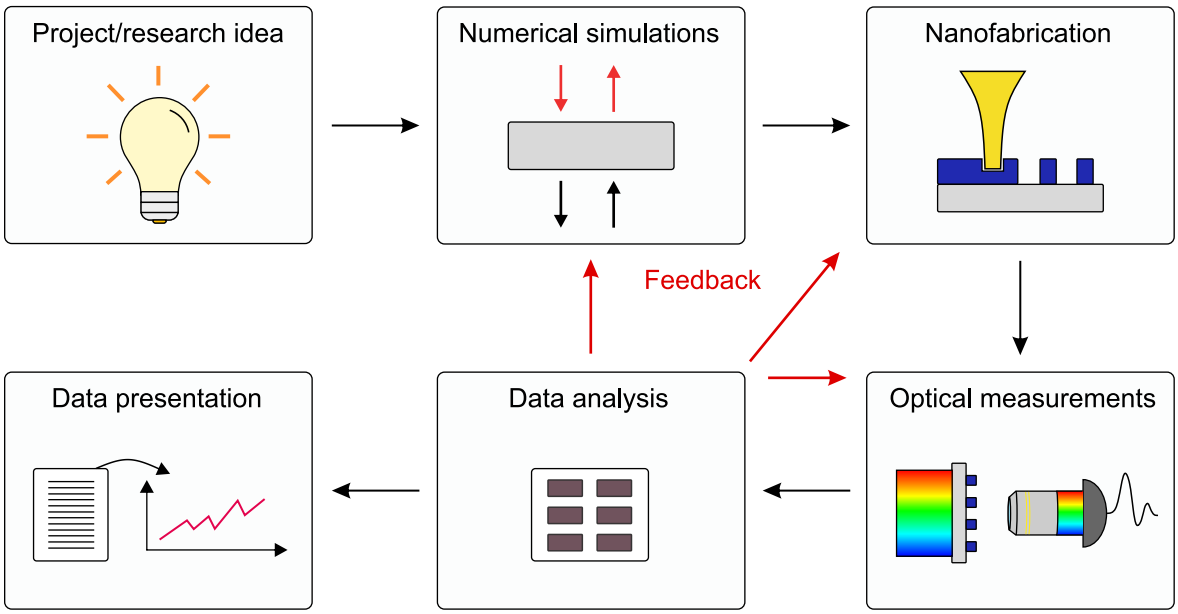

Figure 3.1.: General methodology for research projects in this thesis. All project steps involved for the realization of a research project from the idea to the final data presentation.

tor. Based on the results obtained from the optical measurements and the subsequent data analysis, a feedback for the numerical simulations, the nanofabrication parameter range, or the optical measurements is given to provide a deeper characterization of the nanophotonic design.

Once the simulations and fabrication are optimized and the optical spectroscopy provides satisfying results, the acquired data are analyzed and prepared for the presentation in a scientific journal.

3.2. Numerical simulations

One approach to describe the spectral response of nanophotonic systems is to solve the wave equation under the constraints of the respective boundary conditions imposed by the resonator geometry. Although the equation is analytically solvable, the solution is already complex for a single sphere as introduced in chapter 2. It is thus instrumental and unavoidable to employ numerical methods for solving more complex problems. By considering time-harmonic fields, the wave equation for the electric field is solved more efficiently in the frequency domain and is given as [45]

$$\nabla \times \mu^{-1} \nabla \times \boldsymbol{E} - \omega^2 \varepsilon \cdot \boldsymbol{E} = i\omega \boldsymbol{J}, \tag{3.1}$$

including the current density $\boldsymbol{J}$, which acts as a source for the electric field. For simplicity, the frequency and spatial dependencies were dropped but still hold.

One prominent numerical ansatz to solve this equation is the finite element method (FEM) which divides the nanophotonic structures up in smaller volume elements, so-called *finite elements*. In a nutshell, the nanophotonic structural domain $\boldsymbol{\Omega}$ is defined with appropriate boundary conditions and divided into sub domains $\boldsymbol{\Omega_i}$. For this method, the electric field $\boldsymbol{E}_h$ within the subspace is expanded into basis functions φ_i and given by

$$\boldsymbol{E}_h = \sum_{i=1}^{N} \boldsymbol{e_i}\ \varphi_i, \tag{3.2}$$

where N is the dimension of the subspace and $\boldsymbol{e_i}$ are expansion coefficients.

In principle, two approaches are considered, such as the variational ansatz [63], but the focus here is on the weak formulation of the problem [64]. For this approach, the equations only need to be satisfied for the defined basis functions instead of any arbitrary function, that obeys Maxwell's equations. The common ansatz is to multiply the wave equation 3.1 with a vectorial test function $\boldsymbol{\phi}$ and integrate the product. After a partial integration, the integral is given by [64]

$$\int_{\mathbb{R}^3} \nabla \times \boldsymbol{\phi}\mu^{-1}\nabla \times \boldsymbol{E} - \omega^2 \boldsymbol{\phi}\varepsilon\boldsymbol{E} = i\omega \int_{\mathbb{R}^3} \boldsymbol{\phi}\boldsymbol{J}. \tag{3.3}$$

For simplicity, a compact notation is introduced

$$a(\boldsymbol{\phi}, \boldsymbol{E}) = \int_{\mathbb{R}^3} \nabla \times \boldsymbol{\phi}\mu^{-1}\nabla \times \boldsymbol{E} - \omega^2 \boldsymbol{\phi}\varepsilon\boldsymbol{E}, \tag{3.4a}$$

$$f(\boldsymbol{\phi}) = i\omega \int_{\mathbb{R}^3} \boldsymbol{\phi}\boldsymbol{J}. \tag{3.4b}$$

The simplified form is written as

$$a(\boldsymbol{\phi}, \boldsymbol{E}) = f(\boldsymbol{\phi}). \tag{3.5}$$

After decomposing the domain into the sub domains, the goal is to obtain solutions of the electric field $\boldsymbol{E}_h$ on these sub domains such that

$$a(\boldsymbol{\phi}_h, \boldsymbol{E}_h) = f(\boldsymbol{\phi}_h). \tag{3.6}$$

Inserting the expansion in eq. 3.2 into eq. 3.6 yields

$$\sum_{i=1}^{N} a(\boldsymbol{\varphi}_i, \boldsymbol{\varphi}_j) e_i = f(\boldsymbol{\varphi}_j). \tag{3.7}$$

The form of eq. 3.7 is a matrix equation of the form

$$\underline{\underline{\boldsymbol{A}}}\boldsymbol{e} = \boldsymbol{f}. \tag{3.8}$$

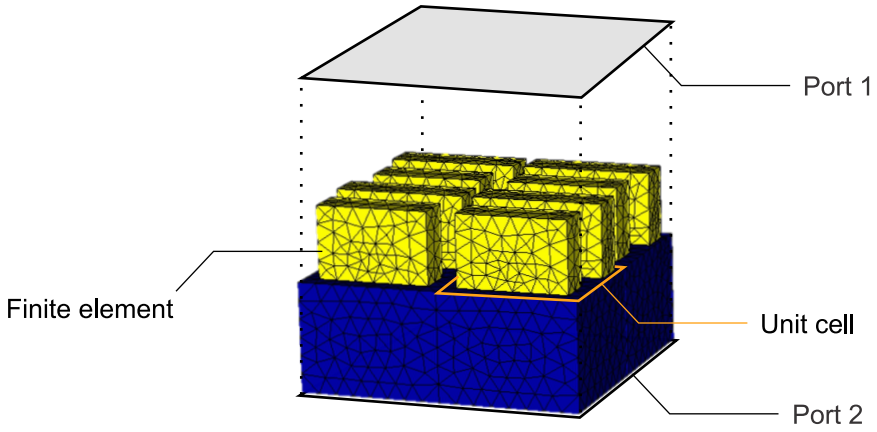

Figure 3.2.: Schematic setup for numerical simulations in this thesis. The complete simulation region is sub-divided into small tetrahedrons. Ports above and below the metasurfaces are used to insert electromagnetic waves and to retrieve the metasurface response normal to the surface. In the plane, periodic boundary conditions are assumed with infinite number of unit cells.

This linear set of equations can be solved by a computer to obtain the expansion coefficients e_i. Using these coefficients, the corresponding electric fields can be reconstructed within the weak formulation.

In practice, the FEM solves the electromagnetic problems often more efficiently since it operates in the frequency domain and the meshing, *i.e.*, the division of the structures in the sub-domains, is adaptive. In fact, the size of the finite elements can be adapted to relevant regions, such as sharp corners and interfaces and does not rely on rectangular grids in contrast to FDTD[1] or RCWA[2] approaches. Since these implementations rely on rectangular grids, they often suffer from poor spatial resolution or, equivalently, from longer simulation times for the same spatial resolution. Additionally, simulations in the time domain come at the cost of long decay times of the fields and thus simulations times, especially for the simulation of high-Q resonances.

In order to model the reflectance and transmittance of qBIC metasurfaces with the FEM method, infinite periodic boundary conditions are assumed in the sample plane. Port boundary conditions (introduced in detail in section 3.5.1) are used to inject TE- and TM- polarized planes waves and to record the transmittance and reflectance response. The corresponding simulation setup is depicted in Fig. 3.2. The material properties of silicon are included by using in-house measured white light ellipsometry data (see Fig. 3.3), while an experimental model based on Sellmaier's equations is used for hBN apart from assuming dielectrics in general as loss- and dispersionless. The lateral dimensions are adjusted to the determined sizes of the scanning electron micrographs and the height profile is checked and adjusted via atomic force microscopy (AFM) images. These experimental data serve as feedback for adjusting the numerical simulations to the exact experimental conditions.

[1] Finite difference time domain
[2] Rigorous coupled-wave analysis

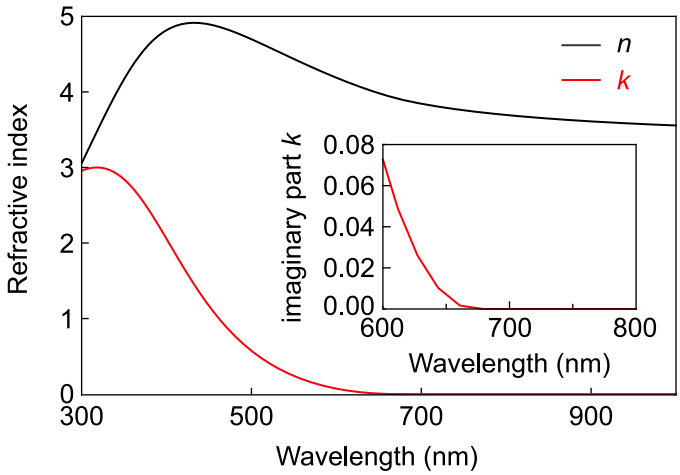

Figure 3.3.: Silicon ellipsometry data. Real and imaginary part of the refractive index, obtained from ellipsometry measurements for an amorphous silicon film. The inset shows the lossless region of the amorphous silicon, starting from 700 nm.

3.3. Nanostructure fabrication

Within this section, the process flow for the fabrication of all-dielectric metasurfaces is explained. The palette of nanostructured materials includes the traditional semiconductor silicon but also 2D materials like hexagonal boron nitride (hBN) or transition metal dichalcogenides (TMDCs). Although the fabrication process is composed of a variety of different steps, it can be reduced to four main steps as highlighted in Fig. 3.4, where each fabrication step needs to be optimized for every material. First, the cleaning and preparation of the substrate is performed, followed by the deposition of the resonator material. Third, electron beam lithography is employed to define the pattern of the nanophotonic structures within an electron beam resist. The subsequent metal evaporation and liftoff step transfer this pattern into a metal hard mask. Finally, the last step includes the reactive ion etching of the resonator material and the chemical wet etching of the metal hard mask to obtain the pure all-dielectric structures.

3.3.1. Substrate cleaning and preparation

Prior to the fabrication process, the silicon dioxide (SiO_2) substrate is cleaned in a beaker of acetone which is placed inside an ultrasonic bath at 55 °C for five minutes to remove dirt particles and is rinsed in isopropanol (IPA) afterwards to prevent drying residues from the acetone. Subsequent oxygen plasma cleaning for 5 minutes removes any organic contamination on the sample and promotes the adhesion to the substrate surface. Hence, oxygen plasma treatment of the surface is employed before the mechanical exfoliation of 2D materials which leads to a better yield and larger flakes. Additionally, oxygen plasma etching increases the surface energy and promotes the wetting of the substrate surface, resulting in increased film quality and flatness.

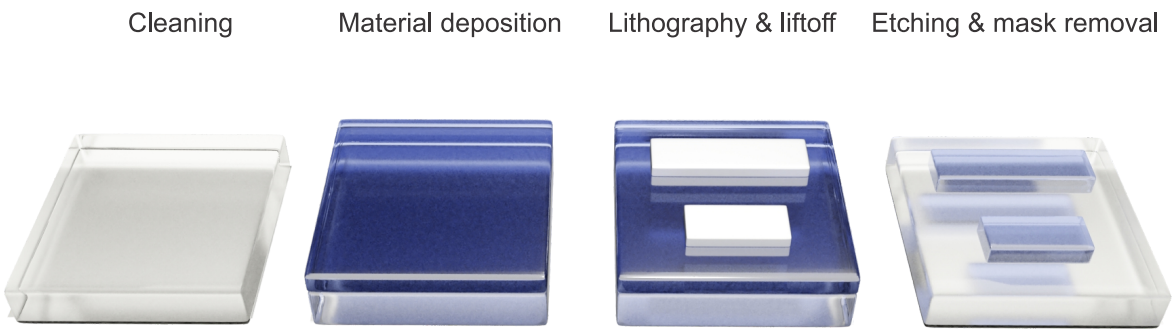

Figure 3.4.: Fabrication overview. Schematic illustration of the important fabrication steps for all-dielectric nanostructures used in this thesis.

3.3.2. Material deposition

Within this thesis, different types of materials are deposited, such as all-dielectric materials as resonator components but also metals which serve as etching hard masks. In particular, two fundamentally different deposition techniques are employed, one relying on vapour deposition methods for the fabrication of amorphous silicon films and etching hard masks and the other technique is based on mechanical exfoliation to extract monocrystalline bulk flakes of 2D materials.

Deposition of traditional materials

Electron beam evaporation (UHV E-beam, Bestec) is utilized for the deposition of etching hard masks, such as gold, titanium, chromium, and silicon dioxide as schematically introduced in Fig. 3.5A. The substrate is placed into a ultra-high vacuum (UHV) process chamber with the topside upside down. By passing a current through a filament, an electron beam with high kinetic energy (up to 8 keV) is generated via an accelerator which is deflected and guided onto the target material via a magnetic field. The electrons impinging on the target locally heat the source which leads to a melting or even a sublimation of the material in the UHV. Afterwards, the extracted atoms will rise up and attach to the substrate. Most importantly, due to the localized heating, this technique generates an almost collimated point-like beam of ejected source atoms which is highly anisotropic. In fact, this anisotropy is beneficial for a smoother liftoff process later. One critical parameter is the control of the deposition rate, which should be kept below 1.0 Å/s, to guarantee good optical film qualities, especially when using SiO_2 and chromium as hard mask materials.

Apart from the deposition of metals, plasma enhanced chemical vapor deposition (PECVD, PlasmaPro 100, Oxford Instruments) is used for the deposition of amorphous silicon as illustrated in Fig. 3.5B. In this case, the sample is transferred into a UHV chamber which is flooded with the reactant gas silane (SiH_4) under a constant flow of 500 sccm to obtain a chamber pressure of 1000 mTorr where the gas ignites into

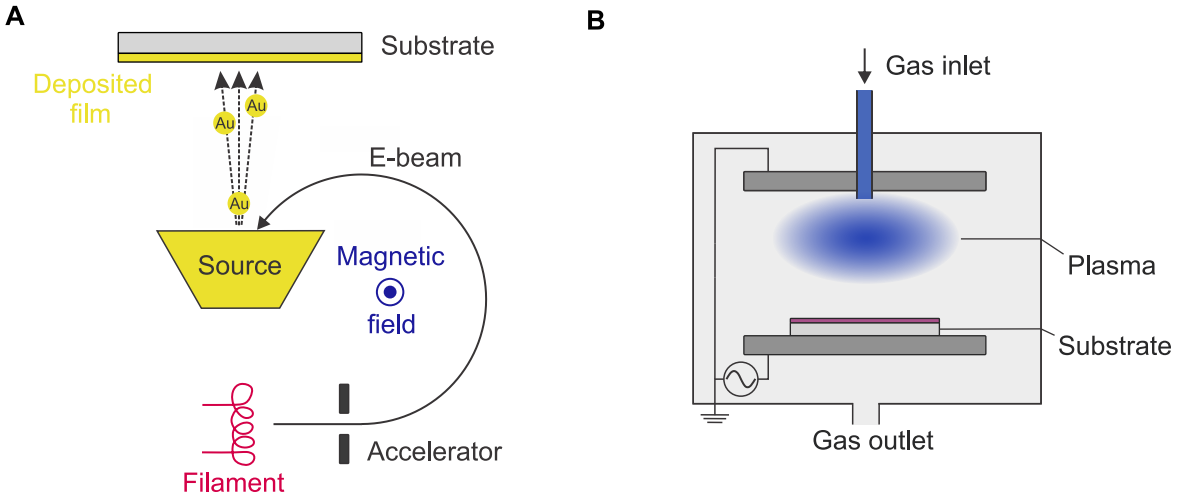

Figure 3.5.: Material deposition techniques in this thesis. (**A**) Schematic illustration of electron beam evaporation showing the extraction of electrons from the filament. The electrons are accelerated and deflected onto the source by a magnetic field. The local heating initiated by the incident electrons leads to an evaporation or sublimation of the material that deposits on the substrate. (**B**) Principle of PECVD where a reaction gas is ignited between two electrodes leading to a reaction on the substrate where a solid layer of silicon forms on top of it.

a plasma between the substrate and the RF electrode (indicated with the RF sign in Fig. 3.5B) using 10W RF power. Initiated by the plasma, a chemical reaction takes place on the surface of the substrate where one of the products is silicon. The reaction product condenses at the surface of the silicon dioxide substrate to form an amorphous silicon layer. Advantageously, the ignition of the plasma reduces the growth temperature of the silicon on the substrate to 250 °C.

Mechanical exfoliation

In contrast to the physical vapor deposition techniques introduced above, mechanical exfoliation provides monocrystalline material quality since the exfoliation crystals are provided as high-quality monocrystalline samples. In the case of hBN, the samples were grown from collaborators in Japan, utilizing high pressure (4.5 GPa) and high temperature (1500 °C) to obtain single crystal hBN flakes from a barium boron nitride solution [67]. By utilizing mechanical exfoliation, single sheets of hBN up to bulk layer thicknesses can be extracted from a target crystal onto a prepared (oxygen-plasma etched) substrate. The corresponding process flow for the mechanical exfoliation of hBN is depicted in Fig. 3.6.

In the beginning, a piece of scotch tape (blue tape, Nitto) is pressed onto the hBN exfoliation crystal as indicated in Fig. 3.6A and peeled off (see Fig. 3.6B). This process is repeated a few times until an optimum between the flake thicknesses, high yield, and the lateral sizes of exfoliated flakes is reached. Commonly, this takes 4-8 exfoliation steps which leads to an extraction of bulk hBN flakes. Subsequently, the

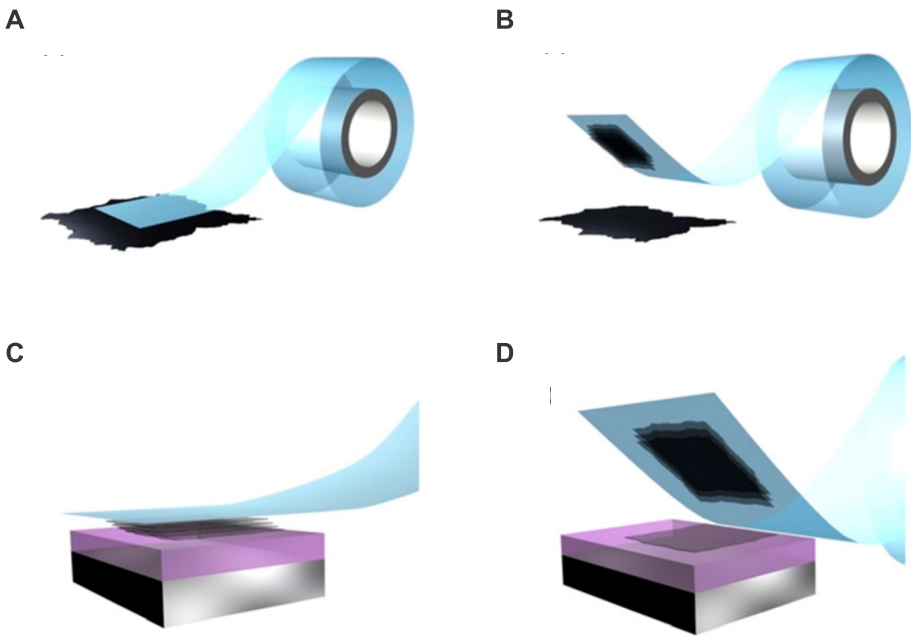

Figure 3.6.: Schematic illustration of the mechanical exfoliation process for 2D materials. (**A**) The process starts by pressing a sticky tape onto the target 2D material crystal and peeling it off as illustrated in (**B**). (**C**) The tape with the bulk 2D material is pressed onto the target substrate and pealed off again which leaves the 2D material back on the target substrate from monolayer to bulk thicknesses (**D**). Graph adapted with permission [68]. Copyright 2012, IOP Publishing.

tape is pressed onto the target SiO_2 substrate at a temperature of 100 °C to reduce water residues and air encapsulation between the flake and the substrate (see Fig. 3.6C). This helps to improve the adhesion and thus provides larger flakes and a higher yield. Finally, the tape is peeled off and a few hBN layers up to bulk hBN will remain on the substrate as shown in Fig. 3.6D. The exfoliation process is usually carried out on previously prepared substrates with a marker system to unambiguously target the flakes during the lithography process.

3.3.3. Lithography and liftoff

Before the lithography process starts, the preparation of the sample with previously deposited hBN or silicon is done via the spin-coating of an electron beam resist, in detail, the positive tone poly(methyl methacrylate) (PMMA). In fact, photo resists based on PMMA are among the highest resolution resists and provide easy and straightforward operation. Here, a 100 nm thin PMMA layer of low resolution type (495PMMA A4, Kayakuam) is spun onto the substrate for one minute at 5000 revolutions per minute (rpm) with a subsequent soft-bake for one minute at 170 °C. Following the first layer, a 80 nm thin high-resolution layer (950k A2, All-resist) is spun on top of it at 3000 rpm for one minute with another soft-bake at 170 °C for one minute. Crucially, this double layer aids the liftoff process later on since this heterostructure resist guarantees

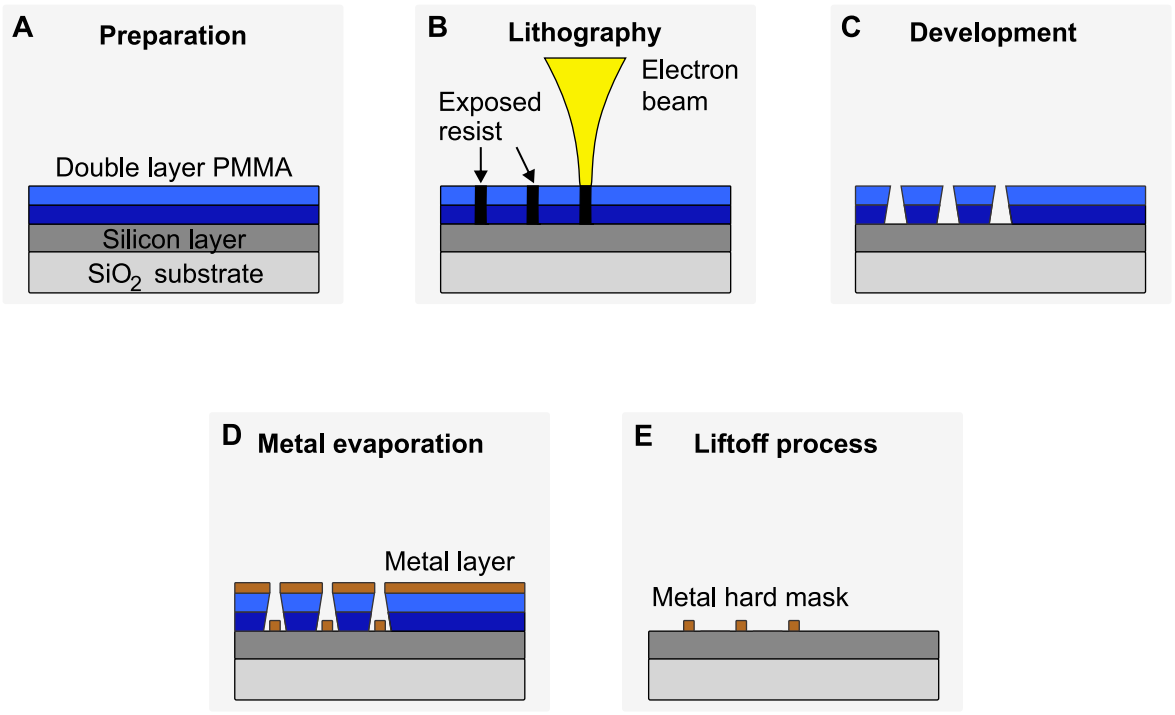

Figure 3.7.: Fabrication I. Schematic illustration of every fabrication step for all-dielectric nanostructures used in this thesis.

an undercut profile after the development step as indicated in Fig. 3.7C.
The whole preparation process is depicted in Fig. 3.7A and is finished by the deposition of an electrically conductive polymer (Espacer 300Z) to prevent electronic charge accumulations and thus pattern distortions during the lithography process (not shown in the figure).

Once the sample is prepared, it is coupled into a UHV electron beam lithography (eLine plus, Raith) machine to expose the resist with an electron beam with a feature size resolution down to 20 nm. In the fabrication processes used in this thesis, the samples are exposed with an acceleration voltage $U_{\mathrm{acc}} = 30$ kV at a working distance of 10 mm using aperture sizes between 10 and 20 μm. Usually, the area doses were between 300 and 450 $\mu\mathrm{C/cm}^2$ depending on the geometries and the array densities.

Upon irradiation with the electron beam, the electrons will scatter within the resist and dissociate the PMMA bonds at the respective exposure position which significantly reduces their solubility in the developer solution. Thus, this transforms the electron exposure into a pattern in the resist as indicated in Fig. 3.7B and Fig. 3.7C.

For the fabrication of hBN or height-driven metasurfaces, the lithography process is slightly more complex since a good overlap between the desired writing pattern and either the flake or the already existing pattern is crucial. For this purpose, a predefined marker system is utilized where the lithography pattern can be matched with the real sample with accuracies down to 5 nm.

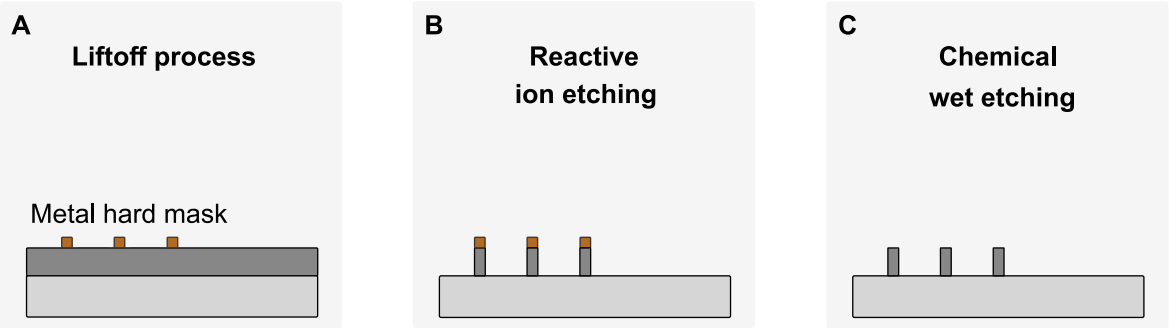

Figure 3.8.: Fabrication II. Schematic illustration of the last fabrication steps of all-dielectric metasurfaces.

After the electron beam irradiation, the conductive polymer is removed by a 10 s rinse in water, followed by a 90 s development in a 3:1 IPA:MIBK (Methyl isobutyl ketone) before it is laid in a beaker with IPA for 20 s and finally dried under a nitrogen flux. After the development step, the exposed resist is removed leaving a hole mask for the electron beam evaporation as depicted in Fig. 3.7C.

The developed samples are coupled into the electron beam evaporator (as described in the previous section) where a thin layer of titanium and gold for hBN metasurfaces or silicon dioxide and chromium for silicon metasurfaces is deposited as illustrated in Fig. 3.7D. Usually, a silicon dioxide buffer layer is used to prevent chromium from diffusing into the resonator material and introducing optical losses.

Finally, the sample is left for the lift-off process overnight in a special PMMA remover (remover 1165, Microposit). The hard mask is stripped off on top of the resist while it stays at the cavities in the resist where it is in direct contact with the resonator material as depicted in Fig. 3.7E, leaving back the hard mask for the etching process.

3.3.4. Reactive ion etching and hard mask removal

Reactive ion etching (RIE, PlasmaPro 100 ICP-RIE, Oxford Instruments) is employed to transfer the previously defined hard mask pattern into the resonator material as indicated in Fig. 3.8A and Fig. 3.8B. Similar to the PECVD process, the etching gases, here chlorine with a laminar flow of 20 sccm and argon with a laminar flow of 7 sccm, are flooded into the chamber at a pressure of 2 mTorr. Subsequently, a plasma within the etching gases between the sample and RF electrode is ignited using 20 W HF and 200 W ICP power. The plasma is then accelerated towards the sample. On the surface, the plasma chemically reacts with the etched material and forms a volatile compound which is sucked away by the vacuum pumps. Most importantly, this process only takes place at positions that are not covered by the hard mask, only leaving back the dielectric material below the masked regions. The last step is the removal of the hard mask either via chemical wet etching for metals or through another RIE step for silicon dioxide as indicated in Fig. 3.8C to obtain the pure all-dielectric structures.

3.3.5. 2D material transfer

Apart from the fabrication of all-dielectric metasurfaces, monolayers of TMDCs were exfoliated and transferred on top of the metasurfaces, which is described in the following and illustrated in Fig. 3.9.

As initial step, commercially available PDMS (poly dimethyl siloxane, PDMS 8, Gel-Pak) is placed on a glass slide. Subsequently, a TMDC layer is extracted from a bulk crystal with blue tape (Nitto) and exfoliated several times. Afterwards, the tape is pressed onto the PDMS after 3-4 exfoliation steps, as known from the bulk hBN exfoliation. The tape is peeled off gently, leaving TMDC flakes back on the PDMS stamp.

Subsequently, potential monolayer TMDC flakes are identified with an optical microscope and need to be differentiated from multilayer TMDC flakes. As shown in Fig. 3.10A, the optical contrast of the white light reflection microscopy image is not sufficient to differentiate a monolayer (white dashed line) from a multilayer (green dashed line) flake. A more sophisticated method is the utilization of photoluminescence (PL) microscopy. Owing to the transition from an indirect band-gap for multilayer flakes to a direct band-gap in monolayer TMDCs, the PL is much higher in monolayer TMDCs [69]. Potential monolayer flakes are thus unambiguously identified by PL microscopy to confirm the layer number [70] as depicted in Fig. 3.10B.

Once a suited flake is identified, it can be transferred onto the target metasurface using a custom built transfer setup. The setup is equipped with a translatable rotation stage for the target sample and a motorized stage to control the vertical movement of the PDMS stamp. For the alignment control between the target flake and the metasurface and for process surveillance, an optical microscope is equipped with a high working distance 20x objective. Using this microscope, the PDMS stamp is spatially aligned with a precision of 500 nm and is slowly approached with the target position until the PDMS stamp is almost in contact with the metasurface. From here on, the velocity of

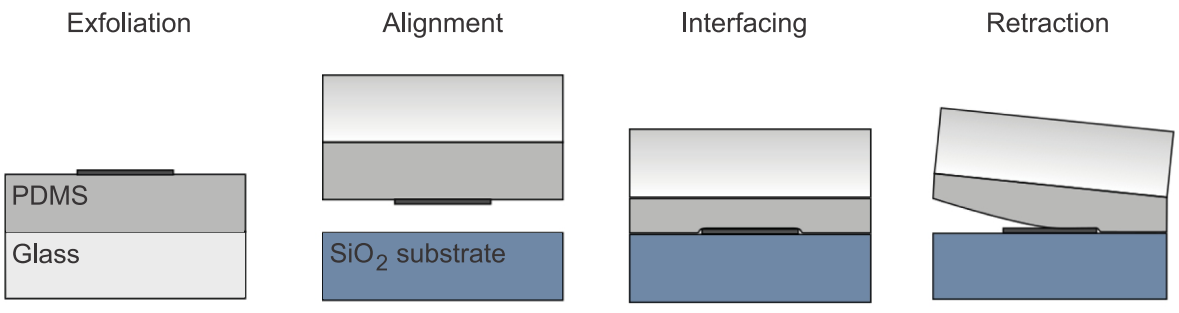

Figure 3.9.: PDMS dry-transfer of atomically thin materials. Few-layers of 2D materials are exfoliated on a PDMS sheet places on a glass slide. The PDMS stamp is aligned with the target substrate and brought in contact via a transfer setup. After a slow retraction of the stamp, the flake is released on the substrate or on top of the metasurface. Graph adapted with permission [71].

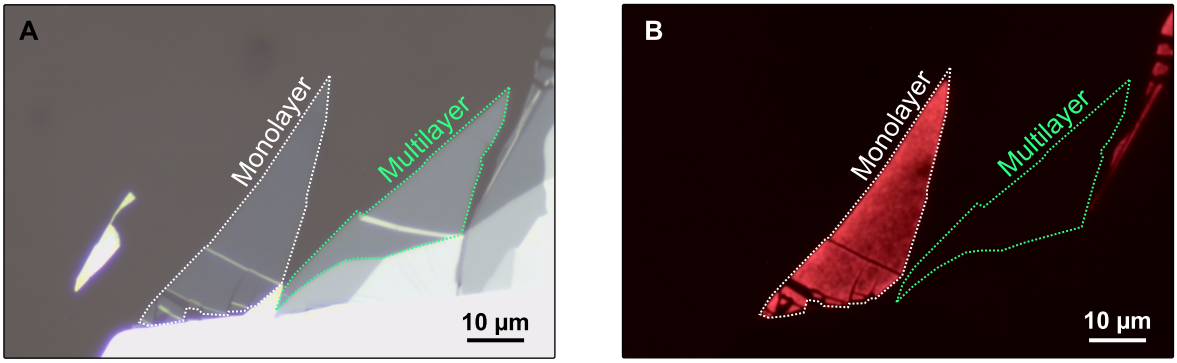

Figure 3.10.: Identification of TMDC monolayers. (**A**) Potential monolayer flakes (outlined by the white dashed line) are identified with an optical microscope and need to be differentiated from multilayers (green dashed line). (**B**) PL microscopy confirms the monolayer thickness of the flake on the left.

the stamp, which is moving towards the sample, is slowed down further to guarantee a slow progression across the metasurface, increasing the transfer success. Once the PDMS stamp has moved completely across the metasurface, it is retrieved in an even smaller pace. When the stamp is not in contact with the flake anymore, it can be moved up quickly and, ideally, the flake is released on top of the metasurface.

3.4. Optical characterization

For the optical characterization of the photonic metasurfaces in this thesis, different setups are utilized including a confocal white light microscopy setup for straightforward characterizations with linear excitation polarization. In addition, a custom-built transmission microscope equipped with chiral excitation light is described along with the optical setup for the characterization of nonlinear measurements.

3.4.1. Confocal white light microscopy

All transmittance spectra with linear excitation polarization are taken with a confocal white light microscopy setup as depicted in Fig. 3.11. The sample is illuminated by collimated white light from a halogen lamp (Thorlabs source, OSL2), that is linearly polarized below the sample. The transmitted beam is collected either with a 10x (NA = 0.25) or 50x (NA = 0.8) objective. Above the objective, the transmitted light is focused and coupled into a multi-mode fiber, which effectively leads to a confocal detection of the signal. The multi-mode fiber guides the light into the spectrometer where it is directed onto a grating from which the light gets dispersed and directed onto a silicon CCD chip. In order to obtain a transmittance spectrum, the transmitted intensity through the metasurface is normalized to the transmitted intensity through the bare SiO_2 substrate (Fig. 3.12). In this way, all unwanted spectral features of the optical beam path, the lamp, and the substrate itself are removed.

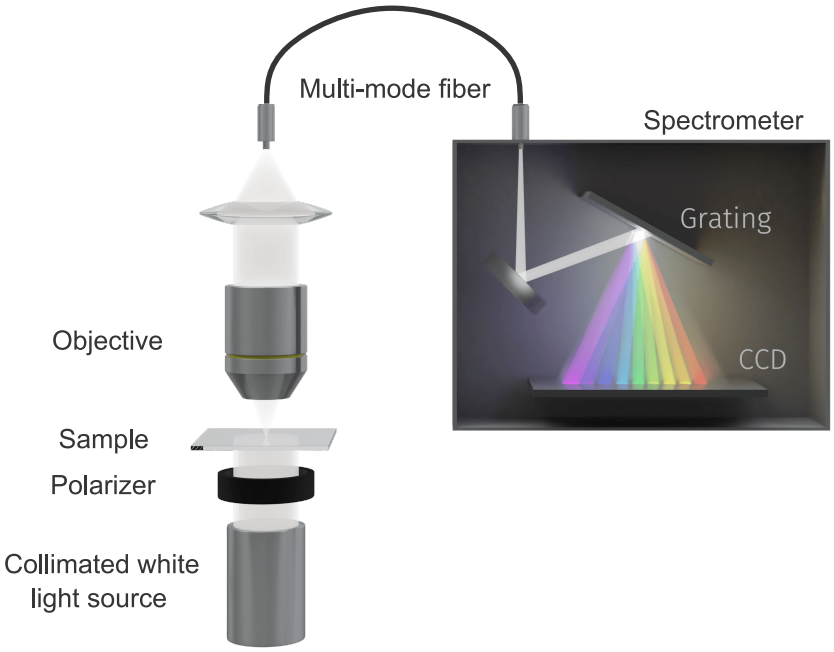

Figure 3.11.: Illustration of the confocal white light setup utilized for the characterization of metasurfaces with linear polarization. Light from a collimated white light source is polarized and guided onto the sample. The transmitted light is collected by an objective and confocally coupled into a multimode fiber, which directs it to a grating-based spectrometer. The light is dispersed by a diffractive grating and directed on a silicon CCD which acquires the spectra. Graph taken with permission [72].

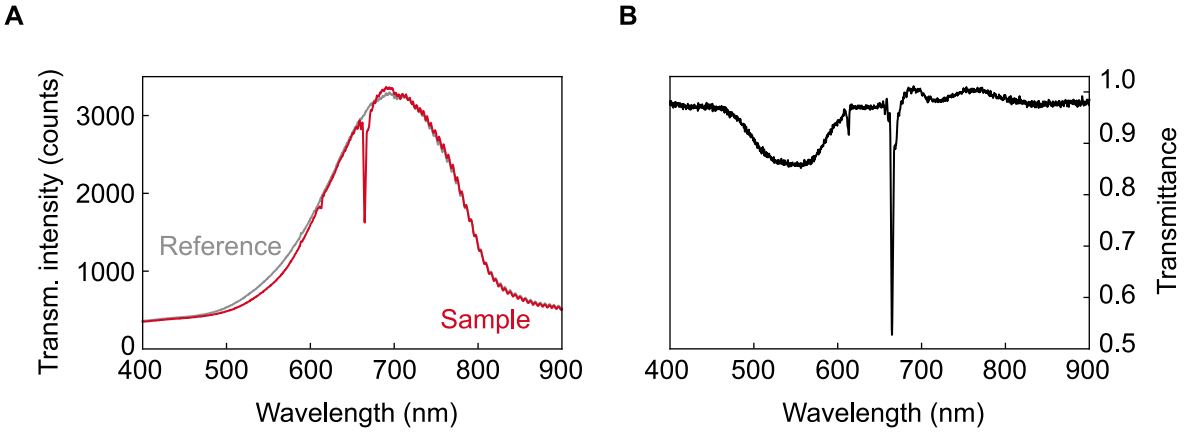

Figure 3.12.: Transmittance data normalization. (**A**) The transmitted intensity through the sample (red curve) is measured and normalized to the reference measurement (gray curve), yielding the transmittance spectrum as depicted in (**B**).

3.4.2. Chiral white light measurements

The optical characterization of chiral metasurfaces was performed with a custom built optical transmission microscope as depicted in Fig. 3.13, which excites the sample from the bottom with LCP or RCP light.

In detail, coherent light from a white light laser (NKT Photonics SuperK) is directed via a mirror onto a partial beam splitter (PBS) which divides the beam up into two arms. In the upper arm, a linear polarizer polarizes the white light horizontally (HP) while in the lower arm the light is polarized vertically (VP) with respect to the optical table plane. Usually, one of the arms is blocked such that only one linear polarization is incident on the quarter-wave plate (QWP). Since small misalignments between the linear polarizer and the QWP can already lead to elliptical polarization, the QWP is aligned with the linear polarizers in order to guarantee circular light polarization. The chiral light is then focused by a 10x (NA = 0.2) excitation objective (Obj) where the numerical aperture is small to prevent large excitation angles. In fact, since BIC resonances are very sensitive to incidence angle, the choice of the excitation is crucial. The transmitted light is then collected by a 60x (NA = 0.7) objective that either directs the light to a CCD camera via a flip-mirror (FM) for the precise positioning of the chiral metasurfaces or guides the light into the grating based high-resolution spectrometer (Princeton instruments). For the measurement of the co- and cross-polarization terms a chiral analyzer, consisting of a QWP and a linear polarizer was installed after the collection objective.

Similar to the characterization with the confocal optical microscopy setup, each measurement is referenced to the bare SiO_2 substrate to obtain the transmittance spectra for both circular polarizations.

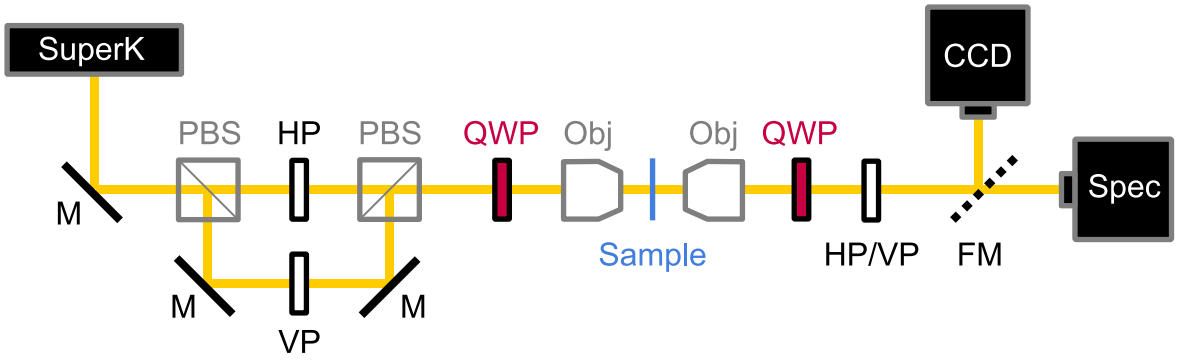

Figure 3.13.: Sketch of the utilized setup for the characterization of the chiral metasurfaces. White light of a white light laser is guided via mirrors (M) and split into two paths by partial beam splitters (PBS), where the light passes through a horizontal (HP) or vertical (VP) polarizer. After that, the light is circularly polarized by a quarter wave plate (QWP) and focused on the sample via a objective (Obj). The transmitted light is collected with another objective and analyzed through a QWP and a linear polarizer. From there, the light can either be guided to the CCD camera or the spectrometer (Spec) via a flip mirror (FM).

3.4.3. Nonlinear measurements

The nonlinear measurements for second harmonic generation (SHG) are performed by exciting the sample with the output of a tunable Ti:sapphire laser (Coherent Chameleon Ultra II) with repetition rate of 80 MHz, where the excitation wavelength can be fine tuned to the resonances of the BIC metasurfaces. Commonly, a transmission geometry is employed where the polarization of the pump light is controlled by a half wave plate ($\lambda/2$ WP). The sample is excited with a low NA 10x objective (NA = 0.25) and the SHG signal is collected with a higher NA 40x objective (NA = 0.6). The SHG signal is then filtered with a short pass optical filter (SPF) at 680 nm and can be analyzed with a linear polarizer (LP) before it is directed to a grating-spectrometer with a silicon CCD camera (Princeton Instruments).

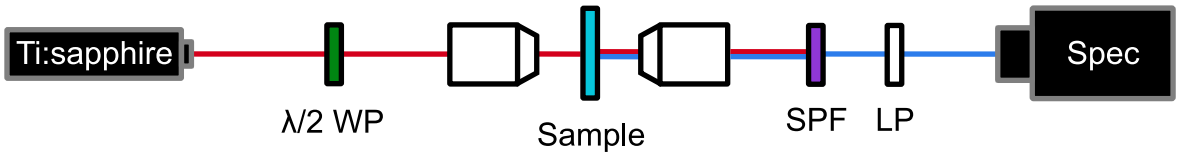

Figure 3.14.: Sketch of the optical setup for nonlinear measurements. A linearly polarized and tunable Ti:sapphire pulsed laser is directed via a half waveplate ($\lambda/2$ WP) and an excitation objective onto the sample where the high intensity and the nonlinear susceptibility $\chi^{(2)}$ give rise to SHG. The SHG is collected with an objective and the pump wavelength is filtered by a short pass filter (SPF). The polarization of the SHG is analyzed by a rotatable linear polarizer (LP) before it is coupled into the spectrometer (Spec).

3.5. Data analysis

This section comprises the explanation of the data analysis for the extraction of the Q factors from the experimental transmittance spectra. In particular, the aim is to derive an intuitive understanding of temporal coupled mode theory (TCMT) and why this model was chosen over a Lorentzian or Fano resonance model. A more detailed derivation can be found in [73] and [74].

3.5.1. Temporal coupled mode theory

Temporal coupled mode theory describes the temporal evolution of the mode amplitude a within a single-mode optical resonator with resonance frequency ω_0 which loses energy at a rate γ via a loss channel

$$\frac{\mathrm{d}}{\mathrm{d}t}a(t) = (i\omega_0 - \gamma)a(t), \tag{3.9}$$

where $|a|^2$ is the energy stored inside the resonator. A schematic illustration which depicts the necessary observables is depicted in Fig. 3.15. If the system is allowed to exchange energy with its environment, the injection $s_{i,+}$ or ejection $s_{i,-}$ of energy via port i can be described for the

$$\text{in-coupling as} \quad \boldsymbol{\kappa}^T \boldsymbol{s}_+ = \begin{pmatrix} \kappa_1 & \kappa_2 \end{pmatrix} \begin{pmatrix} s_{1,+} \\ s_{2,+} \end{pmatrix}, \qquad \text{out-coupling as} \quad \begin{pmatrix} d_1 & d_2 \end{pmatrix} \begin{pmatrix} s_{1,-} \\ s_{2,-} \end{pmatrix}, \tag{3.10}$$

where $\boldsymbol{\kappa}$ and $\mathbf{d}$ are the coupling coefficients for injected and ejected waves, respectively. Furthermore, two ports are assumed, which represent the reflection and transmission planes of the resonator system or the metasurface, as already introduced in the numerical simulation part.

Apart from the resonant interaction of the injected energy via port i, energy can be directly exchanged between the ports without a cavity excitation, described by the scattering matrix C. Crucially, both energy transfer pathways can interfere with each other, which manifests itself as the emergence of a Fano resonance. Beneficially, the TCMT model resembles both the Fano and the Lorentzian shape and is thus chosen over these models. Although the Lorentzian lineshape can also be described with the Fano formalism, the linewidth of the resonance diverges for that condition, leading to unreliable Q factors.

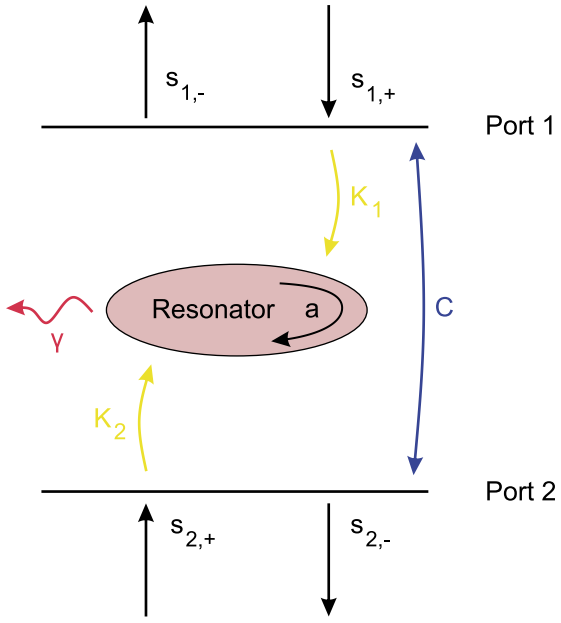

Figure 3.15.: Temporal coupled mode theory for resonant metasurfaces. Schematic illustration of all relevant observables for the description of the reflectance and transmittance of a resonant metasurface. The resonance amplitude a of the resonator is influenced by the resonator losses γ (red curved arrow) and the incoupling of energy κ_i (yellow arrows) via each port i. The direct coupling between the ports is described via the scattering matrix C.

By taking all the relevant terms and interactions into account, the main TCMT equations are obtained as

$$\frac{\mathrm{d}}{\mathrm{d}t}a(t) = (\mathrm{i}\omega_0 - \gamma)a(t) \ + \boldsymbol{\kappa}^T \boldsymbol{s}_+, \tag{3.11}$$

$$\boldsymbol{s}_- = C\boldsymbol{s}_+ + a\boldsymbol{d}. \tag{3.12}$$

In order to obtain far-field quantities, such as the reflectance or transmittance, a time-harmonic dependence of the injected waves $\boldsymbol{s}_+ \propto e^{\mathrm{i}\omega t}$ is assumed, yielding a resonator amplitude

$$a = \frac{\boldsymbol{\kappa}^T \boldsymbol{s}_+}{\mathrm{i}(\omega - \omega_0) + \gamma}. \tag{3.13}$$

By utilizing the time-reversal symmetry which is guaranteed by Lorentz reciprocity of the system, the energy in-coupling and out-coupling of the cavity needs to equal

$$\boldsymbol{\kappa} = \boldsymbol{d}, \tag{3.14}$$

relating the injected and ejected energy via 3.12 as

$$\boldsymbol{s}_- = \left(C + \frac{\boldsymbol{\kappa}\boldsymbol{\kappa}^T}{i(\omega - \omega_0) + \gamma}\right)\boldsymbol{s}_+ \equiv S\boldsymbol{s}_+, \tag{3.15}$$

with the scattering matrix S. Beneficially, the scattering matrix approach allows to relate the output of a system with the input. For the two-port system of interest here, where the energy is only injected from port 1 ($s_{2,+} = 0$), the scattering matrix is given by

$$\begin{pmatrix} s_{1,-} \\ s_{2,-} \end{pmatrix} = \begin{pmatrix} s_{11} & s_{21} \\ s_{12} & s_{22} \end{pmatrix} \begin{pmatrix} s_{1,+} \\ 0 \end{pmatrix} = \begin{pmatrix} s_{11}s_{1,+} \\ s_{12}s_{1,+} \end{pmatrix}. \tag{3.16}$$

Using known relations for the radiated power through a given port yields the reflection r and transmission coefficient t as

$$r = \frac{s_{1,-}}{s_{1,+}} = s_{11}, \tag{3.17}$$

$$t = \frac{s_{2,-}}{s_{1,+}} = s_{12}. \tag{3.18}$$

The above quantities are connected with the reflectance R and transmittance T via

$$R = |r|^2 \qquad \text{and} \qquad T = |t|^2. \tag{3.19}$$

By using the relation $C\boldsymbol{\kappa}* = -\boldsymbol{\kappa}$, and only considering radiative losses $\gamma = \gamma_{\mathrm{rad}}$, the transmittance can be written as [73]

$$T = |s_{21}|^2 = \frac{{t_0}^2(\omega - \omega_0)^2 + {r_0}^2\gamma^2 + 2r_0t_0(\omega - \omega_0)\gamma}{(\omega - \omega_0)^2 + \gamma^2} \tag{3.20}$$

For the quality (Q) factor extraction used in this thesis, the transmittance spectrum is fitted according to 3.20 with r_0, t_0, ω_0, and γ as fitting parameters. Since γ is determined through the TCMT approach, the Q factor of the resonance can be extracted via

$$Q = \frac{\omega_0}{2\gamma}. \tag{3.21}$$

4. Radial bound states in the continuum for polarization-invariant nanophotonics

The results presented in this chapter are published in the scientific open-access journal Nature Communications (L. Kühner et al., *Nat. Com.* **13**, 4992 (2022), *see ref. [75]). As a basis of the chapter, the peer-reviewed manuscript is used and complete sentences or even paragraphs will be taken word by word from the manuscript along with graphic content/figures since Springer Nature allows the reprinting of own contributions in theses (see Nature Portfolio statement in the appendix), also in accordance with the terms of the CC-BY Creative Commons Attribution 4.0 International license* `http://creativecommons.org/licenses/by/4.0/`. *The theoretical explanations and introduction to nonlinear optics follow and are taken from Ref. [76].*

All-dielectric nanophotonics underpinned by the physics of bound states in the continuum [17] (BICs) have demonstrated breakthrough applications in nanoscale light manipulation [16], frequency conversion [23, 30] and optical sensing [28, 77]. Leading BIC implementations range from isolated nanoantennas with localized electromagnetic fields [22] to symmetry-protected metasurfaces with controllable resonance quality (Q) factors [15]. However, they either require structured light illumination with complex beam-shaping optics or large, fabrication-intense arrays of polarization-sensitive unit cells, hindering tailored nanophotonic applications and on-chip integration. Here, radial quasi bound states in the continuum (radial BICs) are introduced as a new class of radially distributed electromagnetic modes controlled by structural asymmetry in a ring of dielectric rod pair resonators. The radial BIC platform provides polarization-invariant and tunable high-Q resonances with strongly enhanced near fields in an ultracompact footprint as low as 2 μm^2. In this chapter, radial BIC realizations in the visible for sensitive biomolecular detection and enhanced second-harmonic generation from monolayers of transition metal dichalcogenides are demonstrated, opening new perspectives for compact, spectrally selective, and polarization-invariant metadevices for multi-functional light-matter coupling, multiplexed sensing, and high-density on-chip photonics.

4.1. Numerical investigation and experimental realization

4.1.1. State of the art and advantages of the radial arrangement

The rise of optical metasurfaces has launched a variety of breakthrough applications ranging from negative refraction [20] and ultrathin optical elements [78] to photonic computation [79]. Similarly, bound states in the continuum (BICs) have been shown to underpin many fundamental oscillatory phenomena [16] and can be employed for tailoring the lifetimes of resonant wave systems [80]. Initially discovered in quantum physics [50] and also found in acoustics [81, 82] and ocean science [53], BICs have emerged as an intriguing concept in optics [54, 55, 24]. In all-dielectric subwavelength structures, radiative losses of BIC-based systems can be precisely controlled by tailoring interferences of the constituent resonant modes, producing sharp resonances with extremely high values of the quality factors (Q factors). The BIC concept has therefore been employed for a variety of applications driven by such spectrally selective nanosystems, including multiplexed biospectroscopy [77, 83, 27], high-harmonic generation [30, 29], and sub-wavelength lasing [26, 84, 85].

Two of the principal BIC implementations in nanophotonics are supercavity modes in single structures such as isolated nanoantennas [23] (see Fig. 4.1D) and resonances in symmetry-protected metasurfaces [15] (Fig. 4.1A and B). Although single BIC structures offer a minimal footprint, careful electromagnetic engineering is required to satisfy the mode interference conditions of the hybridization of the Mie and Fabry-Pérot modes [22], restricting design flexibility and limiting the achievable Q factors. Based on these design constraints, such interference modes can only be excited with structured light illumination, further increasing experimental complexity. Moreover, the resonantly enhanced electric near fields are predominantly confined inside the structures, which is advantageous for material-intrinsic processes such as higher harmonic generation, but severely limits surface-driven light-matter interactions and sensing applications.

In contrast, metasurfaces based on all-dielectric resonators with broken in-plane inversion symmetry (Fig. 4.1A) offer both high Q factors and strong near fields that extend considerably outside of the resonators, enabling cutting-edge applications in sensing [28, 27] and enhanced light-matter interaction [29, 86, 87]. Significantly, symmetry-broken quasi-BICs (qBICs) provide straightforward tunability of the resonance position and Q factor via the geometrical scaling factor of the unit cell [27] and the degree of asymmetry for increased design versatility. However, they require specific excitation polarizations and their lateral on-chip footprints of metasurfaces supporting qBIC resonances in the visible spectrum usually exceed 100 μm^2 [30, 28], holding back their potential for device miniaturization, on-chip multiplexed sensors, and hybrid nanophotonic systems such as interactions with micron-sized individual layers of two-dimensional (2D) materials. Although their spatial extent can be reduced by transforming the system into a one-dimensional chain (Fig. 4.1B), this comes at a significant cost in terms of Q factor [88].

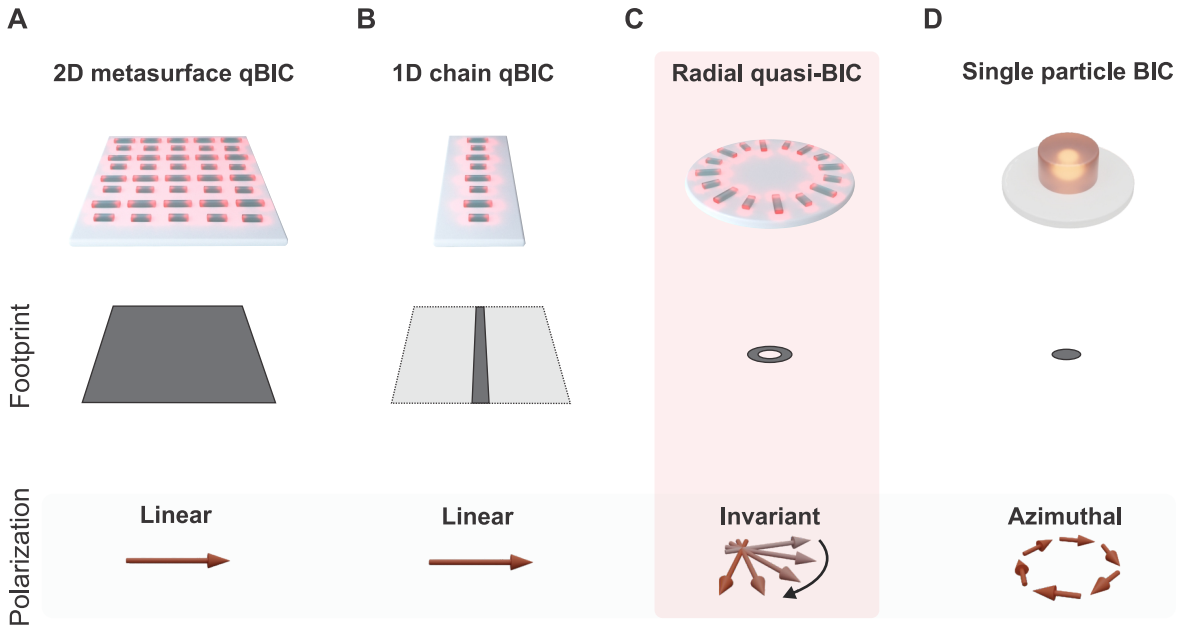

Figure 4.1.: Conceptual advantages of radial quasi-bound states in the continuum (radial BICs). Established symmetry-broken quasi-BIC geometries, such as 2D metasurfaces (**A**), and 1D chains (**B**), exhibit large footprints, moderately high Q factors and require polarization-dependent excitation. Single particle BICs (**D**) exhibit small footprints but require complex excitation conditions. The radial BIC platform (**C**) combines a tiny footprint with high Q factors in the visible. Above all, the radial BIC platform provides the highest Q factor per footprint ratio compared to other 1D and 2D symmetry-broken BIC-based platforms as shown here.

Here, the concept of radial bound states in the continuum (radial BICs) is introduced as a multi-application platform for sustaining polarization-invariant high-Q resonances with high surface sensitivity in a compact footprint. These symmetry-protected and radially distributed electromagnetic states are accessed through a carefully designed ring structure incorporating symmetry-broken double rod unit cells, where individual resonators are rotated to satisfy radial alignment (Fig. 4.1C). In contrast to previous 2D or 1D resonator arrangements, the approach leverages a semi-infinite ring geometry [89, 90], enabling a polarization-invariant optical response and avoiding edge effects. Owing to this unique arrangement, the coupling between neighboring elements over the entire ring is greatly improved for the radial BIC, resulting in much higher Q factors compared to metasurface-based BICs in an 8x8 (blue curve) and 5x5 (black curve) array as apparent from the numerical simulations in Fig. 4.2A. These numerical calculations are performed in the frequency domain by obtaining full-wave solutions of Maxwell's equations using the commercially available RF module of the finite element solver COMSOL Multiphysics. Port boundary conditions are employed for the excitation of the structures and perfectly matched layers (PML) domains for the absorption of propagating waves. A dispersion less refractive index of $n = 1.45$ was employed for the SiO_2 substrate, while the dispersive refractive index of the amorphous silicon film, as measured via ellipsometry (see Fig. 3.3), was used for the resonators.

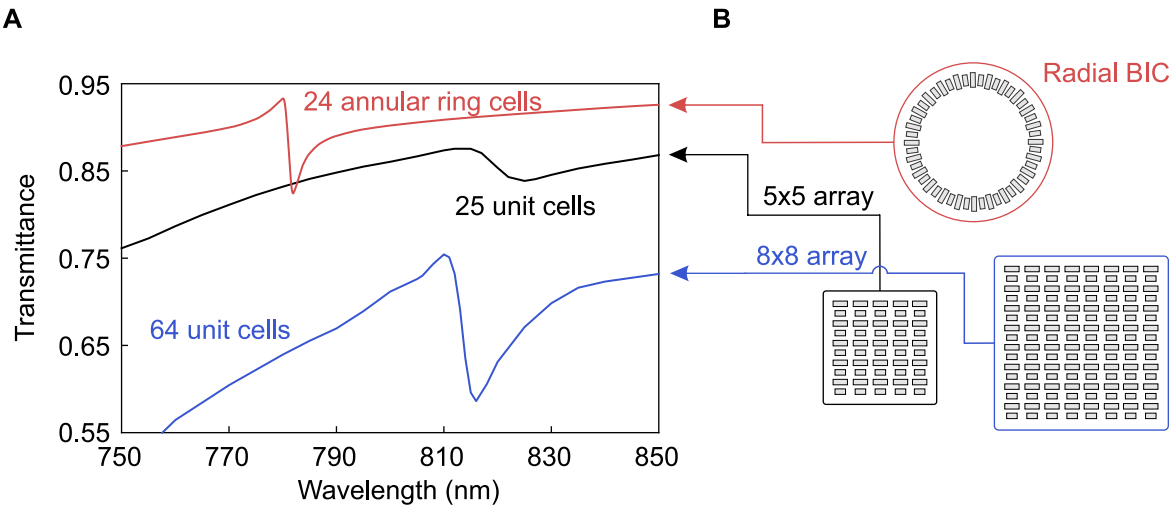

Figure 4.2.: Advances of the annular unit cell arrangement. (**A**) Numerical investigation of the difference between resonator arrays of 8x8 (blue curve) and 5x5 (black curve) unit cells arranged in a two-dimensional BIC metasurface compared to 24 unit cells (red curve) arranged in an annular fashion, showing the highest resonance Q-factors for all systems regarded here. (**B**) Sketches of the simulated metasurfaces geometries.

One of the key parameters to control the optical characteristics of the radial BIC mode is the asymmetry parameter ΔL, *i.e.*, the length difference between the two constituent rods of the unit cell. In the symmetric case ($\Delta L = 0$), a BIC-like state is observed, which is decoupled from the radiation continuum and exhibits negligible electromagnetic near-field enhancement (Fig. 4.3C and black curve in Fig. 4.3A). Notably, even though neighboring resonators are set at a small angle with respect to each other, the radial arrangement of rods with identical lengths leads to a non-radiating BIC state with negligible coupling to the far field. For non-zero asymmetry ($\Delta L > 0$), the C_{2z} symmetry is broken and, hence, the BIC transforms into a radial quasi-BIC (radial BIC) mode. This mode can be accessed by the far field, demonstrating strong field enhancements and the characteristic field pattern of opposing electric dipoles observed in asymmetric metasurfaces [15] (Fig. 4.3C). The field normalization was performed considering the solution obtained for the sum of the in-plane components of the electric field ($E_x + E_y$) using as a reference the smallest chosen asymmetry ($\Delta L = 25$nm) to highlight the reduction in field enhancement for larger asymmetries.

Due to the engineered inter-resonator coupling within the ring, linearly polarized light efficiently couples to the full radial BIC mode extended along the ring and excites spectrally distinct resonances with high Q factors (Fig. 4.3A and Fig. 4.3B). The numerical calculations confirm the presence of highly enhanced near fields outside the resonator volume and highlight how the field magnitude can be tailored via the structural asymmetry as apparent from Fig. 4.3C. Obviously, a clear correlation between the electric near fields and the values of the Q factors exists, where the lowest asymmetry is associated with the maximum values of both parameters. Here, the radial BIC system is engineered to exhibit high-Q resonances at around 770 nm in the red part of the visible wavelength range.

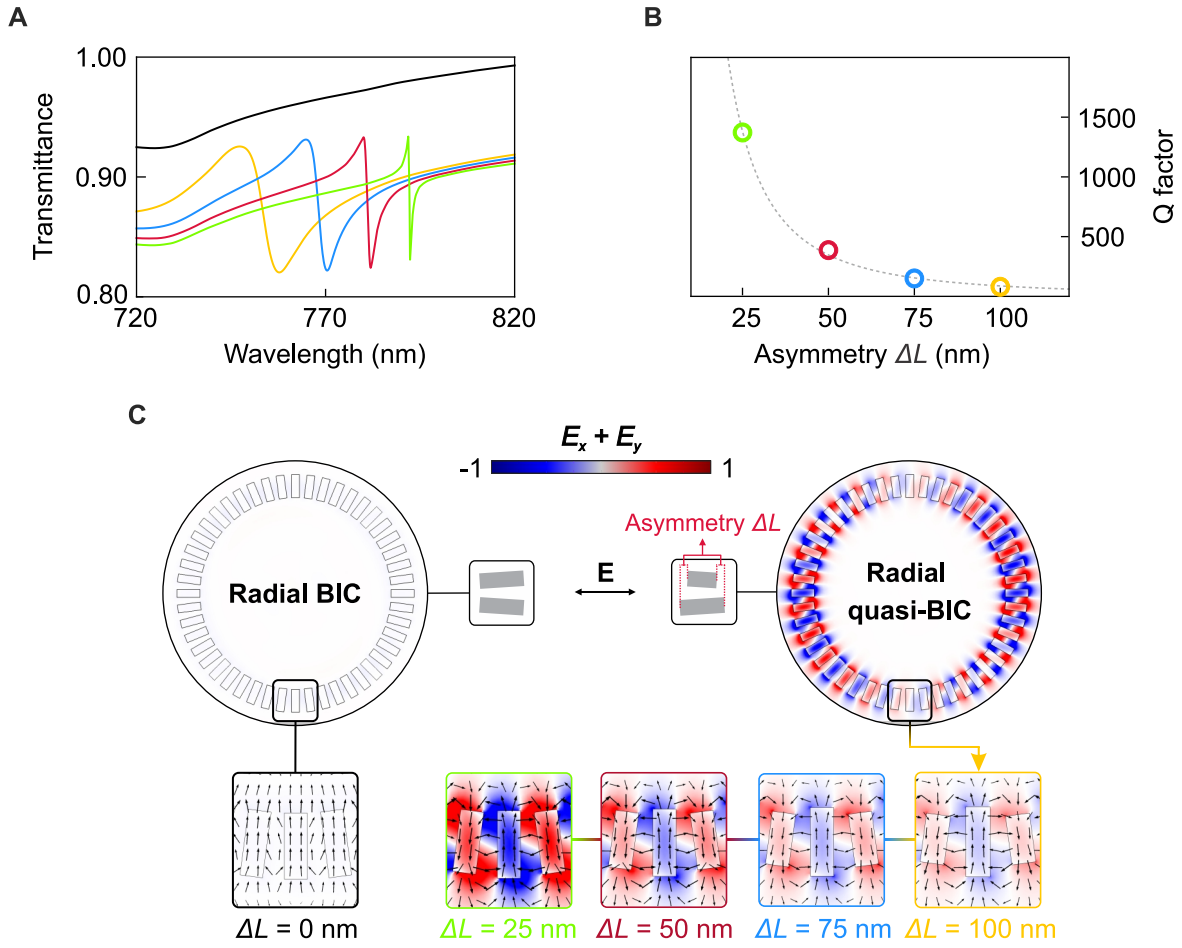

Figure 4.3.: Spectral and near-field investigation of the radial BIC mode. (**A**) Simulated transmittance spectra of radial BIC structures with different asymmetries for a radius R = 1.5 µm, where the black response (shifted for clarity) corresponds to the symmetric case. (**B**) Extracted Q factors for the spectra shown in (**A**) follow the well-known ΔL^{-2} behavior (fitted as gray dashed line). (**C**) Simulated electric near fields for a symmetric ring ($\Delta L = 0$ nm) on the left and a variety of different asymmetries on the right at the spectral position of the respective radial BIC mode. Apparently, the magnitude of the electric field increases for decreasing asymmetry.

4.1.2. Full experimental characterization of radial BICs

Symmetry-broken ring structures with varying geometry are fabricated from 120 nm thick amorphous silicon on a glass substrate using electron beam lithography and reactive ion etching (see Methodology part for details). All measurements shown are based on ring structures with 24 annular unit cells and a base rod length $L_0 = 335$ nm with width $w = 115$ nm except stated differently. The symmetry-breaking is introduced by shortening one rod within the unit cell as indicated by the corresponding asymmetry parameter ΔL. The choice of the asymmetries is based on a trade-off between highest Q factors (and associated strong near fields) and the resulting modulation of the radial BIC resonances in the optical experiments.
Although higher field enhancements and ultrahigh Q factors are numerically predicted

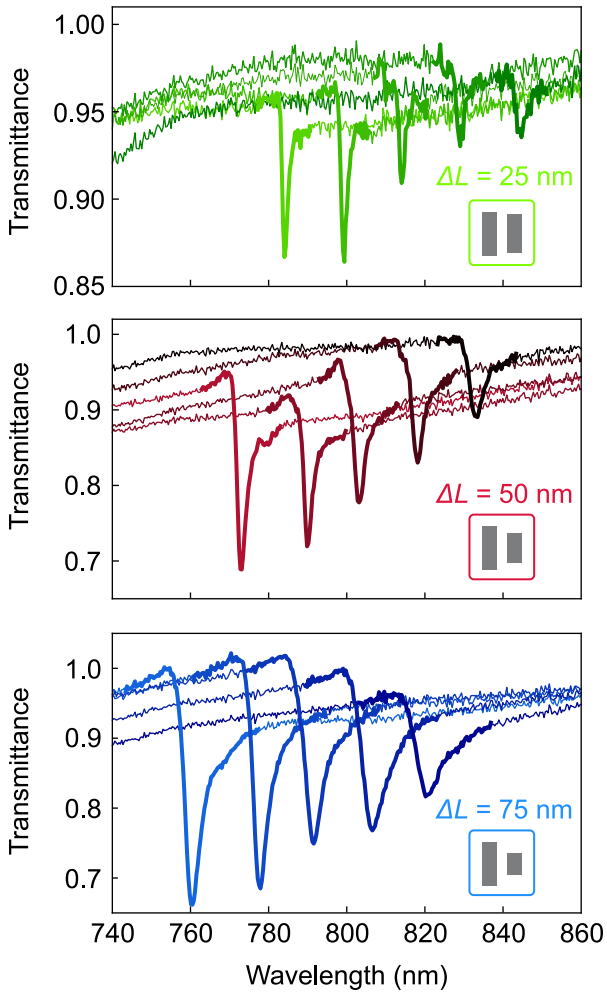

Figure 4.4.: Full white-light transmittance spectra for different asymmetries. Optical transmittance spectra of the radial BIC geometry with different ring radii increasing from 1.4 (smallest resonance wavelength) to 1.8 (largest resonance wavelength) μm for an asymmetry of ΔL = 25 nm (green color code), ΔL = 50 nm (red color code), and ΔL = 75 nm (blue color code). For the smallest asymmetries, the highest Q factors are observed, exceeding 500.

for asymmetries approaching $\Delta L = 0$ nm (see Fig. 4.3B), an optimum parameter range is found for asymmetry values around $\Delta L = 25$ nm, taking into account nanofabrication accuracy and the noise characteristics of the spectroscopy setup.
The optical characterization of the radial BIC structures is conducted with a commercial white light transmission microscopy setup (WiTec alpha300 series). The samples are illuminated with collimated white light from the backside and the transmitted signal is collected with a 50x objective (NA = 0.8). The collected light is focused into a fiber which is coupled to a grating-spectrometer equipped with a silicon CCD camera that is used to acquire white light transmittance spectra. All the transmittance spectra shown are referenced to the bare SiO_2 substrate.
At first, the optical response of the radial BIC structures with different radii R is examined and found that precise tuning of the resonance wavelength is provided via the ring

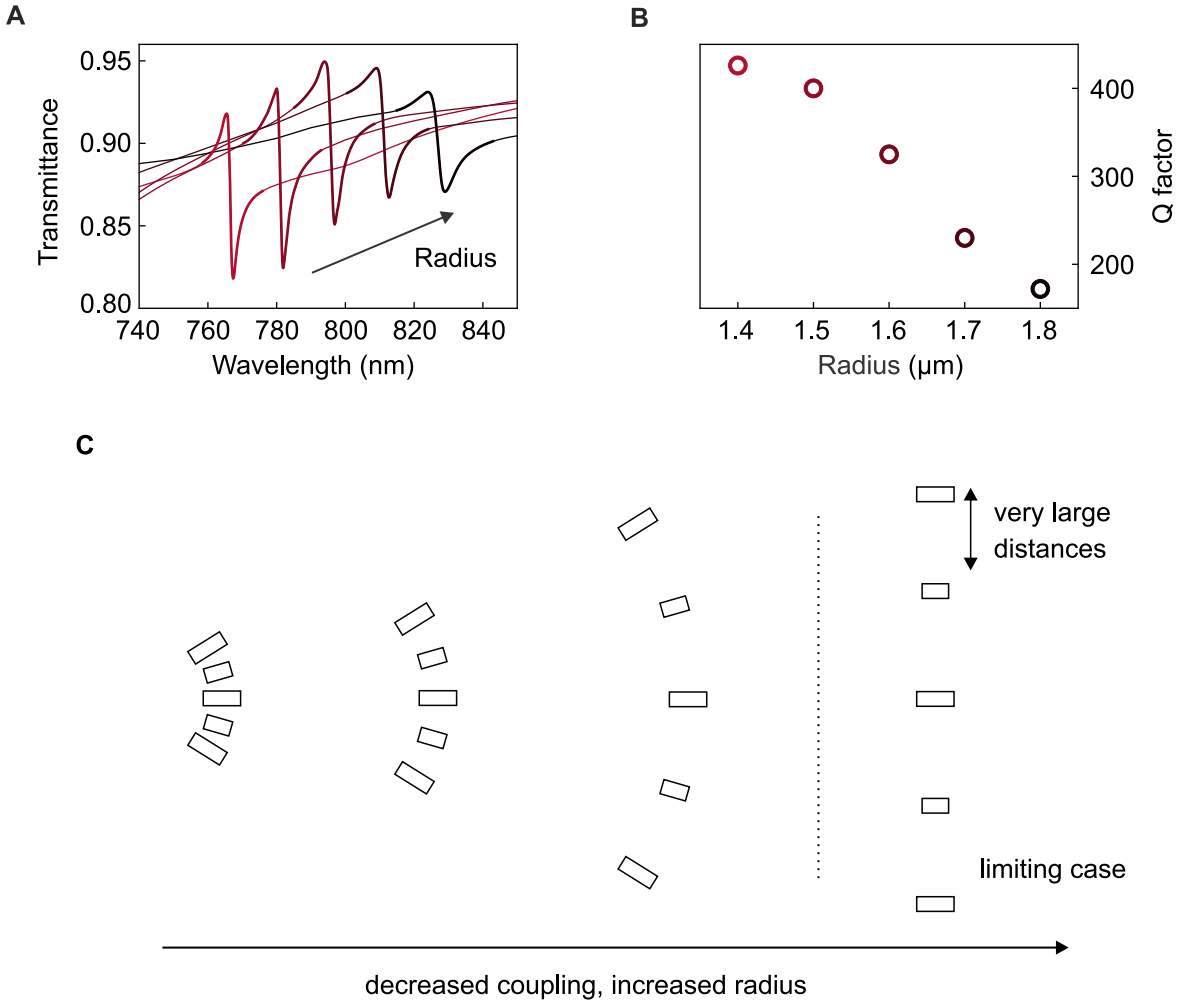

Figure 4.5.: Simulated spectral radial BIC responses for different radii. (**A**) Simulated transmittance spectra of radial BIC structures with different radii ranging from $R = 1.4$ μm to $R = 1.8$ μm for $\Delta L = 50$ nm. (**B**) Extracted Q factors for the spectra shown in (**A**), showing the highest Q factor for the smallest radius. (**C**) The decreasing Q factors for increasing radii are associated with larger spacing between individual rod resonators and thus decreased inter-rod coupling, hampering the mode formation.

radius as depicted in Fig. 4.4. In particular, the energy of the radial BIC resonances is decreased for higher radii which is in line with the theoretical predictions in Fig. 4.5A. Furthermore, the reduced resonance Q factors (see Fig. 4.5B) are associated with the decreased inter-rod coupling between adjacent resonators as illustrated in Fig. 4.5C.

For the determination of the Q factors of the radial BIC resonances, a temporal coupled mode theory model [73] is employed where the Q factor is defined as

$$Q = \frac{\lambda_{\text{res}}}{2\gamma}, \tag{4.1}$$

with the resonance wavelength λ_{res} and the linewidth γ of the resonance. Subsequently, each extracted Q factor is plotted versus the asymmetry and the radius of the

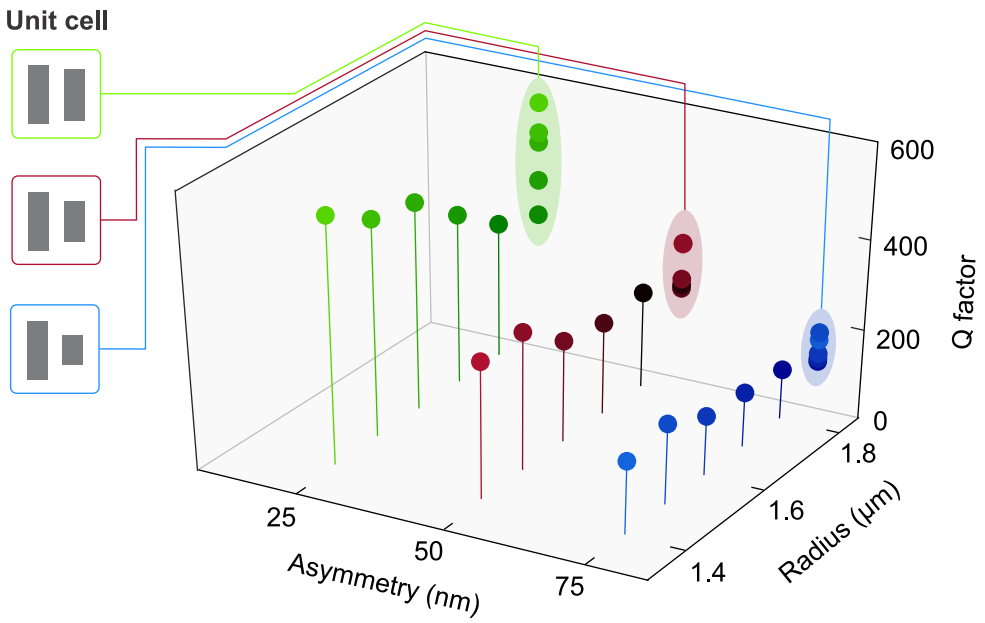

Figure 4.6.: Dependence of the quality factor on the ring radius R and the unit cell asymmetry ΔL. Quality factors exceed 500 for $\Delta L = 25$ nm in the visible wavelength range.

respective ring as depicted in Fig. 4.6. Consistent with the numerical simulations, the highest resonance sharpness is observed for the smallest values of the asymmetry ΔL with Q factors exceeding 500. In fact, the measured Q factors are among the highest reported in the literature for symmetry-broken metasurfaces in the visible spectral regime [28, 34].
In order to put the obtained Q factors more into context, the results are compared with values reported in the literature and overviewed in Table 4.1. Three classes are distinguished for simplicity here: accidental and photonic-crystal-based qBICs, qBICs emerging from strongly coupled photonic modes in individual subwavelength resonators, and symmetry-broken qBICs.

So far, photonic-crystal-based approaches have shown the highest quality factors, with specific examples reaching around 10^6 [24]. However, they rely on grating-based approaches and lack flexible tunability of the resonances. Quasi-BICs emerging from strongly coupled modes possess the lowest footprints since the do not rely on array-based approaches [23]. Nevertheless, these resonators have been limited to experimental Q factors below 200, often require complex optical excitation with structured light, and exhibit near fields that are located inside the structures, reducing the spatial overlap with analytes and thus the sensing performance.
In contrast, symmetry-broken BICs show exceptional resonance tunability and sustain high-Q resonances down to smaller array sizes [91]. In this study, a record Q factor of roughly 18500 for symmetry-broken BICs was achieved. For better comparison, some representative works in the field of BIC-based nanophotonics are shown in Table 4.1. From the table, it is clear that the radial BIC possesses the smallest footprint and thus the highest Q factor vs. footprint ratio apart from the single disk BIC. The single par-

	Ref. [91]	Ref. [25]	Ref. [24]	Ref. [23]	This work
BIC mechanism	Symmetry-broken	Accidental	Photonic Crystal	Strong mode coupling	Symmetry-broken
Excitation	Lin. pol.	Lin. pol	Lin. pol	Structured	Lin. pol
Resonance wavelength	**IR**, 1490 - 1550 nm	**NIR**, 825 - 842 nm	**VIS**, 570 - 850 nm	**IR**, 1500 - 1600 nm	**VIS**, 700 - 850 nm
Quality (Q) factor	500 - 18511	2750	10^6	Up to 200	100-500
Footprint (μm^2)	10.6 - 308	24000	10^8	0.62	2.7
Q / footprint	66 - 117	0.11	0.01	322	186

Table 4.1.: Record Q factors of different BIC metasurfaces with the corresponding geometrical footprints and resonance wavelengths.

ticle BIC is mentioned above but excluded here due to the complex optical excitation conditions and unsuitable near-field distributions for sensing applications [25, 28]. In fact, comparing the same number of unit cells with Ref. [91], the radial BIC exhibits the same quality factor although confined to a much smaller footprint and sustains resonances in the visible where material losses and fabrication imperfections – in contrast to the NIR region – pose significant challenges. In fact, the simulations carried out for the radial BIC geometry demonstrate that the ring arrangement of unit cells is favored compared to the arrangement in a 2D array (see Fig. 4.2A).

Apart from the tailorability of the radial BIC Q factors, the versatile design provides additional degrees of freedom for tailoring the resonance, such as the number of unit

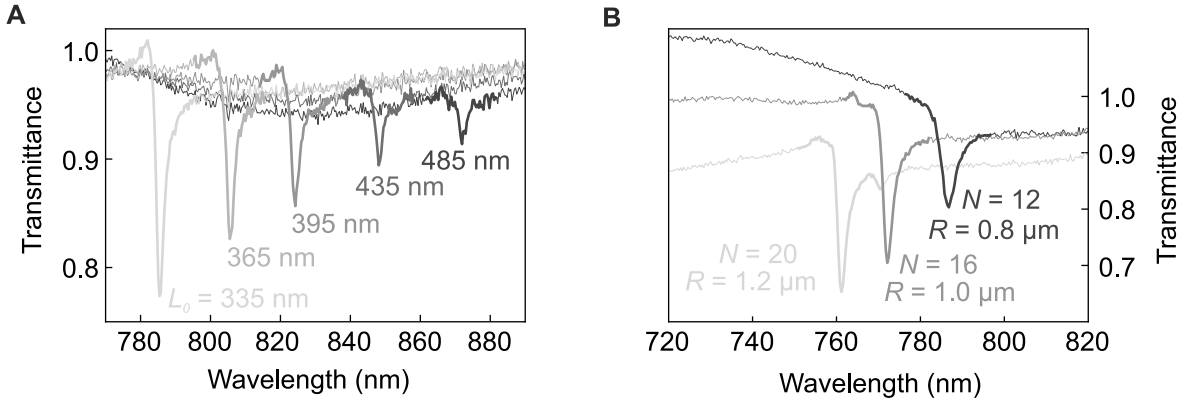

Figure 4.7.: Influence of base rod length L_0 and number of unit cells on the optical response of the radial BICs. (**A**) Measured transmittance spectra for increasing base rod length L_0 for an asymmetry of $\Delta L = 50$ nm. A red-shift of the radial BIC resonance is observed for higher base length. (**B**) White light transmittance spectra for different number of unit cells with $\Delta L = 50$ nm. The Q factor decreases for fewer unit cells due to decreased inter-rod coupling.

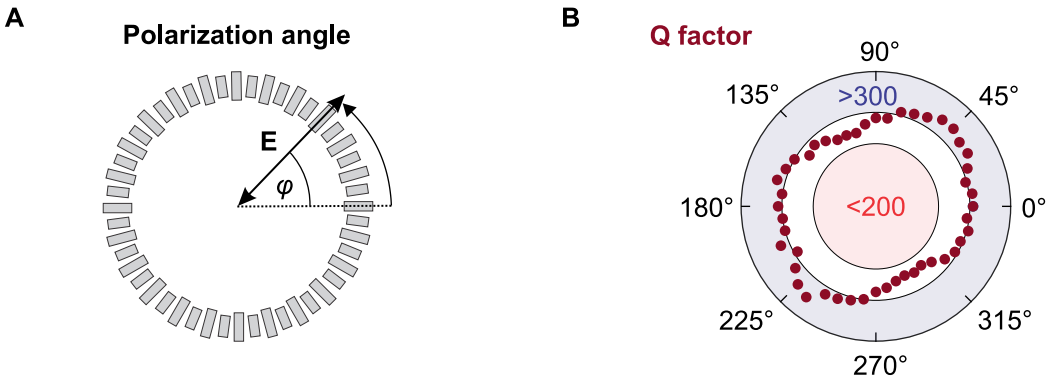

Figure 4.8.: Observation of polarization-invariant excitation of the radial BICs. The radial BIC geometry shows polarization invariance as observed by the weak dependence of the resonance quality factor on the polarization angle φ of the incident light.

cells constituting the ring and the base length L_0 of the all-dielectric rods as demonstrated in Fig. 4.7. As apparent from Fig. 4.7A, increasing lengths of the individual rods lead to pronounced resonance red-shifts. Remarkably, quasi-BIC resonances are observed down to $N = 12$ unit cells (Fig. 4.7B) which corresponds to 24 single resonator elements that constitute the BIC mode. Owing to the increased angles between adjacent resonators for a decreased number of unit cells, the resonance modulation and Q factor are reduced.

Strikingly, the annular arrangement of the resonator elements renders the Q factor mostly invariant under rotations of the incident polarization direction of light [92], maintaining a value above 200 throughout the angular range (Fig. 4.8). To elaborate the polarization invariance in more detail, the explanation is split into two parts, the inter-unit cell and intra-unit cell contribution.
First, for the inter-unit cell polarization invariance, it is clear that the ring possesses a C_{24} symmetry owing to the 24 unit cells of the structure, meaning that a rotation by

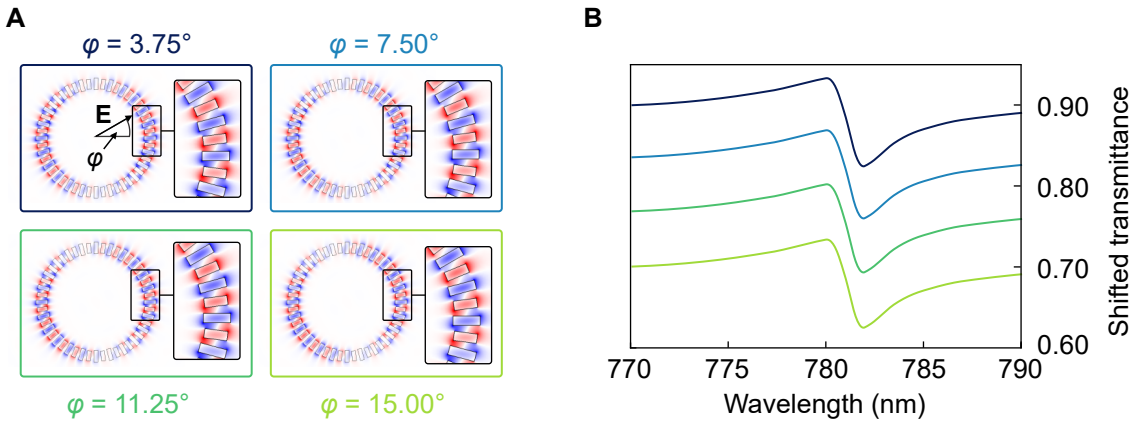

Figure 4.9.: Influence of the incidence angle on the mode formation. (**A**) Electric near fields for different linear polarizations φ of the incident light showing no differences in the mode itself. (**B**) The corresponding numerical spectra for the different incidence angles exhibit the same resonance position and Q factor as well as resonance modulation.

$360°/24 = 15°$ will congruently transform the ring onto itself. As a result, for every polarization angle φ_0 the radial BIC will exhibit the same optical far-field response for all angles $\varphi_n = \varphi_0 \pm n \cdot 15°$, where n are the integers. Even though the far-field response is identical, the maximum of the near-field patterns depend on the polarization angle φ as experimentally verified from the polarization dependent SHG maps in Fig. 4.17. Second, the intra-unit cell polarization invariance for polarization angles $0° \leq \varphi \leq 15°$ is considered within one unit cell. As a proof, the near-field patterns and optical far-field responses were numerically calculated for different polarization angles within this range, which are depicted in Fig. 4.9. As obvious from panel 4.9A and 4.9B, the different polarization angles neither change the mode structure and mode formation nor impact the spectral response of the radial BIC. As a result, it is concluded that the spectral response is also invariant within the radial BIC unit cell. Considering an arbitrary polarization angle, the spectral response will thus be unchanged.
Combining the intra- and inter- unit cell polarization invariance, the spectral response of the radial BIC in general is polarization invariant as a whole for an arbitrary incidence angle φ.

4.2. Biomolecular sensing using radial BICs

One way to utilize the ability of photonic nanostructures to convert incoming far-field radiation into highly enhanced localized near fields is to probe the refractive index in the vicinity of the nanostructures. Mediated by the coupling between the interfaced sensing specimen and the highly enhanced local near fields, minute changes of the surrounding can be monitored [28]. In fact, different environmental conditions, such as another coverage layer and thickness or different biomolecular species and concentrations, will alter the effective refractive index around the nanostructures which manifests itself in a far-field resonance shift as depicted in Fig. 4.10A. Via this far-field resonance shift, the amount of the specimen can be deduced. Usually, to determine the capability of a nanophotonic biosensor, the refractive index sensitivity is characterized first.

4.2.1. Refractive index sensitivity

As an initial step, to assess the refractometric sensing performance of the radial BIC, the local refractive index around the ring structure is varied by means of magnetron sputtering of conformal silicon dioxide (SiO_2) thin films with increasing thicknesses. Pronounced resonance shifts for all asymmetries can be detected dependent on the SiO_2 layer thicknesses (see Fig. 4.10B). For the calculation of the bulk refractive index sensitivity S_B (BRIS), the resonance shifts mediated by the thin films are converted by taking into account the decay length of the resonators and the film thickness from the surface sensitivity [93]. First, the surface sensitivity S_S is calculated as

$$S_S = \frac{\Delta\lambda_{\text{res}}}{\Delta n_S}, \tag{4.2}$$

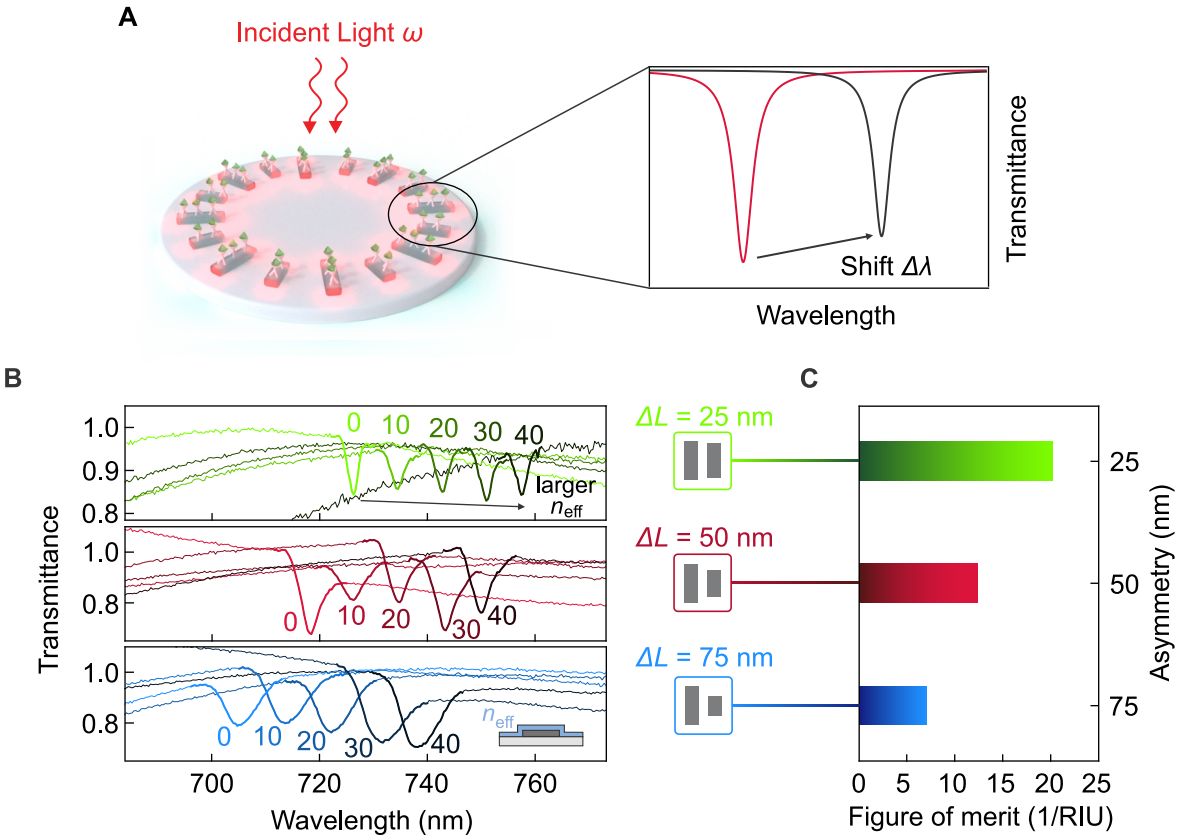

Figure 4.10.: Refractive index sensing. (**A**) Principle of refractive index sensing. Incident light excites the sharp radial BIC resonances that are extremely sensitive to the dielectric surrounding. As a consequence, resonance shifts can be related to the presence of biomolecular species or change of surrounding refractive index in general. (**B**) Radial BIC resonances with different asymmetries ΔL exhibit distinct spectral shifts when covered with increasing thicknesses of SiO_2 thin films (numbers are thicknesses in nm). From these shifts, a figure of merit (FOM) can be calculated for each asymmetry which is depicted in (**C**).

where n_S is the refractive index of the conformally deposited SiO_2 thin film. Usually, the sensitivities are normalized by the respective Q factor of the resonance since it is easier to retrieve small resonance shifts with sharper resonances. For this purpose, the figure of merit for the surface sensitivity is defined as

$$\mathrm{FOM}_S = \frac{S_S}{\mathrm{FWHM}}, \tag{4.3}$$

where FWHM is the full width at half maximum of the radial BIC resonance. From the figure of merit for the surface sensitivity, it can be inferred on the figure of merit for bulk refractive index sensitivity [93] via

$$\mathrm{FOM}_B = \frac{\mathrm{FOM}_S}{1 - \exp(-2h/l_d)}, \tag{4.4}$$

with the film thickness h and the decay length l_d. From the simulations, a decay length $l_d = 44.7$ nm is obtained. With the help of these values and equations, the FOM for bulk refractive index sensing is derived for each asymmetry ΔL as shown in Fig. 4.10C.

Work	Ref. [94]	Ref. [95]	Ref. [28]	This work (exp.)	This work (num.)
Platform	Gold nanohole array	All-dielectric Fano metasurface	Symmetry-broken BIC	Radial BIC	Radial BIC
Sensitivity (nm RIU^{-1})	700	289	263	40	188
FOM (RIU^{-1})	160	103	40	22	2243

Table 4.2.: Overview of biosensitivities for different sensor platforms, data taken from [96].

Based on these BRIS values, it is found that the resonance figure of merit (FOM, BRIS divided by resonance full width at half maximum, FWHM) is clearly correlated with the asymmetry of the radial BIC structures. The highest FOM of above 20 per refractive index unit (RIU) is observed for the lowest asymmetry (Fig. 4.10C). The FOM values of the radial BIC geometry for refractive index sensing are mostly comparable with large array-based approaches relying on symmetry protected metasurfaces [28], despite the much smaller footprint. Nevertheless, the FOM can be substantially boosted by utilizing even smaller asymmetries or by further engineering the inter-rod coupling, e.g. by optimizing the resonator shape.

To put the performance of the radial BIC sensor more into context, some representative sensitivities are shown in table 4.2 along with the sensitivities and FOM obtained from this experimental study. Importantly, through a further optimization of the nanofabrication processes, the losses of the radial BIC sensor platform can be greatly reduced, leading to improved Q factors and a higher FOMs.

To estimate the potential of the geometry, numerical data for the sensitivity of the radial BIC platform are presented in Fig. 4.11. For an asymmetry of $\Delta L = 5$ nm, which is estimated to be the minimum achievable asymmetry, a sensitivity of $S = 188$ nm/RIU is obtained, which compares with recently established numerical values (see Ref. [97]) of 440 nm/RIU for extended 2D arrays of symmetry-broken BIC resonances. The corresponding FOM for the radial BIC platform was calculated as FOM = S/FWHM = 2243 RIU^{-1}.

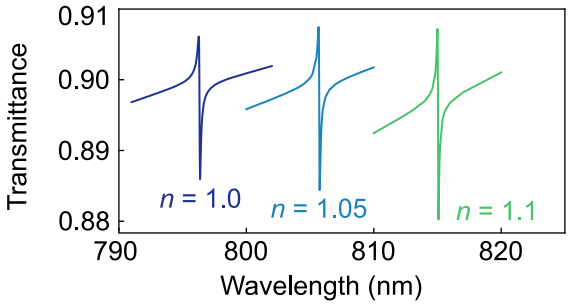

Figure 4.11.: Simulated refractive index sensitivity. Simulated radial BIC responses using $\Delta L = 5$ nm for different surrounding refractive indices indicate an FOM = 2243 RIU^{-1}.

4.2.2. Biomolecular sensing performance

For the implementation of a model multi step bioassay, the structures are first functionalized with (3-Aminopropyl) triethoxysilane (APTES), followed by the attachment of biotin capture molecules and the binding of different concentrations of streptavidin protein. After each step, a clear redshift of the radial BIC resonance is observed (Fig. 4.12A), induced by the increased amount of molecules on the surface and the associated increase of the environmental refractive index. To compare the biomolecular sensing performance for all asymmetries, the resonance shift is normalized by the respective FWHM and plotted for each streptavidin concentration to obtain a map of biomolecular sensing performance (Fig. 4.12B).
Notably, a clear and concentration-dependent sensor performance over a broad range of concentrations and resonance linewidths is apparent. Depending on the experimental light sensitivity and thus the required resonance modulations as well as spectral resolution, a wide parameter space is demonstrated for picking the appropriate structural asymmetry. Especially field-deployed applications with low spectral resolution may require resonances with smaller Q factors – when pushing for highest sensitivity, high-Q resonances and consequently a high FOM is favored. The versatile platform allows to cover all such use cases in an ultrasmall footprint.

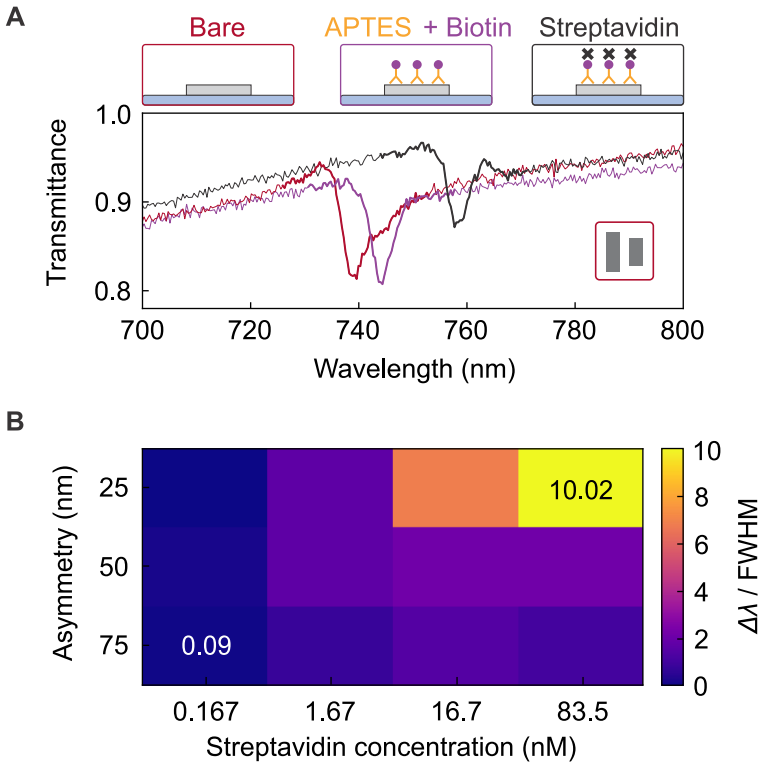

Figure 4.12.: Molecular biosensing with radial BICs. (**A**) Transmittance spectra for a ring with $\Delta L = 50$ nm and $R = 1.6$ μm after each functionalization and molecular binding step as indicated in the color-coded boxes. (**B**) Map of biomolecular sensing performance. Measured resonance shifts normalized to the respective FWHM for three different asymmetries dependent on streptavidin concentrations.

4.3. Radial BIC-enhanced second harmonic generation

Another way to utilize the highly-enhanced near fields is to couple 2D materials, which will be introduced in detail in the next chapter, to the nanophotonic surface. Mediated by the highly enhanced electric near fields, that are provided by the resonantly excited nanostructures, nonlinear optical effects, such as higher harmonic generation will be greatly enhanced.

4.3.1. Introduction to nonlinear optics

In order to comprehend higher harmonic generation, it is insightful to consider the dielectric polarization within a medium caused by an incident light wave. For this purpose, it is convenient to represent the time-dependent polarization $\boldsymbol{P}(t)$ as a Tailor series of different contributions

$$\boldsymbol{P}(t) = \varepsilon_0 \left(\chi^{(1)} \boldsymbol{E}(t) + \boldsymbol{\chi}^{(2)} \boldsymbol{E}^2(t) + \boldsymbol{\chi}^{(3)} \boldsymbol{E}^3(t) + O(\boldsymbol{E}^4) \right), \tag{4.5}$$

where $\chi^{(1)}$ is the linear susceptibility and $\boldsymbol{\chi}^{(2)}$ and $\boldsymbol{\chi}^{(3)}$ are the nonlinear susceptibilities and are tensors in general. In essence, the incident light drives a polarization $\boldsymbol{P}$ in the medium that is usually linearly dependent on the incident field $\boldsymbol{E}$. Nevertheless, if the strength of the incident light is very high, for instance for a laser, nonlinear contributions to the polarization need to be included. In the case of second harmonic generation (SHG), two incident photons with frequency ω are absorbed by the nonlinear material and converted to a single photon with frequency 2ω as depicted in Fig. 4.13.
The emergence of SHG can be easily understood by considering a time-harmonic incident field given as

$$\boldsymbol{E} = \boldsymbol{E}_0 e^{-i\omega t} + \boldsymbol{E}_0{}^* e^{+i\omega t}. \tag{4.6}$$

The corresponding second order polarization is then given as

$$\boldsymbol{P}^{(2)} = 2\varepsilon_0 \chi^{(2)} \boldsymbol{E}\boldsymbol{E}^* = 2\varepsilon_0 \chi^{(2)} \boldsymbol{E}_0 \boldsymbol{E}_0{}^* + \left(\varepsilon_0 \boldsymbol{\chi}^{(2)} E_0{}^2 e^{-2i\omega t} + c.c. \right). \tag{4.7}$$

As apparent from eq. 4.7, the second order nonlinear susceptibility contains a constant term, which is referred to as optical rectification and two terms that are oscillating at twice the frequency of the incident light. In fact, these terms are the contributions to the SHG of a nonlinear material.
By utilizing nanophotonic structures, the incident light can be transduced and highly enhanced up to orders of magnitude into local electric fields. This, in turn, boosts the second-order polarization and thus the SHG for any nonlinear material exposed to these highly enhanced fields, such as an evanescently coupled 2D material on the surface of a nanophotonic structure.

One necessary prerequisite for a finite $\chi^{(2)} \neq 0$ is that the material is non-centrosymmetric, *i.e.*, it does not possess an inversion center. Another prerequisite for the

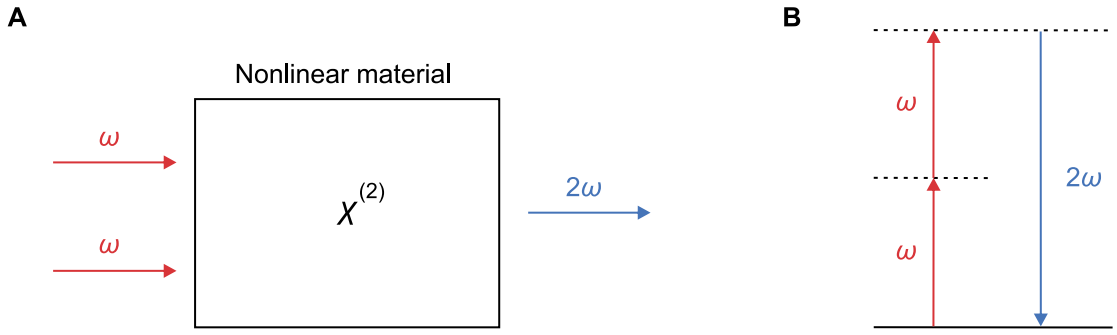

Figure 4.13.: Principle of SHG (**A**) Two incident photons with frequency ω are converted in a nonlinear material $\chi^{(2)} \neq 0$ to a single photon with frequency 2ω. (**B**) Level scheme for SHG.

occurrence of SHG is the interference management between the incident light, which is not converted, and the generated SHG. Since both waves interfere, the thickness of the nonlinear material needs to be adjusted such that both waves do not interfere destructively, a process called phase matching. Since the SHG considered here originates from atomically thin materials, phase matching is not necessary in this case.

4.3.2. Estimation of the SHG enhancement

Prior to the experimental realization, a numerical estimation is performed, investigating which asymmetry provides the highest near-field enhancements and thus the strongest light-matter interaction. To quantify the dependence of the SHG enhancement on the underlying radial BIC asymmetry, a simple estimation of the asymmetry-dependent SHG is given. The normalized electric energy W_V provided by the radial BIC is given by [98]

$$W_V{}^2 = n^2 \int \frac{dV}{V} \frac{E^2}{E_0{}^2}, \tag{4.8}$$

where n is the refractive index of the surrounding medium, V the corresponding near-field volume, and $E^2/E_0{}^2$ the near-field intensity enhancement. The SHG enhancement is proportional to the square of the normalized electric energy and can be compared for different asymmetries. For these calculations a scattering field formulation was employed in simulations, where the linearly-polarized incident, transmitted and reflected waves were defined as the background field.
For simplicity, the refractive index dependence is dropped since the surrounding medium is the same for all asymmetries and thus the refractive index contribution will cancel out. As model system for the SHG, a monolayer of the transition metal dichalcogenide (TMDC) molybdenum diselenide ($MoSe_2$) is chosen. As such monolayer TMDCs provide lattices with broken inversion-symmetry and thus give rise to high SHG [99, 100].

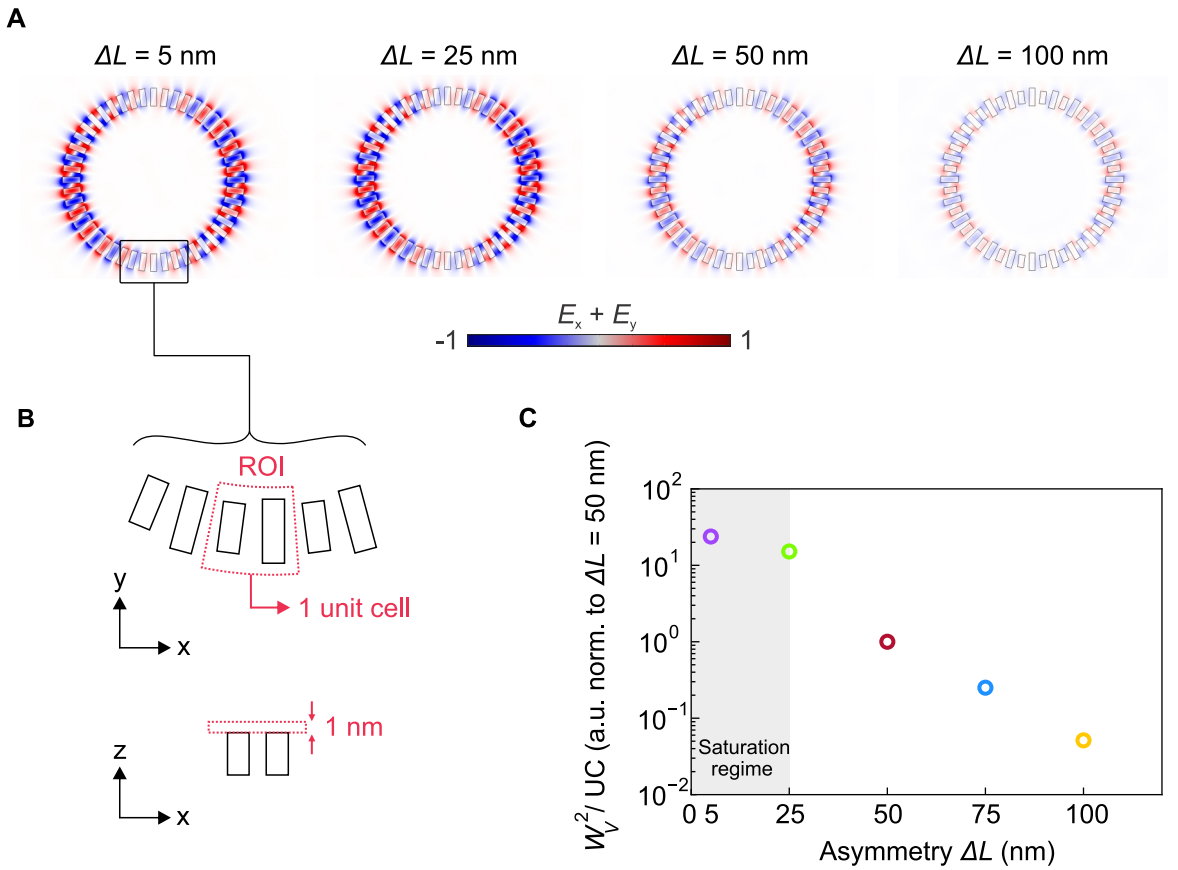

Figure 4.14.: Estimation of the electric energy and SHG. (**A**) Simulated near-field patterns for different asymmetries, all normalized to $\Delta L = 5$ nm. (**B**) Volume considered for the calculation of the normalized electric energy, restricted to one unit cell in plane and to 1 nm in z direction which corresponds to the extent of a monolayer of $MoSe_2$. (**C**) Square of the mean electric energy normalized to $\Delta L = 50$ nm (as used in the experiments) for the region of interest (ROI) defined in (**B**).

As a consequence, the consideration of the normalized electric energy is restricted to a range of interest (ROI) of one unit cell and it is assumed that the monolayer lays completely flat on the surface of the unit cell with a thickness of 1 nm as depicted in Fig. 4.14B.

To provide an estimate of the expected SHG, the calculation of ${W_V}^2$ is performed for different asymmetries within one unit cell (UC) and is normalized to the $\Delta L = 50$ nm case. It is evident from Fig. 4.14A and Fig. 4.14C that the SHG enhancement saturates for asymmetries smaller than $\Delta L = 25$ nm. Considering the fabrication intolerances and detection efficiency of the confocal white light setup, an asymmetry of $\Delta L = 25$ nm would be optimum. Nevertheless, transmittance measurements of the hybrid material system with the monolayer $MoSe_2$ on top of the radial BIC platform could not detect any resonance, probably related to the damping induced by the monolayer.

As a consequence, an asymmetry of $\Delta L = 50$ nm was chosen as a trade-off between high near-field enhancements and sufficient resonance modulation.

4.3.3. Experimental results

To demonstrate the versatility of the design, the radial BIC platform is employed for enhanced light-matter interaction and coupled to a two-dimensional excitonic material [29, 101, 102]. Specifically, enhanced second harmonic generation (SHG) in a non-centrosymmetric monolayer crystal of $MoSe_2$ is demonstrated and localized, facilitated by the highly enhanced electromagnetic near fields that are associated with the radial BIC resonances. For this purpose, a monolayer of $MoSe_2$ is deterministically transfered on top of the radial BIC platform (Fig. 4.16B). Crucially, this experiment is enabled by the low footprint of the radial BIC platform, which allows full spatial overlap between the micron-sized $MoSe_2$ layer and the ultra-compact ring geometry.

The experimental system is depicted in Fig. 4.16A, where the radial BIC platform is displayed covered with the $MoSe_2$ monolayer. The lattice structure of the atomically thin monolayer exhibits a broken inversion symmetry, leading to strong optical nonlinear effects, such as SHG. In order to probe the SHG, the sample is illuminated with a tunable Ti:sapphire femtosecond pulsed laser and the SHG signal is detected after a shortpass filter with an avalanche photo diode detector.

At first, the origin of the observed signal is verified as SHG by increasing the pump power and monitoring the integrated signal from the pure $MoSe_2$ monolayer. As apparent from Fig. 4.15A, the integrated intensity follows a quadratic increase with the input power as indicated by the gray fit line indicating the emergence of non-linear second harmonic light generation. Furthermore, the polarization resolved SHG signal is analyzed for light incident on the pure monolayer. If the excitation polarizer and the detection polarizer are aligned in parallel (∥, blue color code), the characteristic four-fold pattern is observed, as expected from the nonlinear permittivity tensor derived from the symmetry group of the crystal. In line with this, for the cross-polarized situation (⊥, orange color code), the same pattern is observed but with a 45° rotated maximum signal, clearly indicating the signal origin as SHG [103].

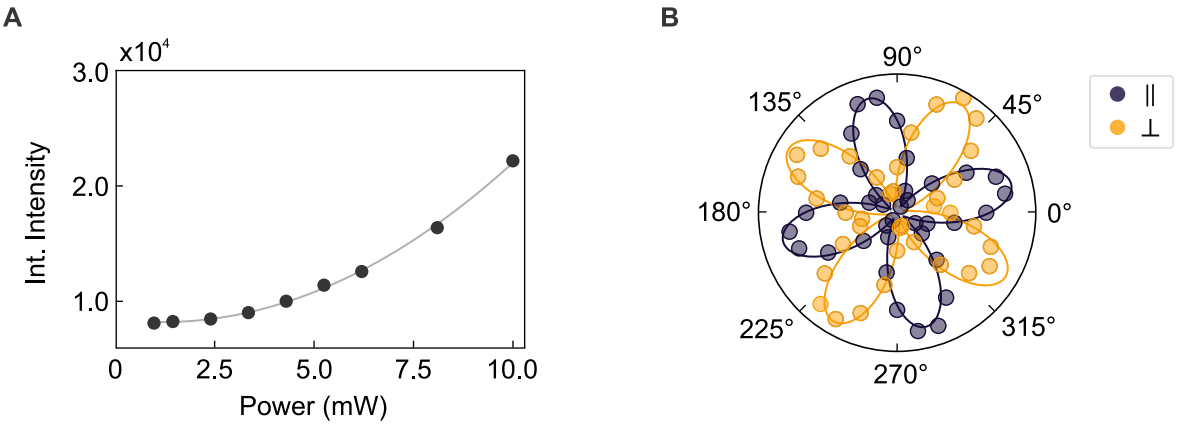

Figure 4.15.: SHG from a $MoSe_2$ monolayer. (**A**) Integrated second harmonic generation (SHG) signal for an excitation wavelength of $\lambda = 744$ nm on the $MoSe_2$ monolayer on a bare substrate showing a quadratic dependence (grey fit line). (**B**) Polarization-resolved SHG signal from the $MoSe_2$ monolayer in either parallel or perpendicular detection geometry.

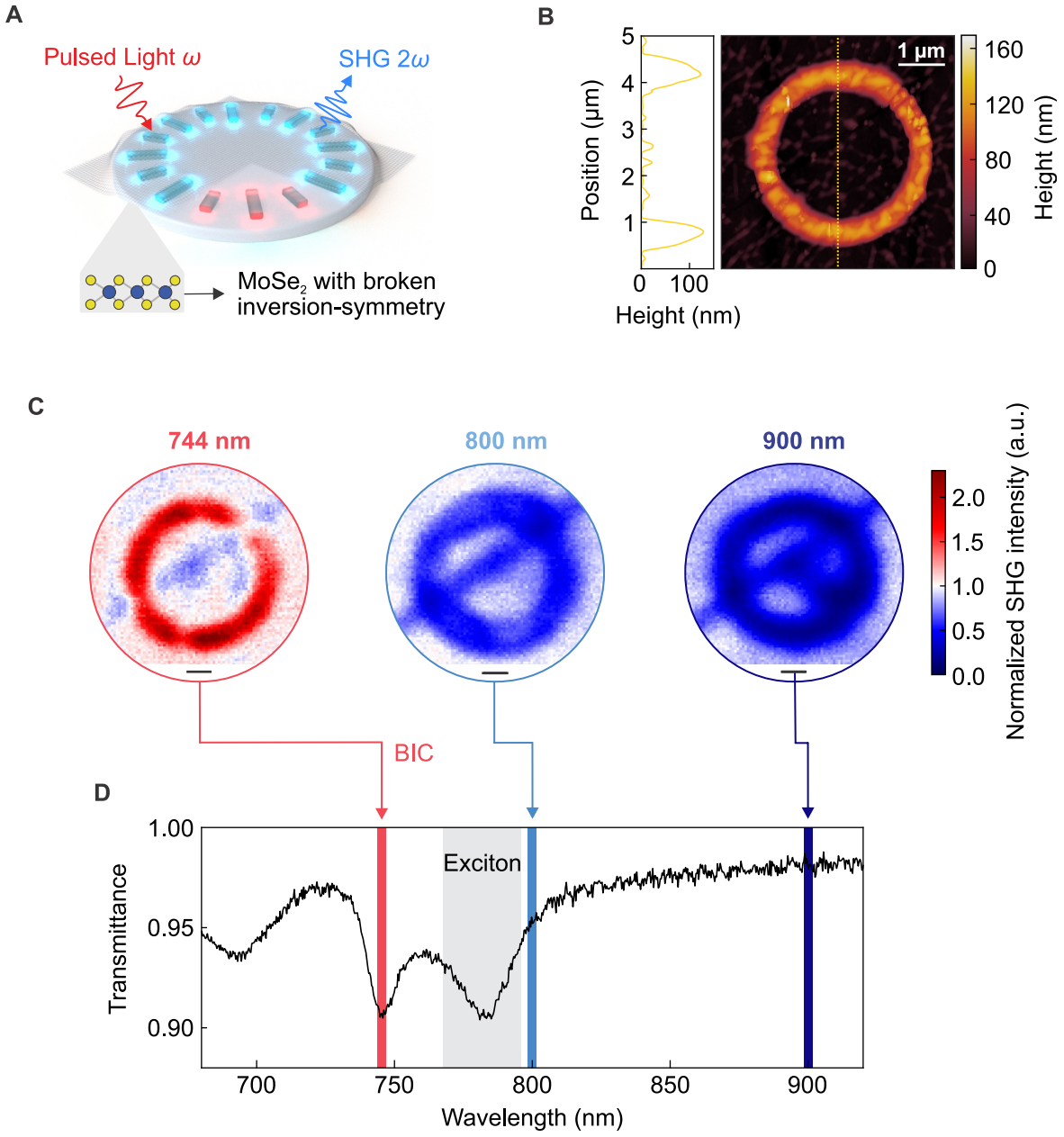

Figure 4.16.: Radial BIC-enhanced second-harmonic generation in a $MoSe_2$ monolayer. (**A**) Schematic depiction of an $MoSe_2$ monolayer covering the ring structures while being illuminated by a pulsed excitation laser. (**B**) AFM image showing the coverage of the flake on top of the ring. (**C**) SHG maps for the ring displayed in panel **B** taken at different excitation wavelengths. SHG enhancement is only present for an excitation wavelength resonant with the radial BIC. In contrast, for the off-BIC excitation, the expected suppression of the SHG signal due to strain is observed. Scale bar: 300 nm. (**D**) Transmittance spectrum of the ring structure ($\Delta L = 50$ nm) covered with $MoSe_2$ monolayer clearly showing the spectral signatures of the radial BIC resonance (744 nm) next to the absorption line of the exciton (785 nm).

After the PDMS dry-transfer of the $MoSe_2$ monolayer with the custom-built stacking setup (see Methodology for details), atomic force microscopy (AFM) imaging confirms the homogeneous coverage of the resonators (Fig. 4.16B) and indicates that the monolayer is in good contact with the silicon structures.

To demonstrate spectrally selective SHG, the coupled system is excited at three different excitation wavelengths via the utilization of a tunable femtosecond pulsed laser (Fig. 4.16C and D). A ring with $\Delta L = 50$ nm was chosen to balance the high near-field enhancements with a sufficient resonance modulation. Although even higher near fields and thus SHG enhancements are expected for smaller asymmetries, such as $\Delta L = 25$ nm, the resonance was diminished by the TMDC monolayer in experiments.

Specifically, as shown in Figure 4.16D, the system is excited at 744 nm, in resonance with the radial BIC mode, at 800 nm, close to the $MoSe_2$ exciton peak, and at 900 nm, spectrally distinct from both the exciton and the radial BIC resonance. For each excitation wavelength, the focused laser beam is rastered across the sample and the SHG signal is directed to an avalanche single photon detector and plotted for each point to obtain an SHG intensity map. The SHG maps shown in Fig. 4.16C are normalized to the bare $MoSe_2$ monolayer flake to guarantee consistency between the measurements and to eliminate wavelength-dependent processes such as detector and SHG efficiency as well as transmission of the signal in the optical beam path.

For the radial BIC-resonant excitation, a five-fold SHG intensity enhancement is observed, confined to the top of the ring structure, illustrating the highly localized generation of the SHG signal. On the contrary, for off-resonant excitation a suppression of the SHG is observed within the same region. The suppression of the SHG excited spectrally apart from the radial BIC resonance can be attributed to strain introduced in the monolayer TMDC by the ring structure [104] which is overcome by the highly enhanced near fields for the resonant excitation. The wavelength dependency is a clear indication that the SHG enhancement is driven by the locally enhanced electromagnetic near field of the radial BIC resonances.

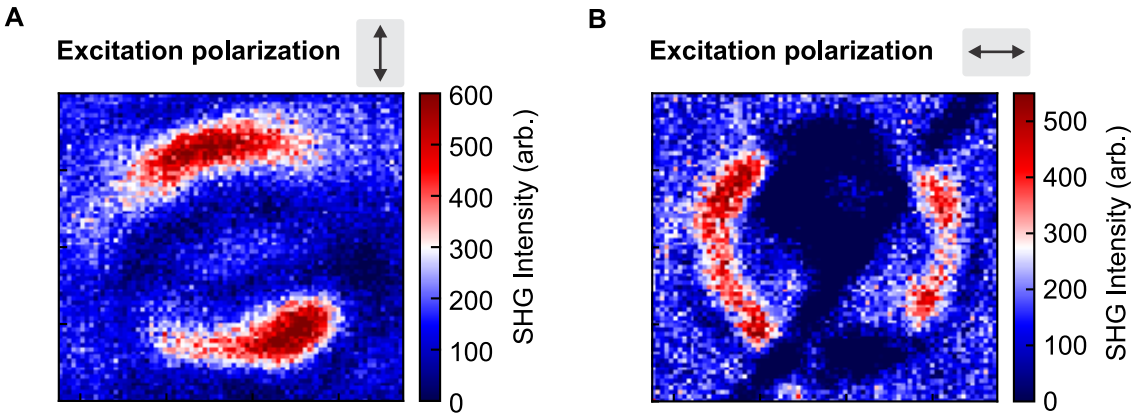

Figure 4.17.: Excitation polarization dependent SHG maps of the same ring covered with a monolayer of $MoSe_2$. (**A**) Background-corrected SHG map for vertical excitation polarization. (**B**) Background-corrected SHG map for horizontal excitation polarization.

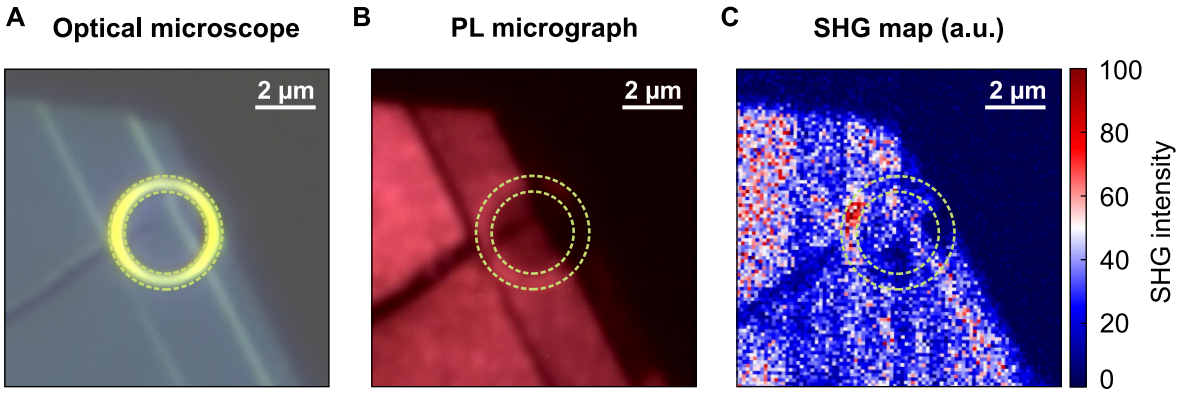

Figure 4.18.: SHG map of a symmetric ring covered with a monolayer of $MoSe_2$. (**A**),(**B**) Optical and photoluminescence micrograph of the radial BIC which is used for SHG reference maps for the purely symmetric structure. The outline of the ring is indicated as yellow dashed circles for clarity. (**C**) SHG map for the symmetric structure. Except for regions where the monolayer is folded, we observe no enhancement of the SHG signal present, supporting the BIC-induced SHG enhancement.

Another proof of the radial BIC related SHG enhancement is performed by using a linear polarizer for the excitation laser. As obvious from Fig. 4.3C, the maximum field enhancement across the ring is always parallel to the linear excitation polarization. As a result, rotating the angle of the incident linearly polarized light should lead to a rotation of the origin of the maximum SHG on the ring.
For this purpose, the system is illuminated with horizontal and vertical linear polarization in resonance with the radial BIC at 744 nm and the obtained SHG maps are depicted in Fig. 4.17, where the background was subtracted for easier comparison of both maps. Apparently, the SHG signal clearly follows the polarization of the incident laser beam and thus the maximum near-field enhancement of the radial BIC.

Furthermore, to clearly attribute the SHG enhancement effect to the radial BIC, another control experiment is performed. Here, a symmetric ring with $\Delta L = 0$ nm was covered with an $MoSe_2$ monolayer. The corresponding optical and photoluminescence (PL) image is shown in Fig. 4.18A and B. Already from the PL image, no enhancement is present which is confirmed by the SHG map in Fig. 4.18C.

Apart from the consistency checks with the coupled system, the emergence of the SHG signal from the resonator material silicon itself is excluded by measuring a pure uncovered radial BIC ring at the resonance wavelength. Although crystalline silicon does not exhibit a broken inversion symmetry, the devices are fabricated from amorphous silicon which could contribute to the observed SHG signal.
Nevertheless, only a negligible SHG signal is observed from the pure silicon ring itself as apparent from Fig. 4.19A. The comparison of the SHG from the pure ring and the coupled system in Fig. 4.19B shows that the SHG from the coupled system is two orders of magnitude larger, indicating that the SHG from the silicon can be neglected. As obvious from the previous measurements, the radial BIC is a versatile platform to boost the light-matter interaction between the $MoSe_2$ monolayer and the incident light.

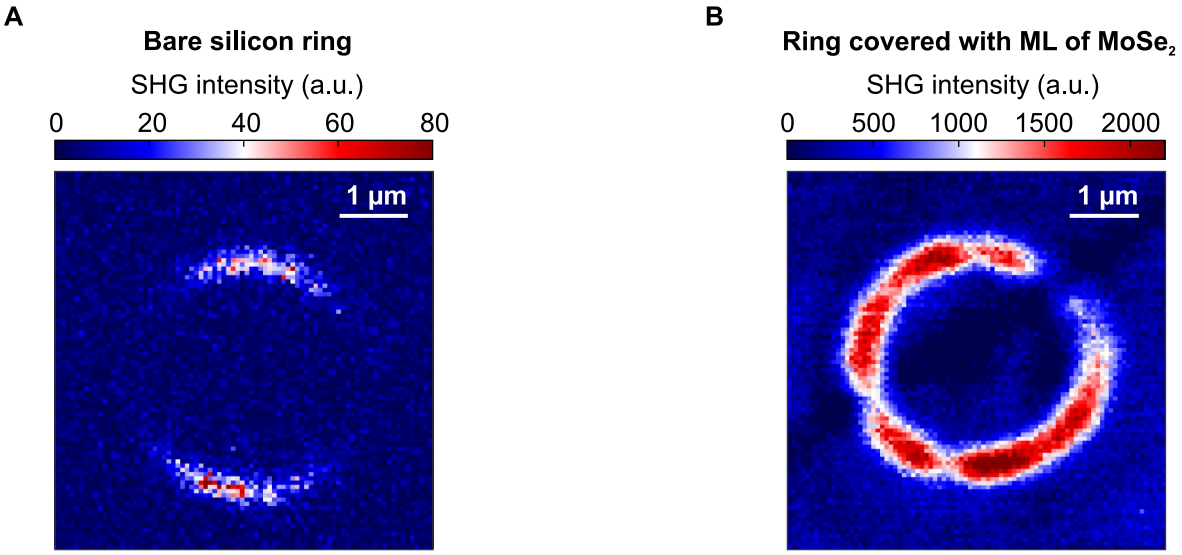

Figure 4.19.: SHG map comparison of a bare silicon radial BIC structure and a $MoSe_2$ covered ring. Comparison of SHG maps extracted from a bare asymmetric silicon radial BIC geometry in (**A**) and from the same ring covered with a monolayer of $MoSe_2$ in (**B**) plotted on different scales. For comparability of both maps, the background signal is set to zero. The maximum signal obtained from bare silicon structures is more than two orders of magnitude smaller on the whole ring compared to the $MoSe_2$ covered ring and can thus be neglected.

In summary, a new paradigm for BIC-based nanophotonics was introduced and experimentally demonstrated within this chapter: radial bound states in the continuum supported on rings of symmetry-broken all-dielectric resonators. Crucial for the implementation in optical circuits and as sensing devices, the challenging requirement for ultrasharp resonances and tiny footprints was achieved to obtain high quality factors in the visible along with the smallest footprints for symmetry-broken BIC metasurfaces reported in the literature. The novel BIC platform delivers polarization-invariant high-Q resonances with versatile spectral tunability in a footprint as low as 2 μm^2.

The concept shifts the boundaries of BIC-based nanophotonics and nanoscale sensors by reaching several milestones:
First, radially distributed and symmetry-protected modes were leveraged in semi-infinite ring structures to unlock a new design dimension for nanophotonic systems.
Second, the inherent polarization-invariance of the radial BIC enables straightforward nanophotonic integration and increased signal-to-noise ratios.
Third, it was experimentally shown that radial BICs offer drastically reduced spatial footprint while maintaining full control over resonance position and sharpness, reaching extremely high quality factors in the visible above 500.

Due to their highly enhanced near fields and precise spectral tunabilty, radial BICs are an ideal platform for tailoring and boosting light-matter interaction. The enhanced light-matter interaction was demonstrated with two applications: Increased biomolecular detection efficiency of streptavidin proteins and enhanced second harmonic generation in monolayers of $MoSe_2$.

All together, the radial BIC platform is ideally suited for enhanced light-matter interaction and can be employed to study light-matter coupling, potentially even in the strong coupling regime. Nevertheless, the platform can already be used for on-chip integration and could find applications for sensitive point-of-care devices in early disease detection and treatment but also for health monitoring. Beside the sensing aspect, the resonant system can be used for miniaturized on-chip light-sources based on the enhanced SHG of a suited material in the proximity.

5. Unlocking the out-of-plane dimension for photonic bound states in the continuum to achieve maximum optical chirality

The realization of lossless metasurfaces with true chirality crucially requires the fabrication of three-dimensional structures, constraining their feasibility for experiments and hampering practical implementations. Even though the three-dimensional assembly of metallic nanostructures has been demonstrated previously, the resulting plasmonic resonances suffer from high intrinsic and radiative losses. The concept of photonic bound states in the continuum (BICs) is instrumental for tailoring radiative losses in diverse geometries, especially when implemented using lossless dielectrics, but applications have so far been limited to planar and intrinsically achiral structures. In this chapter, a novel nanofabrication approach to unlock the height of generally flat all-dielectric metasurfaces is introduced as an accessible parameter for efficient resonance and functionality control. In particular, out-of-plane symmetry breaking in quasi-BIC metasurfaces is realized and the design degree of freedom is leveraged to demonstrate, for the first time, an optical all-dielectric quasi-BIC metasurface with maximum intrinsic chirality that responds selectively to light of a particular circular polarization depending on the structural handedness. The experimental results not only open a new paradigm for all-dielectric BICs and chiral nanophotonics but also promise advances in the realization of efficient generation of optical angular momentum, holographic metasurfaces, and parity-time symmetry-broken optical systems.

5.1. Height-driven linear qBICs

5.1.1. Analytical description and numerical simulation of height-driven qBICs

Controlling the interaction of different polarization states of light with matter has been a major goal of optics, covering the gamut from fundamental science [105] to practical technological applications [106]. Metasurfaces composed of resonant sub-wavelength building blocks with tailored optical properties have significantly advanced the capabilities for controlling light on the nanoscale [19], launching breakthrough applications in diverse fields including localized high-harmonic generation [91, 29], ultra-thin optical elements [78, 107], and biomolecular sensing [77, 27, 28]. In recent years, two major developments have underpinned the rapid progress in the metasurface technology and applications:
(i) a transition from traditional plasmonic resonator geometries to all-dielectric materials to overcome Ohmic losses, and
(ii) the utilization of the emerging physical concept of photonic quasi bound states in the continuum (qBICs), which provides versatile control over the radiative losses in nanophotonic systems [16, 15, 108, 80].
Combining these advances, all-dielectric qBIC-driven metasurfaces have delivered ultrasharp resonances with high values of the quality factors (Q factors) [91, 25], broad spectral tunability [27, 83], and strongly enhanced near fields for boosting both surface-driven and material-intrinsic processes [29, 31, 23]. Among different BIC-driven concepts [17], metasurfaces with broken in-plane inversion symmetry are especially appealing for tailoring light-matter coupling, because they enable a straightforward control over the radiative lifetimes via geometric perturbations within the metasurface unit cell (meta unit) [15].

So far, most qBIC-driven metasurface realizations have relied on modifying the in-plane geometry of the resonant elements to control the asymmetry, owing to the challenges of fabricating resonators with different heights at sub-wavelength distances. This limitation also constitutes a significant roadblock for applications such as holography [109, 110, 111], generation beams with an optical angular momentum (OAM) [112], chirality sensing [113], and chiral nanophotonics [114, 115, 116], which naturally require non-planar structures to enable the efficient interaction with more complex polarization states of light.

Here, out-of-plane symmetry-broken qBIC metasurfaces are experimentally demonstrated in the red part of the visible spectrum by leveraging a novel multi-step fabrication process for arbitrary height control of the resonators. Crucially, the approach implements different resonator heights based on an additional deposition step of the dielectric material, allowing height control with extreme precision down to the Angstrom range, only limited by the parameters of the respective evaporation or sputtering processes. This approach is utilized to realize height-driven qBIC resonances with tailored linewidths interacting with linearly polarized light.

The optical properties of qBIC metasurfaces can be modeled using coupled-mode theory (CMT) describing light scattering as an interference of a direct background channel and a resonant channel underpinned by a qBIC eigenstate excitation and re-radiation [73]. The eigenstate interaction with the far field is described by the coupling parameters m_e and for electromagnetic waves normally incident along the z-axis and polarized along unit vectors $\mathbf{e}$ they are proportional to (in analogy to eq. 2.25) [15]

$$m_e \propto \int_V \boldsymbol{J}(\boldsymbol{r}) \mathrm{e}^{ikz}, \tag{5.1}$$

where $\boldsymbol{J}(\boldsymbol{r})$ is the displacement current within the meta unit volume V and k is the light wavenumber. The coupling coefficients $m_e{}'$ to waves incident onto the metasurface backside are expressed by similar integrals with reversed propagation direction ($\mathrm{e}^{\mathrm{i}kz} \rightarrow \mathrm{e}^{-\mathrm{i}kz}$). The corresponding power transmission coefficients of an incident wave (polarized along unit vector $\boldsymbol{i}$) into an outgoing wave (polarized along unit vector $\boldsymbol{f}$) are expressed as

$$T_{\mathbf{fi}}(\omega) = |t_{\mathbf{fi}}(\omega)|^2, \quad \text{with} \quad t_{\mathbf{fi}}(\omega) = \tau\delta_{\mathbf{fi}} - \frac{m_{\mathbf{i}} m_{\mathbf{f}}{}'}{i(\omega - \omega_0) - \gamma_0{}'}, \tag{5.2}$$

where τ is a coefficient of background transmission preserving the polarization ($\delta_{\mathbf{fi}}$ is the Kronecker delta-symbol), and the complex eigenfrequency ($\omega_0 + i\gamma_0$) contains an imaginary part with radiative and dissipative contributions: $\gamma_0 = \gamma_\mathrm{r} + \gamma_\mathrm{d}$. QBICs with versatile polarization properties can be realized starting from a simple symmetry-protected anti-parallel electric dipole BIC of a double-rod meta unit as shown in Fig. 5.1A. The corresponding coupling parameters given by eq. 5.1 are reduced to

$$m_e \propto \boldsymbol{p}_1 \cdot \boldsymbol{e}\mathrm{e}^{ikz_1} + \boldsymbol{p}_2 \cdot \boldsymbol{e}\mathrm{e}^{ikz_2}, \tag{5.3}$$

where $\boldsymbol{p}_{1,2}$ are the electric dipole moments of the rods 1 and 2, and $z_{1,2}$ are their effective z-coordinates. Perfect BIC isolation with $m_e = 0$ for all polarization unit vectors $\boldsymbol{e}$ is achieved when $\boldsymbol{p}_1 = -\boldsymbol{p}_2$ and $z_1 = z_2$, *i.e.*, when identical rods are placed within the same plane.

An exemplary in-plane symmetry-breaking, transforming this BIC into a qBIC, occurs when the length of one rod is varied and the rod length difference ΔL becomes the asymmetry parameter (Fig. 5.1A). For $\Delta L > 0$, the electric dipole moments remain antiparallel, but have different magnitudes ($|\boldsymbol{p}_1| \neq |\boldsymbol{p}_2|$), which enables the coupling to waves linearly polarized along the long rod axis. Crucially, such coupling can also be tailored via the rod height difference Δh. In this case, both the magnitudes of the dipole moments and their effective locations become slightly different. Thus, the coupling to the far field is enabled by

$$m_y \propto \boldsymbol{p}_1(\mathrm{e}^{\mathrm{i}k\Delta z} - 1) + \Delta p, \tag{5.4}$$

where both $\Delta p = \boldsymbol{p_1} - \boldsymbol{p_2}$, and $\Delta z = z_1 - z_2$ are determined by Δh as it produces a difference in the rod volume and also shifts their centers of mass, see Fig. 5.1B.

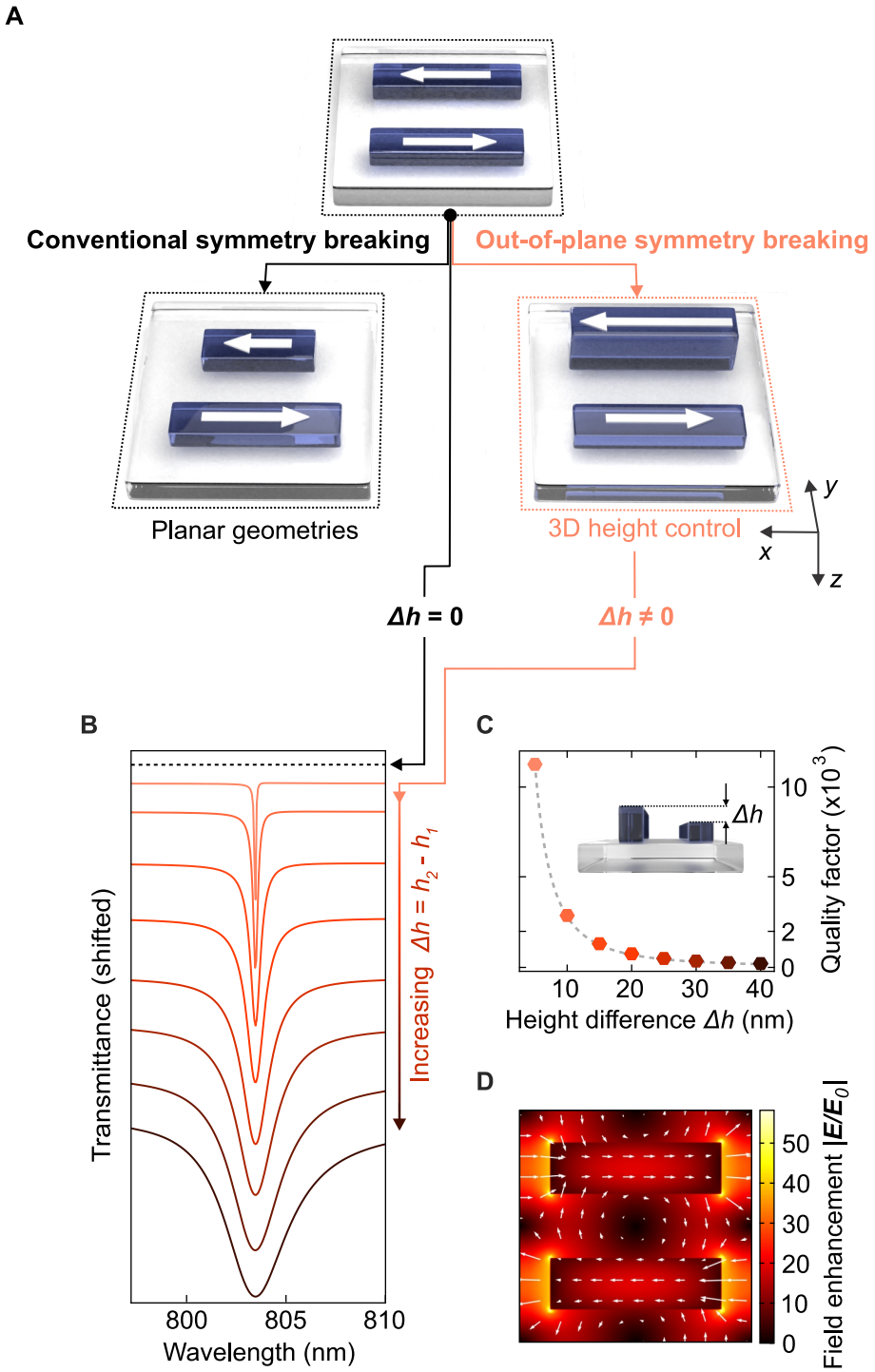

Figure 5.1.: Unlocking the height of dielectric resonators for photonic qBIC engineering. (**A**) Established qBIC geometries use in-plane symmetry breaking to couple otherwise dark BIC states to the radiation continuum. Here, out-of-plane symmetry-broken qBICs are introduced for high-Q optical metasurfaces. (**B**) Simulated spectral responses for various height differences starting from $\Delta h = 0$ nm (black dashed line, top) up to $\Delta h = 40$ nm (dark brown curve, bottom) with the corresponding electric near field in (**D**). The geometries of the structures were adjusted such that their resonance wavelengths coincide. (**C**) Corresponding Q factors extracted from the spectra in (**B**) following the inverse quadratic dependence (fitted as gray dashed line) typical for symmetry-broken qBIC metasurfaces.

In all above cases, the rods remain parallel and the qBIC is linearly polarized, contributing solely to T_{yy}. To verify the height-driven qBIC engineering, numerical simulations of the transmission and reflection of normally incident light are performed. For linearly polarized qBICs, a square metasurface lattice with a period of 450 nm is modeled, where the meta unit consists of parallel rods with equal footprint of 330×100 nm^2 and a base height of 120 nm with a variable height difference Δh (Fig. 5.1A).

Simulated transmittance spectra for linearly polarized light along the rod axis are shown in Fig. 5.1B, revealing strong and sharp qBIC resonances in the red part of the visible spectrum. In fact, the resonance linewidth and modulation are directly controlled by the asymmetry parameter Δh. As expected for BIC-driven systems, the resonance is absent for the symmetric case ($\Delta h = 0$ nm, black dashed line in Fig. 5.1B) and starts to couple to the radiation continuum for increasing asymmetry, showing the sharpest resonances with Q factors above 10^4 for $\Delta h = 5$ nm.

To quantify the influence of the asymmetry parameter on the resonance sharpness, the Q factors are extracted from the transmittance spectra by fitting them with a coupled mode theory (CMT) model and plotting them as a function of Δh (Fig. 5.1C). Apparently, the Q factors follow an inverse quadratic relationship with the asymmetry ($Q \propto 1/\Delta h^2$), which is a hallmark feature of qBIC metasurfaces, confirming that the height-driven symmetry breaking fits well within the established BIC framework.

As a further confirmation, the electric near-field distribution is simulated at the resonance wavelength (Fig. 5.1D). The characteristic mode structure of anti-parallel dipoles is nicely reproduced in the numerical simulations, and near-field enhancements $|\boldsymbol{E}/\boldsymbol{E_0}|$ exceeding 50 are observed, which is competitive with previous symmetry-breaking approaches [27]. Notably, the Angstrom-level control over the asymmetry provided by state-of-the-art material deposition technologies such as atomic layer deposition (ALD) can enable ultra-small values of Δh and therefore much higher field enhancements (Fig. 5.2). The large field enhancement and the strong confinement of the fields to the resonator surface (Fig. 5.1D) render height-driven geometries ideal candidates for enhancing interface-driven processes such as biospectroscopy or catalysis.

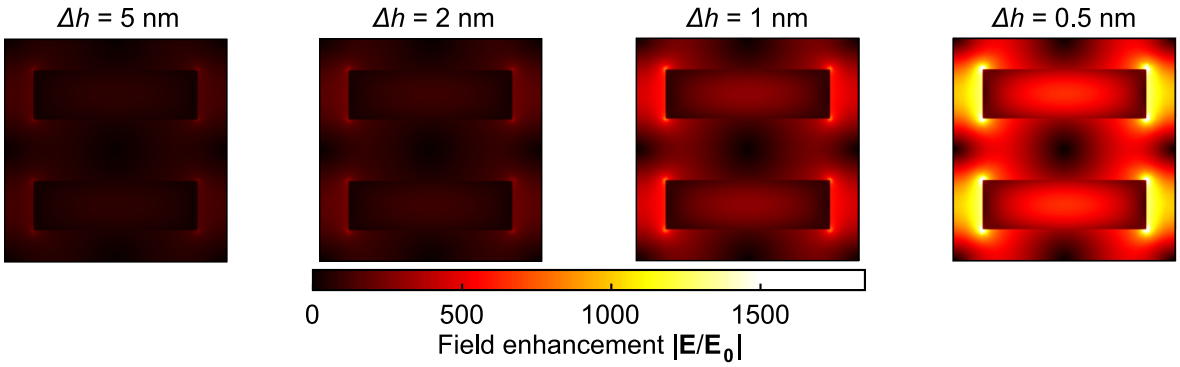

Figure 5.2.: Angstrom-level control for high field enhancements. Numerical investigation of the electric near fields associated with the height-driven qBIC resonances for various small height differences. The field enhancement increases drastically towards Angstrom-scale height differences, such as 5 Å on the right-hand side with enhancement factors of up to 2000.

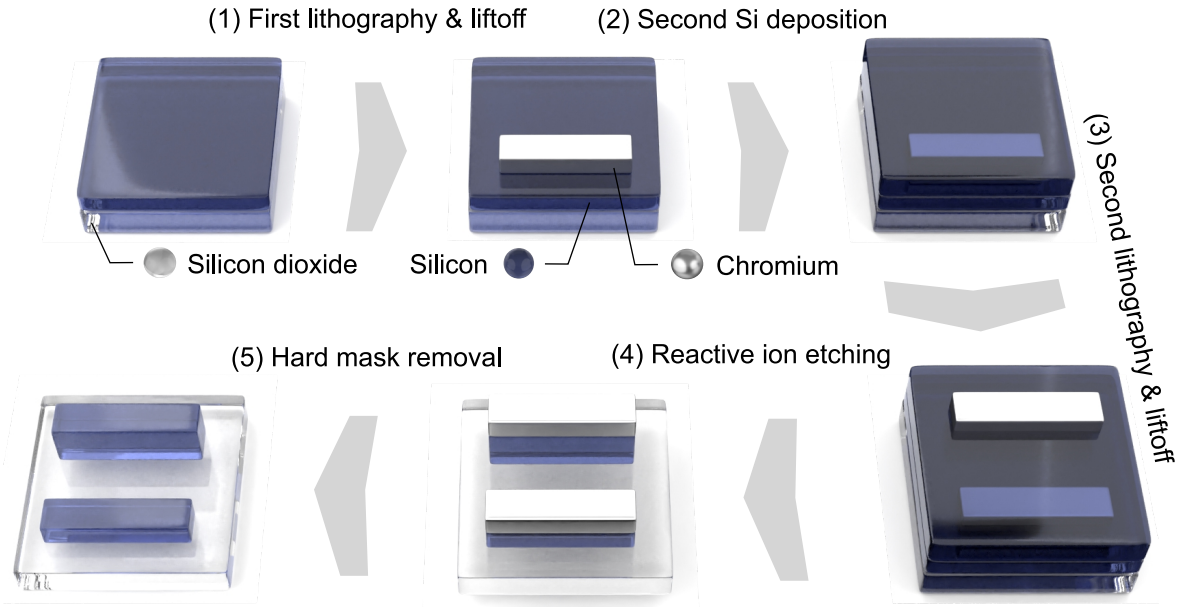

Figure 5.3.: Fabrication principle of all-dielectric metasurfaces with full height control. The fabrication is composed of a two-step EBL process (step 1 and 3) with an additional silicon deposition step in between (step 2). Reactive ion etching (step 4) and chemical wet etching (step 5) transfer the hard mask pattern into the silicon and reveal the pure silicon structures.

5.1.2. Experimental demonstration of out-of-plane symmetry breaking

For the realization of all-dielectric multi-height metasurfaces, a new multi-step nanofabrication approach is developed. The core mechanism of this method leverages the combination of an N-step electron beam lithography process and an N-step deposition process to obtain a metasurface with N different height levels. The fabrication steps are illustrated in Fig. 5.3 for $N = 2$, as required for the two-level height-driven target geometries introduced in Fig. 5.1. Detailed process parameters are given in the Methodology. Importantly, the method is fully scalable for large N, since additional lithography/deposition steps can be added at any point during sample fabrication to obtain additional height levels.

In essence, the metasurface fabrication starts with the plasma-enhanced chemical vapor deposition (PECVD) of an amorphous silicon (a-Si) layer onto a silicon dioxide (SiO_2) substrate, where the thickness h_1 defines the height of the lowest resonator element with the smallest thickness in the meta unit (Fig. 5.3, left). Electron-beam lithography, metal deposition, and wet-chemical lift-off are then performed to obtain a thin chromium (Cr) hard mask defining the footprint of the first resonator (Fig. 5.3, step (1)). Subsequently, a second layer of a-Si is deposited onto the sample with a precisely controlled thickness Δh, which produces a total thickness of $h_2 = h_1 + \Delta h$ for the second resonator element (Fig. 5.3, step (2)). A second hard-masking step with accurate spatial alignment is then performed to define the footprint of the second resonator (Fig. 5.3, step (3)). At this point, additional pairs of a-Si and hard-masking could

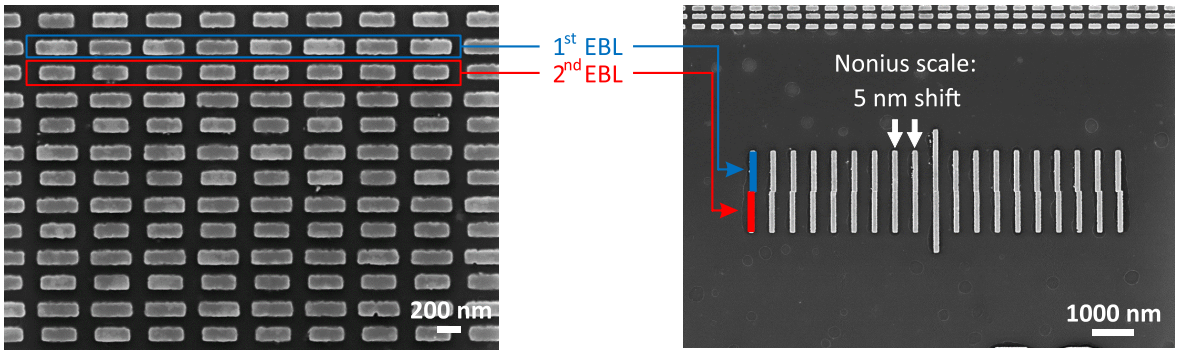

Figure 5.4.: SEM micrographs for a two-step lithography process. SEM micrograph of a planar BIC metasurface fabricated with two-step electron beam lithography process on the left-hand side. The nonius scale on the right-hand side shows an alignment accuracy of 5 nm.

be performed to increase the metasurface height levels. Finally, reactive ion etching is used to transfer the resonator patterns into the a-Si layers (5.3, step (4)), resulting in pure silicon structures with different height levels after wet-chemical removal of the Cr hard masks (Fig. 5.3, step (5)).

The successful fabrication of the multi-height metasurface structures is confirmed by atomic force microscopy (AFM) and scanning electron microscopy (SEM). The as-designed metasurface pattern and height differences (Fig. 5.6A) are already evident from the different scattering intensities in the SEM micrograph in Fig. 5.6B. The SEM image further confirms the good spatial alignment between the lithography steps associated with the two resonator heights (dashed boxes in Fig. 5.6B) although numerical simulations only show a small impact of the relative rod alignment (Fig. 5.5) for an alignment accuracy of 5 nm (see Fig. 5.4). The AFM measurements reveal accurately defined height differences between adjacent resonators for three different height-driven metasurfaces with asymmetries of 10 nm, 20 nm, and 40 nm (Fig. 5.6C).
The asymmetry-dependent optical response of the metasurfaces is characterized using

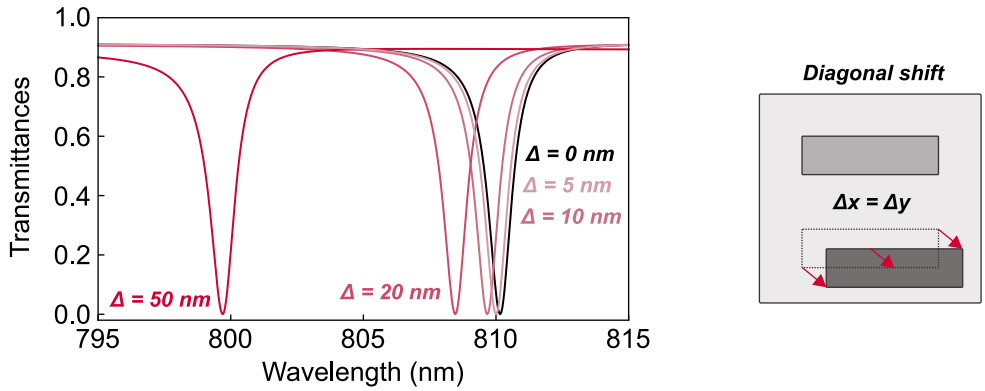

Figure 5.5.: Numerical investigation of resonator shifts in the unit cell. Simulated transmittance spectra for different diagonal shifts Δ of one resonator within the unit cell. For the placement accuracies in this work ($\Delta \leq 5$ nm), the impact on the spectral response is negligible.

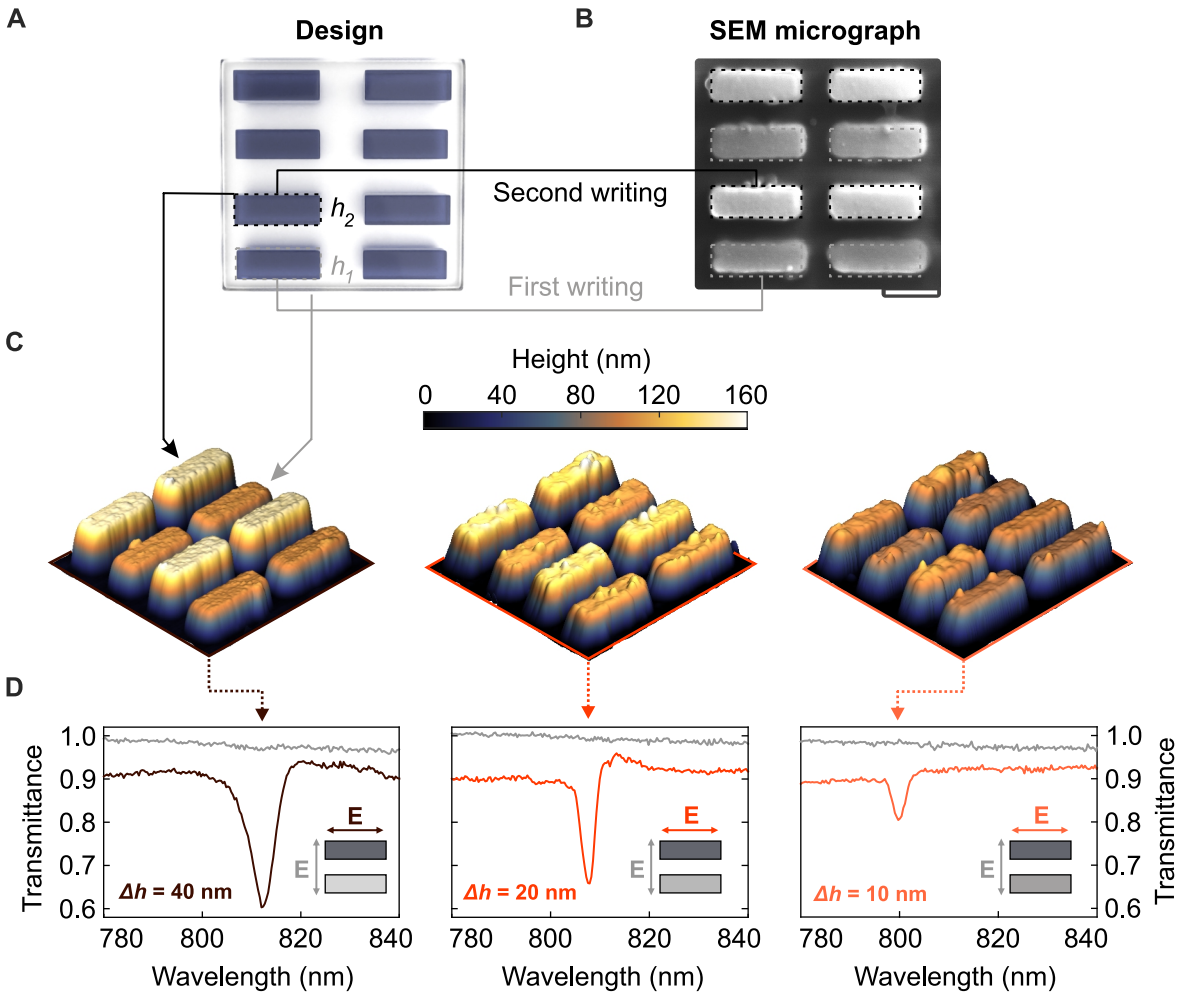

Figure 5.6.: Experimental characterization of height-driven linear qBICs. (**A**) Design of the metasurface with the scanning electron micrograph in (**B**), showing different height levels from the scattering contrast. (**C**) AFM images for Δh = 40 nm (left), Δh = 20 nm (middle), and Δh = 10 nm (right) height difference, showing the precise control over the asymmetry via the layer height. (**D**) Corresponding transmittance spectra demonstrate increasing Q factors and decreasing coupling to the far-field for smaller asymmetries.

confocal white light transmission microscopy (Fig. 5.6D). In excellent agreement with the simulations, pronounced qBIC resonances are observed when the incident light is polarized along the long rod axis, whereas the resonances disappear for the orthogonal polarization in accordance with the BIC mechanism. Comparing the height-driven metasurface samples for different values of Δh, an increase of the resonance Q factor is found for decreasing asymmetry, highlighting the resonance tailoring capabilities of the method.

The experimental results show that the fabrication approach provides a toolkit for realizing multi-element metasurfaces with tailored heights only limited by the precision of the utilized deposition tool, enabling previously unavailable Angstrom-level control over the asymmetry in height-driven BIC geometries.

5.2. Chirality in nanophotonics

Chirality lies at the heart of nature and is present in a variety of systems, such as life-important sugars, the human DNA, and in many pharmaceuticals. As such, a chiral entity, also called *enantiomorph* or *enantiomer* is not superimposable with its mirror image through any rotational or translational transformation (see Fig. 5.7). Nevertheless, two enantiomers of the same species can have fundamentally different functionalities regarding the target drug effect for pharmaceuticals or the interaction with light. Differentiating the chirality of different species or molecules is thus ultimately important and of high interest in the pharmaceutical but also many other disciplines.

Similar to molecules or plants, light also exhibits chirality via its optical circular polarization. Depending on the polarization of the light and the handedness of a specimen, the interaction of light, *i.e.*, the absorption of a certain light polarization, with that specimen is highly different. This principle is utilized to determine the chirality of chiral molecules.

Unfortunately, the interaction between light and the molecules is very weak, limiting the chirality determination to large amounts of specimen. One way to overcome the inefficient detection is the utilization of nanostructures with optical resonances tailored to the specific molecular response. By arranging the nanostructures with a certain chirality, they will selectively respond to one circular polarization and convert the far-field energy into highly enhanced electromagnetic near fields. As a consequence, the absorption of chiral molecules, that are located within these enhanced near fields and exhibit the appropriate chirality, is highly boosted.

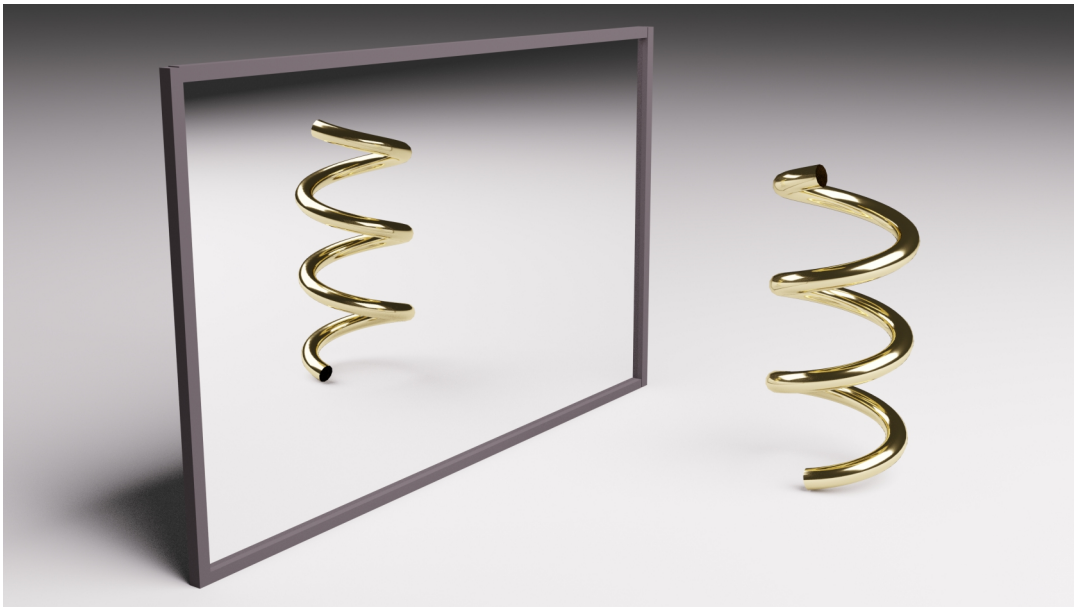

Figure 5.7.: Exemplary chiral structure. A three-dimensional helix with its mirror image as representative for a chiral nanophotonic structure.

So far, a major roadblock for chiral nanophotonics is a fundamental trade-off between either using metallic nanostructures or all-dielectric resonators. Although metal-based systems offer a maximally chiral three-dimensional arrangement due to the well-established bottom up fabrication and stacking approaches, they suffer from high material-intrinsic losses. Likewise, all-dielectric systems provide manageable radiative losses but are limited to planar and thus intrinsically achiral structures owing to the more complicated top down fabrication techniques, which they require.

In the following section, a novel approach for chiral nanophotonics is introduced by implementing a unique concept for all-dielectric resonator systems via the combination of symmetry-broken quasi bound states in the continuum (qBICs) to precisely tailor the radiative Q factor of the metasurface and a novel fabrication approach providing full height control over individual metasurface elements to unlock an additional degree of freedom.

5.3. Chiral qBIC metasurfaces

5.3.1. Description and implementation of chiral qBICs

Chiral qBICs have recently been proposed theoretically [116, 117, 118], aiming to provide efficient coupling with circularly polarized light and circular dichroism responses with greatly reduced linewidths. However, proof-of-concept experimental implementations remain limited to the microwave range [119], while optical realizations faced severe restrictions associated with complex three-dimensional unit-cell designs [115, 119, 120].

Here, the out-of-plane symmetry breaking approach is generalized to demonstrate chiral qBIC metasurfaces that selectively couple to circularly polarized light depending on the structural handedness. Beneficially, the results and fabrication method relax the constraints of purely planar metasurface geometries, and thus offer a nontrivial generalization to the entire metasurface concept. This approach unlocks an additional degree of freedom and establishes independent parameters for freely tuning the optical response of metasurfaces. In this way, their design flexibility is significantly increased, delivering previously unavailable functionalities via multi-height geometries.

By combining the height-driven out-of-plane symmetry breaking perturbation with a conventional in-plane one, the realization of chiral qBIC metasurfaces [117, 119] is enabled. Specifically, a metasurface is implemented that breaks all point symmetries by utilizing a meta unit composed of two rods of equal lengths diverged in-plane by a small angle θ. Furthermore, the rods have different footprints and heights while maintaining identical cross sections (Fig. 5.8A). In this case, the electric dipoles $\boldsymbol{p_1}$ and $\boldsymbol{p_2}$, even though equal in magnitude ($|\boldsymbol{p}_1| = |\boldsymbol{p}_2|$), are not exactly anti-parallel, and their effective z-coordinates also differ, producing a three-dimensional chiral arrangement. It is insightful to evaluate eq. 5.3 in such a case and obtain for the coupling parameters to the left circularly polarized (LCP) and right circularly polarized (RCP) waves

$$m_{L,R} \propto \sin(\theta \pm k\Delta z/2). \tag{5.5}$$

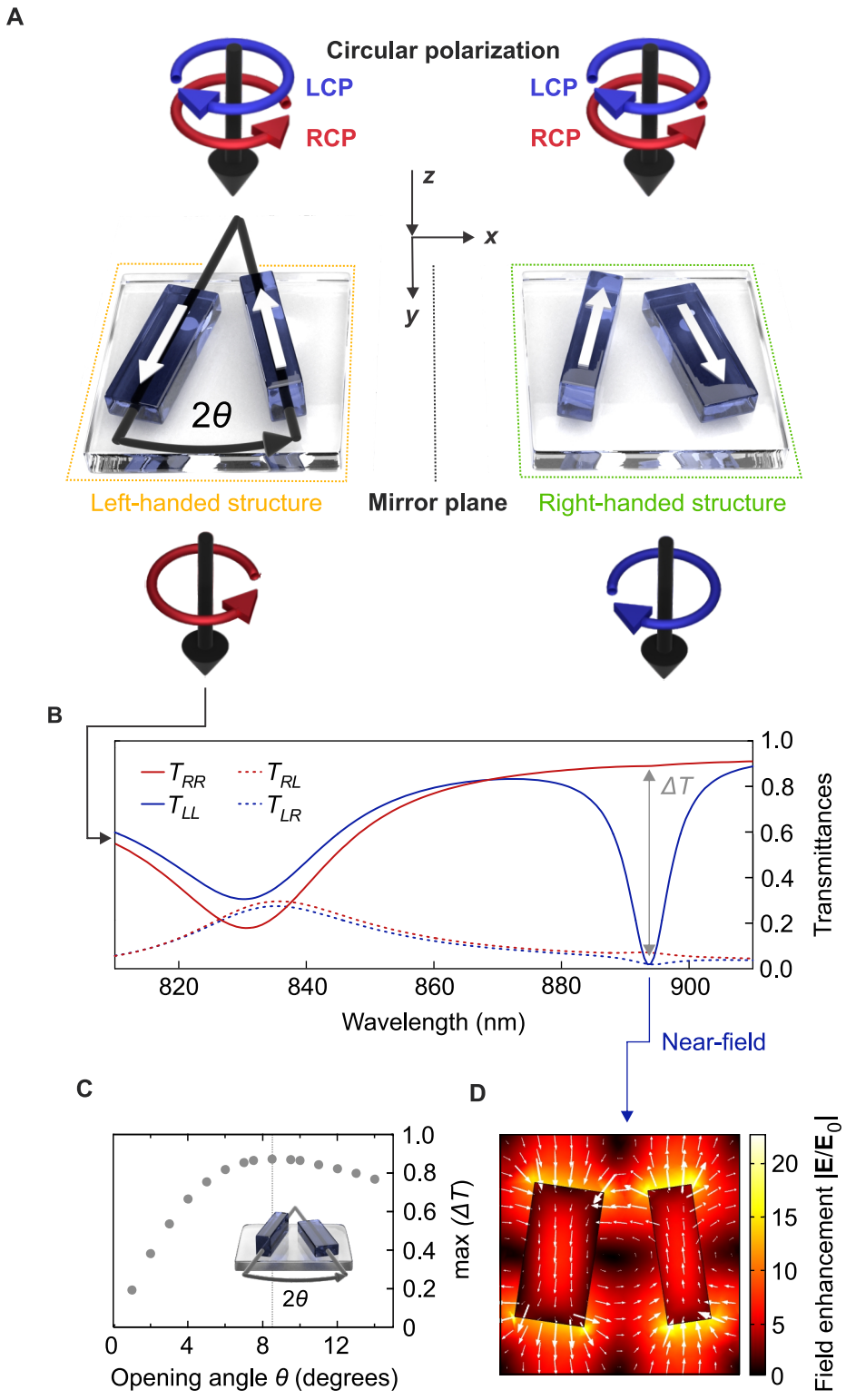

Figure 5.8.: Tailoring the height-driven qBIC by an opening angle θ for maximum chirality. (**A**) Schematic illustration of the chiral measurements. Left-handed (left, yellow) and right-handed structures (right, green) are illuminated with LCP and RCP light and respond selectively to light with appropriate helicity. (**B**) Simulated transmittance spectrum for a left-handed enantiomer, showing the excitation of a qBIC resonance only for LCP light with the corresponding near field in (**D**). (**C**) Tailoring the opening angle θ allows to achieve maximum chirality for $\theta = 8.5°$.

Precise tailoring of the meta unit geometry is used to balance the perturbations via $2\theta = k\Delta z$. Thereby, efficient and controllable qBIC coupling to the LCP waves is enabled with $m_L \propto \sin(2\theta)$, whereas sustaining full qBIC isolation from the RCP waves by $m_R = 0$. Notably, according to eq. 5.2, an ideally matched chiral metasurface does not convert circular polarizations from LCP to RCP ($t_{RL} = 0$) or from RCP to LCP ($t_{LR} = 0$). Although there are no symmetry restrictions which prohibit such conversions in the presence of rotational symmetry axes [121], the polarization conversion is absent.

Remarkably, this simple design allows approaching the ultimate limit of maximum chirality [122], when an object remains transparent to the waves of one circular polarization, for instance RCP, and strongly interacts with those of the opposite polarization (LCP). To realize this condition, one has to first ensure that the qBIC resonance occurs in the spectral range of full background transparency ($|\tau| \approx 1$) and negligible dissipation in the metasurface material ($\gamma_0 = \gamma_r$). Then, the coupling coefficients to LCP light incident onto the metasurface front and back satisfy $m_{L'} = -m_L{}^*$. The decay rate γ_r follows a characteristic quadratic dependence on the coupling parameter $\gamma_r = |m_L|^2$ leading to zero transmittance t_{LL} at resonance [119] (given by eq. 5.2).

Importantly, the maximum chiral metasurfaces qualitatively outperform those exhibiting bands of similarly strong circular dichroism (CD), such as plasmonic chiral hole arrays [123]. For the latter, the CD reaches its extreme ±1 values when one circular polarization is fully blocked regardless of the transmission of the opposite one. Strong CD of maximum chiral qBIC metasurfaces, on the contrary, is achieved when a selective blocking of waves of one circular polarization is accompanied by close to unitary transmission of their counterparts. As a specific parameter quantifying such exceptional transmission selectivity, the transmittance difference is introduced as

$$\Delta T = T_{RR} - T_{LL} \tag{5.6}$$

to specifically characterize the proximity to maximum chirality: while the conventional CD $= (T_{RR} - T_{LL})/(T_{RR} + T_{LL})$ tends to ±1 as soon as waves of a certain circular polarization are fully blocked, the difference ΔT approaches ±1 only if, additionally, the waves of the opposite polarization are fully transmitted.

Left-handed and right-handed enantiomers of the chiral qBIC metasurface can be realized by swapping the rods (Fig. 5.8A). The opposite enantiomer similarly remains transparent to LCP waves and resonantly blocks RCP waves. In contrast to metasurfaces with rotational symmetry axes [124, 125], the blocked circularly polarized light is not absorbed but is rather reflected backwards [117] as illustrated in Fig. 5.9. Therefore, under perfect circumstances, each metasurface enantiomer acts as a maximum chiral lossless filter of the corresponding handedness.

To confirm the analytical description, the chiral configurations are simulated by utilizing a meta unit consisting of a pair of rectangular rods diverged by a small angle θ from the y-axis (Fig. 5.8A). The square lattice period is set to 550 nm and the rod centers are placed equidistantly with a 275 nm spacing between them. To preserve the equality of the electric dipole moment magnitudes ($|\boldsymbol{p_1}| = |\boldsymbol{p_2}|$), an identical 160 x 100 nm^2 cross section of both rods is maintained and their lengths are kept equal to $L = 310$ nm.

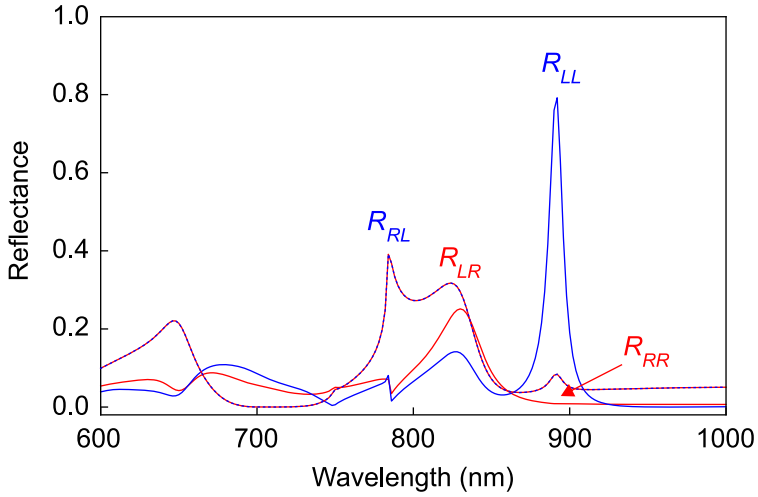

Figure 5.9.: Numerical simulation of the reflectance spectrum. Co- and cross-polarization terms for a left-handed chiral qBIC metasurface with an opening angle of $\theta = 8.5°$ showing the selective reflection of of LCP light.

The asymmetry is introduced by turning one rod over to its side, as shown in Fig. 5.8A. For the resulting $\Delta h = 60$ nm, one can roughly estimate the relative displacement of the dipole moments along the z-axis by $\Delta z \approx 30$ nm. Then, for the resonant wavelength around 900 nm, the proportionality $2\theta = k\Delta z$ is fulfilled for a diverging angle $\theta \approx 6°$. For a more precise determination, a series of numerical simulations for different θ is performed and it is found that $\theta = 8.5°$ corresponds to the optimal transmission of circularly polarized waves shown in Fig. 5.8B. As illustrated in Fig. 5.8**C** , smaller angles produce weaker chirality, while larger ones also suppress the maximum values of ΔT (for experimental data see Fig. 5.12).

In the optimal chiral configuration, as envisioned by the CMT approach, the qBIC is fully decoupled from the normally incident RCP waves but gives rise to a pronounced transmission resonance for the LCP waves at a wavelength of 892 nm. The corresponding near-field pattern under LCP illumination (Fig. 5.8D) demonstrates a maximum enhancement of the local fields by a factor of more than 20.

5.3.2. Optical characterization of chiral qBICs

Using the multi-step fabrication approach, left-handed, right-handed, and achiral qBIC samples are realized at a design wavelength of 900 nm approaching the visible wavelength range (Fig. 5.10 and Fig. 5.11). The AFM images (Fig. 5.10A, B and Fig. 5.11A) highlight the excellent experimental reproduction of the designs with clearly defined structure sizes and height differences. The optical response of the metasurfaces is retrieved using a custom-built transmission microscopy setup (see Fig. 3.13) incorporating the necessary polarizers and quarter wave plates to generate circularly polarized light. Notably, two beam paths for RCP and LCP light are implemented, enabling the convenient switching between left-handed and right-handed illumination

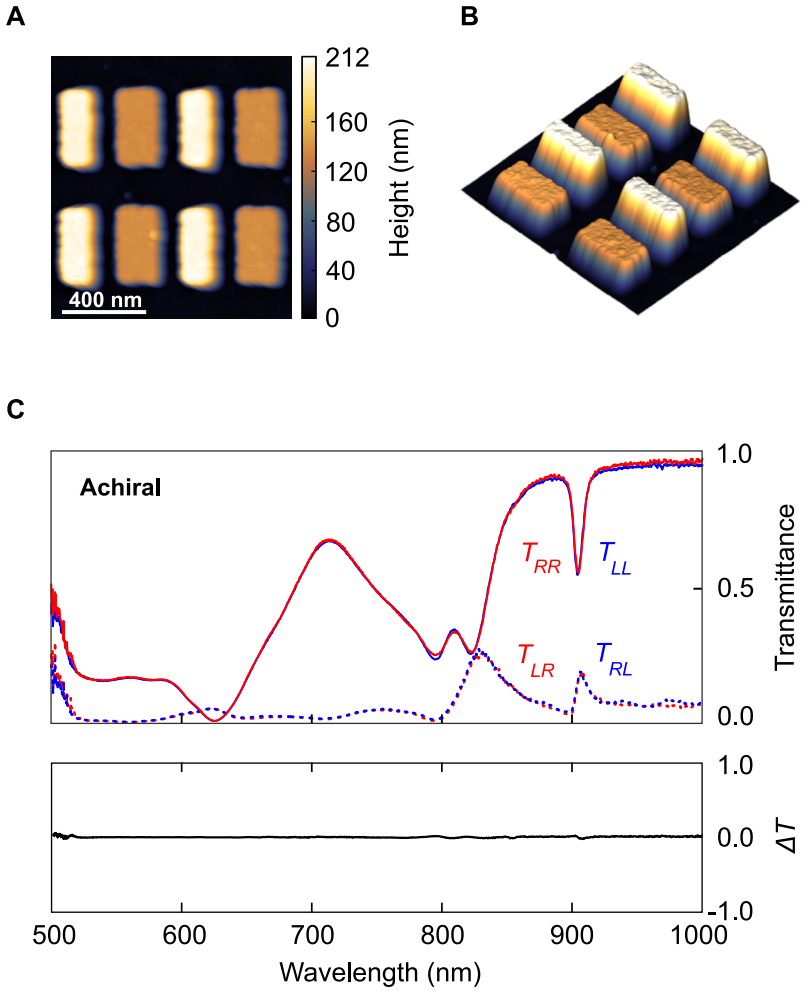

Figure 5.10.: Optical characterization of the achiral structure. (**A**) AFM image for the achiral structure showing a good spatial alignment of the individual resonators and a height difference of $\Delta h = 60$ nm. (**B**) 3D AFM micrograph of the same area. (**C**) The optical characterization with chiral analyzers shows the same coupling and transmittance (T_{LL}, T_{RR}) for LCP and RCP light leading to a vanishing ΔT signal in the lower panel. The polarization conversion (T_{LR}, T_{RL}) is small as apparent from the dashed blue and red curves in the top panel of (**C**).

during experiments. Light is condensed on the sample using a 10x objective and collected through an analyzer using a 60x objective to enable the targeted polarization resolved interrogation of individual metasurface patterns with sizes of 40 by 40 µm^2. A spectrometer is used for spectral analysis in order to resolve the sharp features of the chiral qBIC resonances.

Focusing first on the achiral structures as depicted in Fig. 5.10, nearly identical transmittance spectra are observed for RCP and LCP illumination, leading to a vanishing ΔT signal (Fig. 5.10C) throughout a large spectral range from 500 nm to 1000 nm. The spectral features at 900 nm in both the RCP and LCP spectra are attributed to a height-driven BIC.

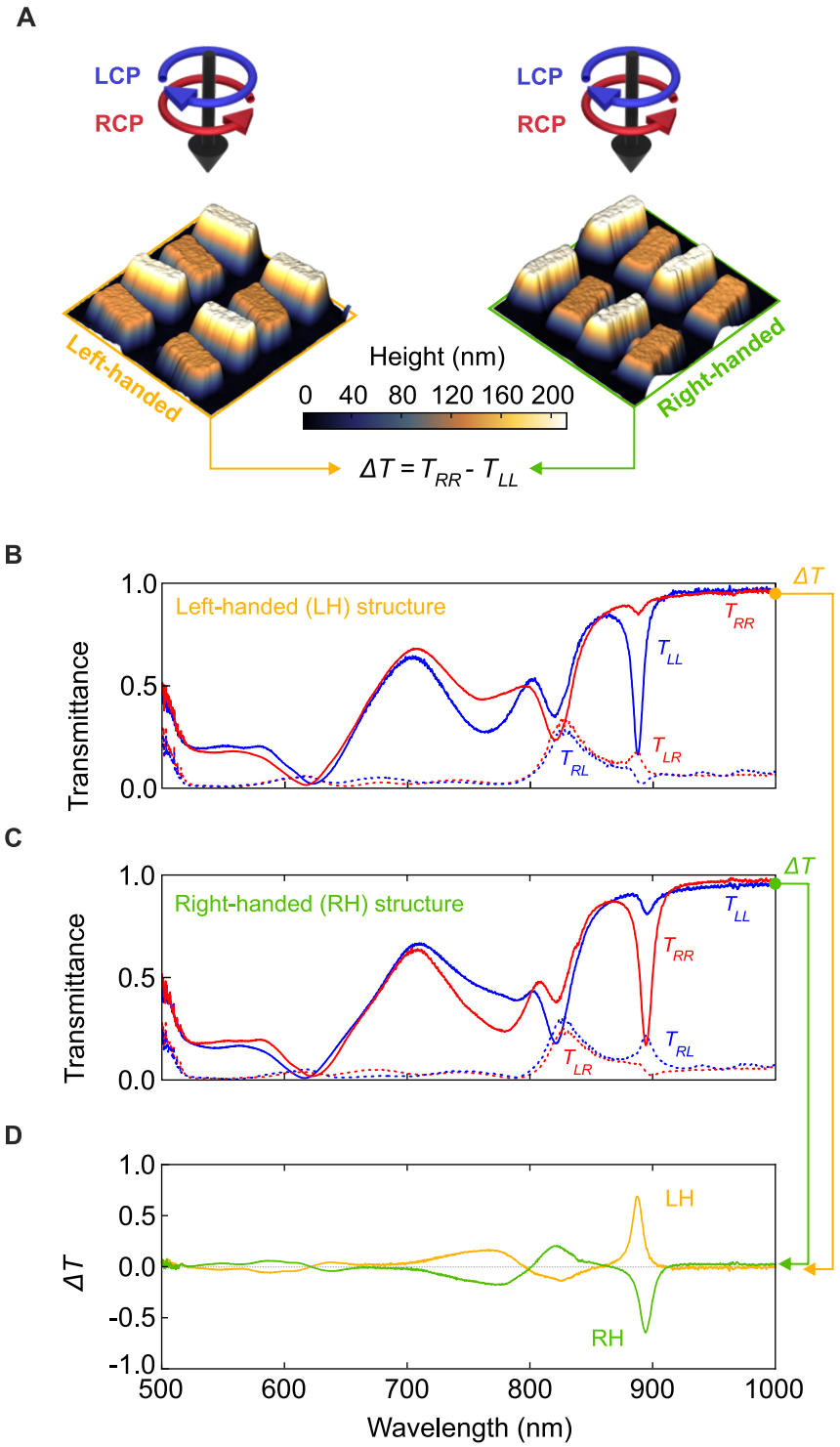

Figure 5.11.: Optical characterization of the left- and right-handed enantiomer. (**A**) AFM micrographs of the left-handed (left, yellow) and right-handed (right, green) enantiomer tuned to the maximum chiral regime with $\Delta h = 60$ nm and $\theta = 8.5°$. Both structures are illuminated with LCP and RCP light and their transmittance differences ΔT are recorded. The optical spectra in (**B**) and (**C**) show selective coupling to LCP and RCP light depending on their handedness with almost no polarization conversion. (**D**) The corresponding chiral spectra show almost perfect mirror images.

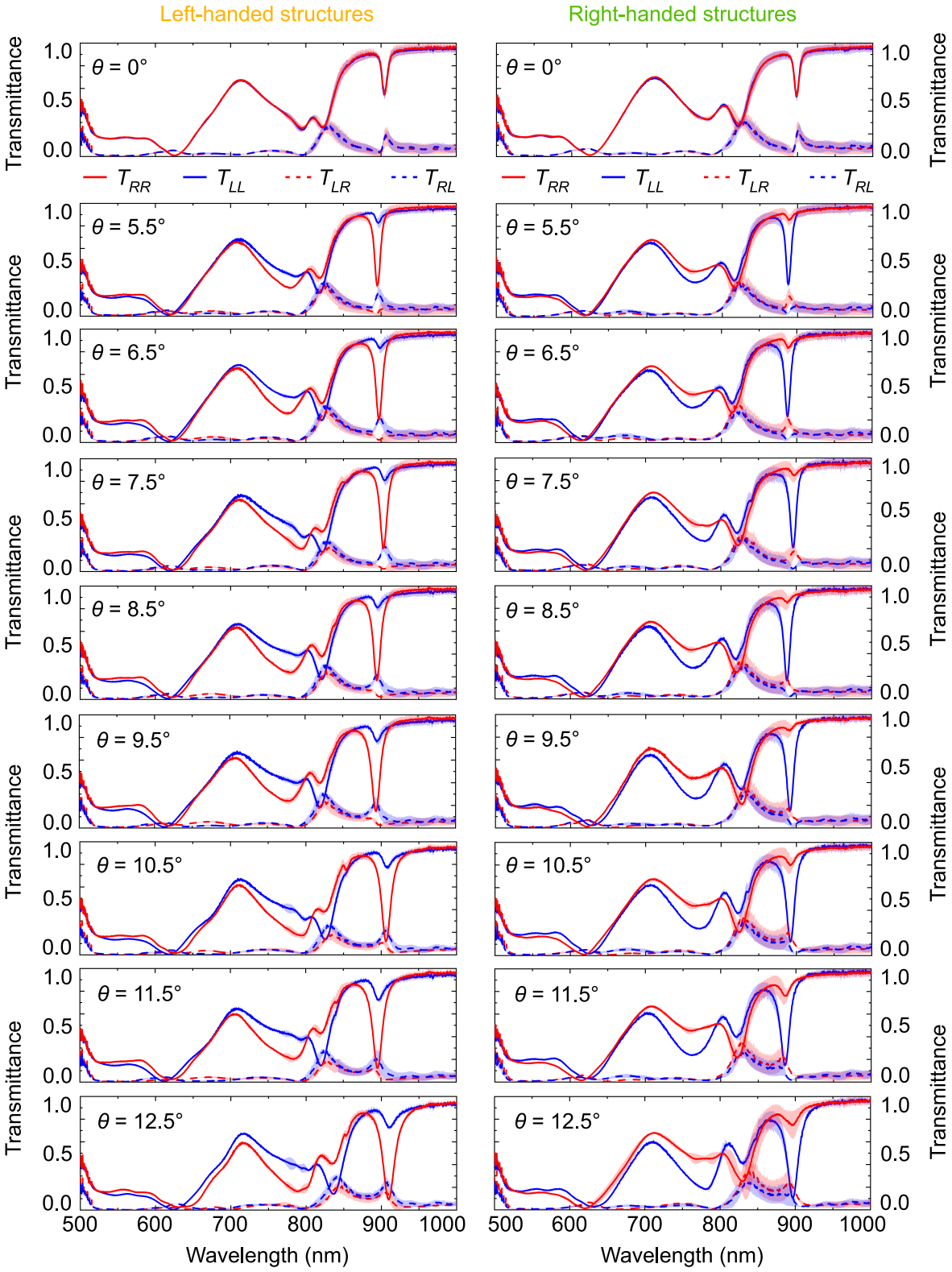

Figure 5.12.: Co- and cross-polarized transmittances for different diverging angles θ. Measured co- and cross-polarized transmittances for a left-handed (left side) and right-handed structure (right-hand side) from $\theta = 0°$ to $\theta = 12.5°$.

As apparent from Fig. 5.11B, the chiral left-handed geometry shows a markedly different optical response, with a pronounced transmission dip at the design wavelength of 900 nm for LCP, which is almost completely absent for RCP illumination in line with the numerical predictions (Fig. 5.8). This distinct chiral selective behavior results in a large modulation of the ΔT signal with $\Delta T = 0.7$ and a narrow bandwidth with a quality factor of $Q \approx 80$, which is the highest experimental value for a strongly chiral optical resonance reported in the literature so far.

For the chiral right-handed structure in Fig. 5.11C, the situation is reversed, with a strong resonance feature for RCP light and a vanishing optical response for LCP, resulting in a ΔT value with equally large magnitude but opposite sign at $\Delta T = -0.7$, and a similarly high Q factor as obvious from Fig. 5.14A and Fig. 5.14B. Most importantly, the cross-polarization measurements in Fig. 5.11C show no significant polarization conversion as expected from eq. 5.2 and the numerical predictions (Fig. 5.8B).

The experimental polarized transmittance spectra undoubtedly identify the observed resonance at a wavelength of around 900 nm as a chiral qBIC closely tuned to the maximum chiral regime, with the transmittance difference reaching $\Delta T = \pm 0.7$. Thus, for the right-handed (left-handed) enantiomer, the co-polarized LCP (RCP) transmittance stays close to 0.9, while the co-polarized RCP (LCP) transmittance resonantly drops down to below 0.2, whereas both cross-polarized transmittances remain below 0.1 within the whole range of this resonance.

Significantly, the comparison between the optical transmittance spectra and the numerically obtained chiral response shows excellent agreement (Fig. 5.15). The good agreement can be attributed to the precise adjustment of the simulation parameters to the experimental situation. For instance, the in-house measured ellipsometry data of the deposited a-Si film (see Fig. 3.3) were utilized and the size were adjusted according to the AFM (Fig. 5.11A) and SEM images.

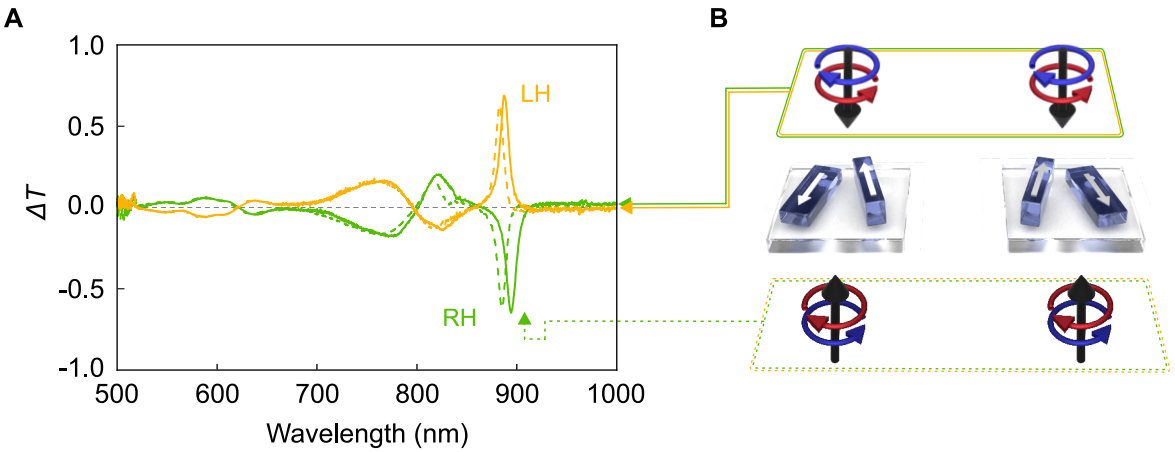

Figure 5.13.: Lorentz reciprocity. (**A**) Chiral signals from the left-handed (LH, yellow) and right-handed (RH, green) enantiomer for forward and backward illumination as indicated in (**B**) showing almost no differences and thus conserving Lorentz reciprocity.

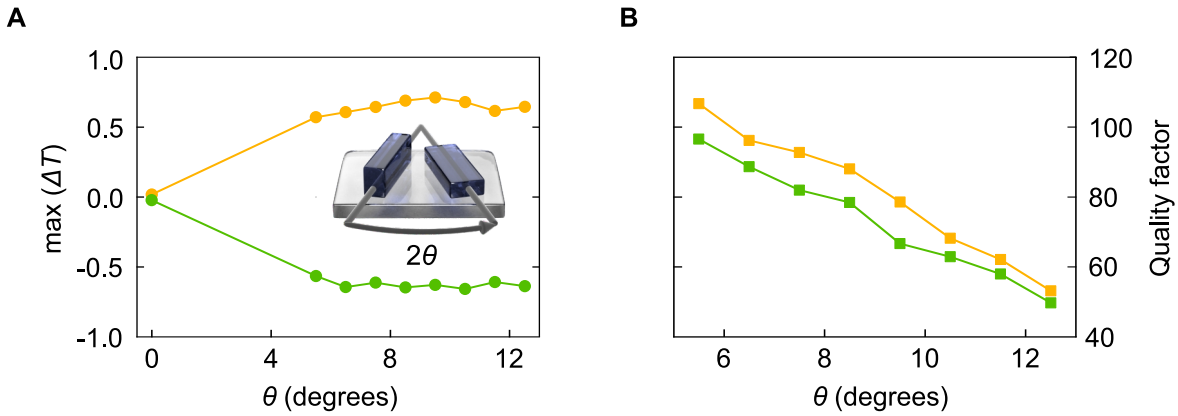

Figure 5.14.: Experimental tuning of the chirality. (**A**) The maximum chirality increases for higher opening angles θ until it peaks and saturates around $\theta = 8.5°$. (**B**) The extracted Q factors decrease towards higher opening angles, providing independent tailoring of the chirality and Q factor.

Furthermore, to estimate the accuracy of optical experiments, the consequences of Lorentz reciprocity are checked by performing the identical measurements on the chiral metasurface flipped upside down. Since the spectral responses remain unchanged (see Fig. 5.13), sufficient precision of the optical setup is guaranteed. In addition to that, the sample quality and alignment of the setup is checked by measuring the sample with four different rotation angles. As apparent from Fig. 5.16, the spectra are almost identical. Slight variations in the signal are addressed to a small degree of elliptical polarization.

Additionally, the chiral qBIC retains the versatile resonance tuning capabilities of the BIC concept, which is demonstrated by experimentally varying the orientation angle θ between the two rods. Obviously, the modulation of the ΔT signal (Fig. 5.14A) is mostly constant while the Q factor of the resonance (Fig. 5.14B) can be tailored via the diverging angle for $\theta \geq 5°$ (for full experimental spectra, see Fig. 5.12). Specifically, lower values of θ produce higher Q factors, which can be beneficial for spectrally selective chiral applications, whereas the signal modulation vanishes approaching the achiral case ($\theta = 0°$). Here, the BIC-based resonance tuning can be harnessed to precisely configure the optical system for the target chiral use case, striking a balance between Q factor and modulation as required.

Qualitatively, regarding the selective RCP/LCP transmission, the qBIC metasurface represents a maximum chiral version of previous intrinsically chiral and rotationally symmetric metasurfaces [125, 126] or, in even simpler terms, a maximum chiral analog of a bi-isotropic Pasteur medium [127]. However, while the previous examples absorb the attenuated circularly polarized waves, here, on the contrary, the qBIC metasurface reflects them with up to 80 % efficiency. This peculiar type of near-lossless maximum chirality has been previously observed in model microwave experiments [119], and its first optical realization is presented here.

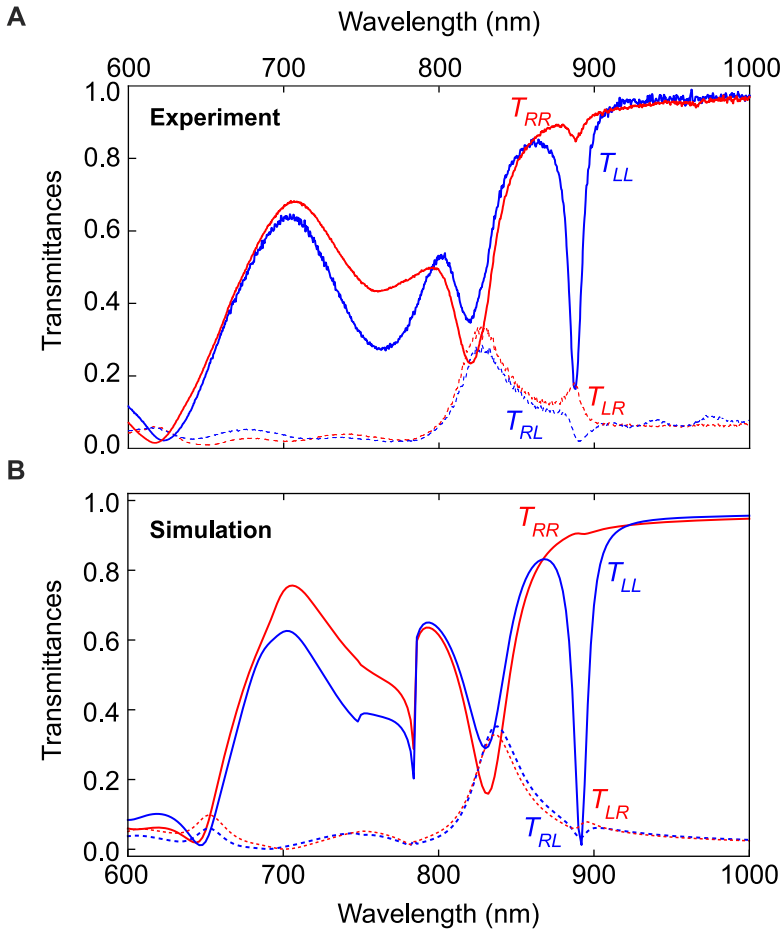

Figure 5.15.: Comparison between experiment and numerical simulations. The measured chiral response (upper panel) for a left-handed structure with an opening angle of $\theta = 8.5°$ only interacts with LCP light (blue curve T_{LL}) for which the chiral qBIC is excited. The experimental data show excellent agreement with the numerical simulations (lower panel). Scanning electron microscopy (SEM) images were used to match the lateral dimensions, atomic force microscopy scans to determine the different heights of the resonators and in-house measured amorphous silicon ellipsometry data were utilized to match the numerical simulations as precisely as possible to the measurement results. In particular, the simulations were done for a periodicity of 550 nm, heights of $h_1 = 104$ nm and $h_2 = 171$ nm, an opening angle of $\theta = 8.5°$, rod widths of $w_1 = 104$ nm and $w_2 = 157$ nm, and lengths of $L_1 = L_2 = 334$ nm.

Until now, selective reflection of circularly polarized light was attributed to the so-called chiral mirrors, which, however, inevitably invert the circular polarization of the transmitted light [128]. Recently, such mirrors have been experimentally realized as perforated silicon slabs [129] and as arrays of silicon particles of reduced symmetry hosting specific qBICs [115]. Being achiral, as all planar metasurfaces, such structures exhibit intriguing optical performance, which, however, elucidates the limits of the planar design and fabrication. Unlocking the out-of-plane dimension enables creating optical structures hosting strongly chiral qBICs selectively coupled to the light of specific helicity. Analogous resonators on a much larger scale can be arranged as Fabry-Perot cavities confined between planar chiral mirrors [130].

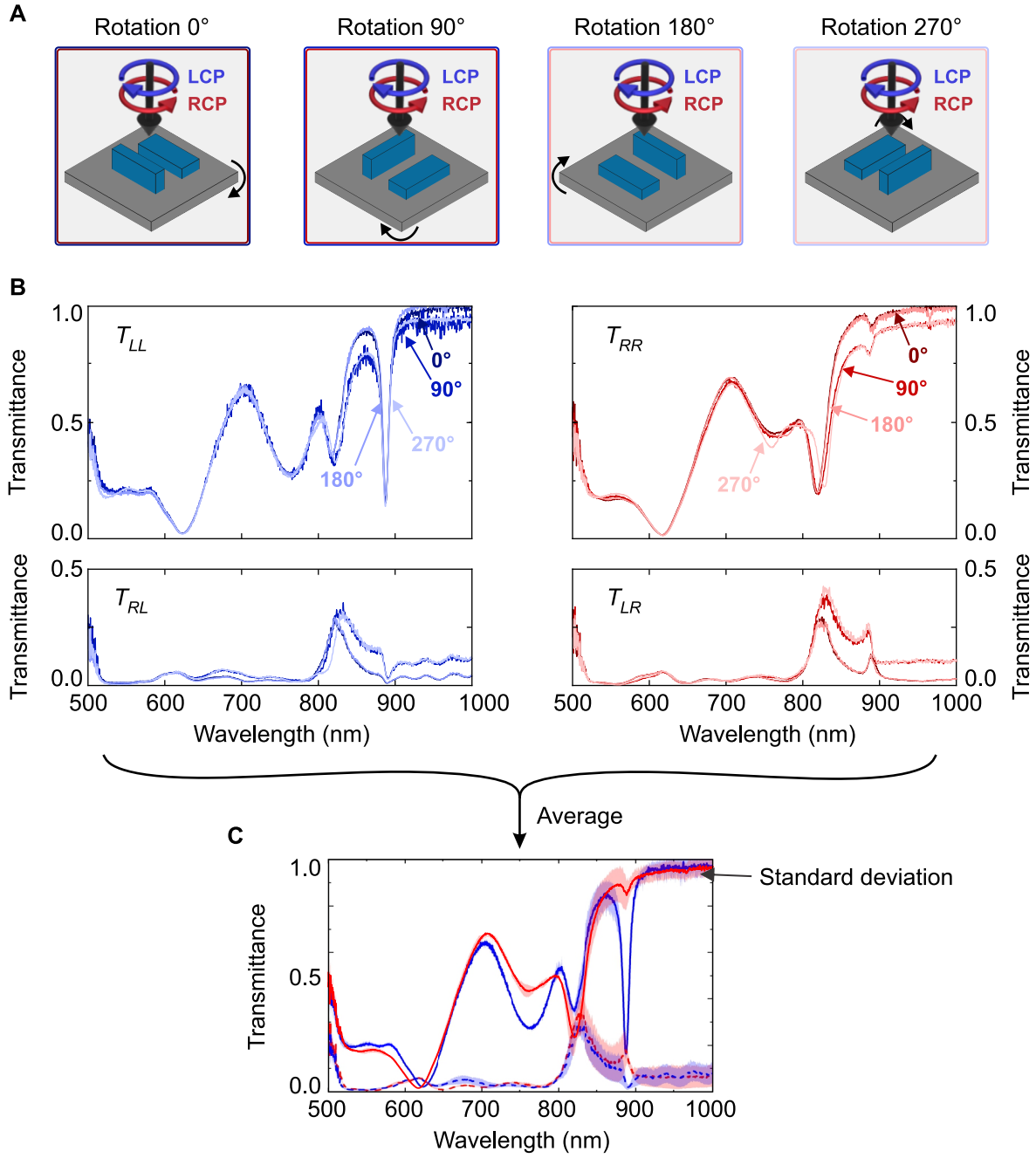

Figure 5.16.: Influence of sample rotation on the measurements of the chiral qBIC metasurfaces with chiral analyzer. (**A**) Schematic overview of the performed sample rotations during measurement. The sample was rotated four times with a 90° angle to avoid any influences of elliptical polarization or sample tilt.(**B**), (**C**) Single spectra of the four measurements (**B**) and the mean value with standard deviation (**C**) of the left-handed chiral qBIC metasurfaces with an opening angle of $\theta = 8.5°$ measured with chiral analyzer. A small signal variation in the transmittance data upon sample rotation is evident in the four single spectra for each co- and cross-polarization (T_{LL}, T_{RR}, T_{LR}, T_{RL}). The signal is identical for rotations modulo 180° (0°, 180° and 90°, 270°), which is a hint towards a small degree of elliptical polarization, which decreases the measured CD. For an influence of sample tilt, the signal should vary for all rotation angles. The small degree of elliptical polarization might be caused by the deviation of retardation (± 6%) given by the quarter wave plate and by deviation of the chiral analyzer.

In summary, a novel approach for the realization of artificial photonic materials was demonstrated through precise control over the individual meta unit height levels. In this regard, the realization of maximally chiral symmetry-broken quasi bound states in the continuum (qBICs) was shown in the optical regime. Mediated by the novel fabrication approach, the combination of two metasurface functionalities, such as the precise tailoring of the radiative quality (Q) factors and the selective coupling to circularly polarized light is unlocked to achieve several milestones.
First, out-of-plane symmetry breaking is introduced and experimentally realized as a straightforward and extremely precise symmetry-breaking mechanism for quasi-BIC metasurfaces for the first time in the visible from all-dielectric materials. The achieved asymmetries were below the resolution of most electron beam lithography systems and is only limited by fabrication intolerances [131] and layer thickness control.
Second, the full height control over individual meta units was harnessed to experimentally demonstrate chiral quasi-BIC resonances within the optical range and close to the highly relevant visible spectral range ($\lambda_{\mathrm{res}} = 900$ nm). For the first time, a record maximum chirality of $\Delta T = \pm 0.7$ in the visible range with a Q factor of 80 was shown while having full independent control over both quantities.
In contrast to previous approaches [111, 132], the fabrication approach allows for the realization of *high refractive index based multi-height metasurfaces*. Driven by the precise alignment accuracy of 5 nm, an arbitrary number of height levels can be realized, ultimately improving the efficiency of holographic metasurfaces or OAM generating metasurfaces besides chirally selective metasurfaces. In principle, the additional degree of freedom provided by the individual resonator height could unify even more different metasurface functionalities, such as filters and wavefront shapers, beam steerers etc.
Overall the fabrication approach even allows for the realization of hybrid metasurfaces, incorporating different materials within the same platform. Using this approach, PT-symmetry can be broken to realize non-Hermitian physics by interfacing loss and gain materials. Furthermore, the approach could also lead to tailored material-specific functionalities in biosensing for the material-dependent capturing of different biomolecular species.
In conclusion, the developed fabrication approach unleashes the height and the material of the resonator as accessible parameters and might not only improve the efficiencies of existing metasurfaces but could also lead to the implementation of novel systems and multi-functional metasurfaces.

6. Hexagonal boron nitride metasurfaces for low refractive index bound states in the continuum

The access to the visible spectrum and in particular the realization of all-dielectric metasurfaces with high quality (Q) factors over the full visible spectral range has been hampered so far by the lack of lossless and high refractive index materials. Nevertheless, due to the inverse correlation between the band-gap energy and the material refractive index, the utilization of low refractive index materials is unavoidable. However, for all-dielectric Mie resonant photonics, lower refractive indices are undesirable due to reduced Q factors and mode volume confinement. In this chapter, two-dimensional materials are introduced, in particular hexagonal boron nitride (hBN), along with its optical properties. In this context, symmetry-broken bound states in the continuum (BICs) are leveraged to suppress radiation losses from the low-index ($n \approx 2$) van der Waals material hBN to realize metasurfaces with high-Q resonances. In particular, the rational use of low and high refractive index materials as resonator subjects is compared from numerical simulations. Furthermore, sharp BIC resonances are demonstrated, with Q factors above 300, spanning between 400 and 1000 nm from a single hBN multilayer flake. The enhanced intrinsic electric near-fields are utilized to demonstrate second harmonic generation (SHG) with enhancement factors above 10^2. The high transparency of the material allows BIC-driven SHG for wavelengths below 400 nm, potentially even further into the ultraviolet. The results provide a theoretical and experimental framework for the implementation of low refractive index hBN as a photonically active material.

6.1. Introduction to 2D materials

Two-dimensional (2D) materials provide a valuable toolkit for solid state physics and photonics but also many more fields. As such, 2D material provide a straightforward experimental access to realize any system already known from traditional materials but also provide the possibility to create new materials with atomically sharp interfaces and novel functionalities. Owing to the compatibility of a variety of 2D materials, they are not only studied as isolated single layers but also as stacks of different 2D materials so-called van der Waals (vdW) heterostructures. In fact, the combination of different 2D materials gives rise to a plethora of applications ranging from solar cells [133, 134], detectors [135] and lasers [136, 137] in photonics to superconductivity [138, 139] and spin transistors [140] in solid state physics.

The field of two-dimensional (2D) materials started with the discovery of graphene, an atomically thick layer of carbon, by Kostya Novoselov and André Geim in 2004 [141]. Since then, graphene is well known for its linear and gap-less electronic dispersion (shown in the inset of Fig. 6.1) leading to a variety of interesting phenomena [142, 143] and is thus classified as semi-metal. Since the electronic density can be easily controlled by a gate voltage, the observation of the integer quantum Hall effect [144] in graphene proved the two-dimensional nature of graphene and was awarded with the Nobel prize in 2010. In fact, the abundance of intriguing physical phenomena and the ease of fabrication stimulated a lot of scientists to enter the field.

Mediated by the crystal structure of graphite (see Fig. 6.2A), the carbon atoms in the lattice are strongly bound to each other by the sp^2-hybridized covalent bonds within one graphene layer. In contrast to the in-plane carbon bonds, the graphene sheets inside the carbon crystal are only weakly bound to each other out of plane by van der Waals forces - a defining property for 2D materials. For that reason, single graphene sheets can be isolated by a process called mechanical exfoliation [141]. Here, thin layers of an exfoliation crystal on a tape are peeled off with another tape, which is repeated a few times until the tape is pressed on the target and graphene sheets will be left back on the substrate.

Apart from graphene, a variety of different materials have already been exfoliated as mono- (single) or multilayers. An overview of the most important 2D materials is given in Fig. 6.1. The multitude of 2D materials ranges from semimetals like graphene to semiconductors like the transition metal dichalcogenides (TMDs) and black phosphorus to insulators like hBN. Nevertheless, owing to its large band gap and thus low refractive index, hBN has either been dismissed as passive buffer layer or only been used in a small infrared (IR) spectral window in the photonics community.

However, the low absorption losses up to the ultraviolet (UV) spectral range make hBN a good candidate for its use as all-dielectric resonator material despite the low refractive index. In the following section, the underlying material and optical properties of hBN are examined.

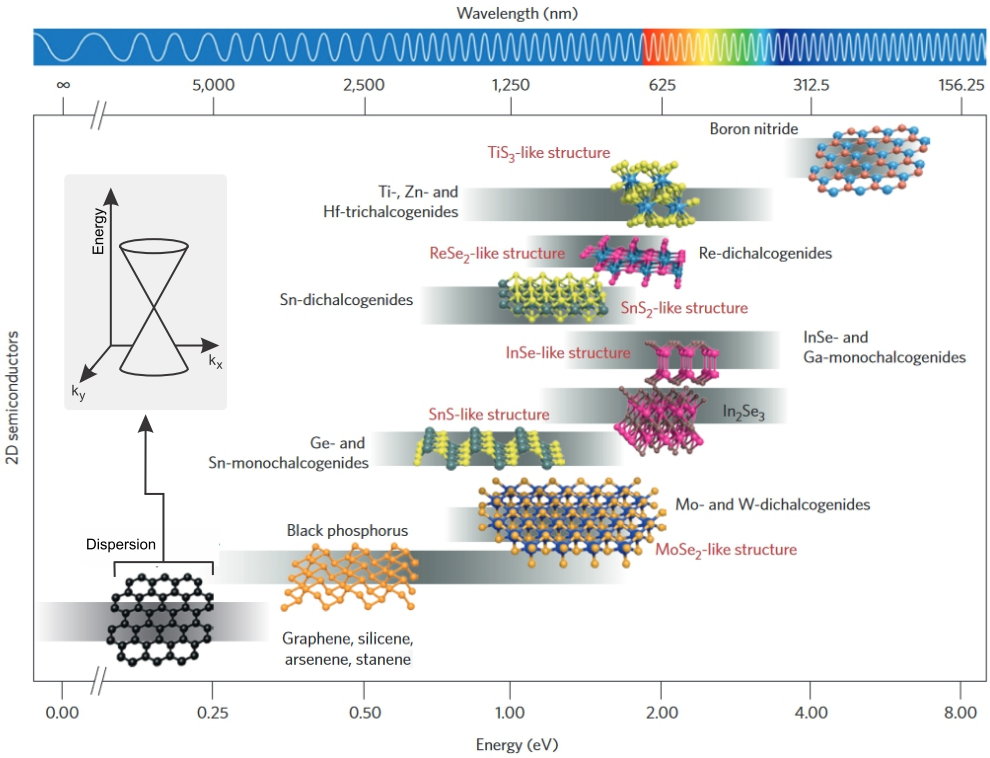

Figure 6.1.: 2D materials for nanophotonics. Overview of different 2D materials sorted by their electronic band gap. Extended ranges indicate a variance of the bandgap related to changes in the electronic structure induced by strain, different layer numbers, temperature or other effects. Inset: Electronic dispersion of graphene. Graph adapted with permission [145]. Copyright 2016, The authors, published by Springer Nature.

6.1.1. Lattice and electronic properties of hexagonal boron nitride

One of the most prominent 2D materials is hBN owing to its atomic flatness and compatibility with especially graphene as already obvious from their crystals structures depicted in Fig. 6.2A and Fig. 6.2B. Both graphite and hBN bulk crystals consist of individual layers, that are stacked on top of each other and bond together by weak van der Waals (vdW) forces. In the plane, they exhibit six atoms that are arranged in a honeycomb lattice. The main difference between hBN and graphite is the difference in the atomic composition of the materials. Although both materials exhibit similar crystal structures, hBN is composed of alternating boron and nitrogen atoms, which has severe consequences on the optical properties of the materials. On the one hand, the alternation in the arrangement of boron and nitrogen atoms enables a direct stacking on top of each other between single hBN layers.
On the other hand, the presence of another type of atom, *e.g.*, boron atoms in the nitrogen lattice, breaks the in-plane inversion symmetry and lead to an opening of a band-gap by virtue of Noether's theorem [58]. As depicted in Fig. 6.2C, the band-gap of hBN is above 5 eV (calculated with different methods, *i.e.* density functional theory (DFT) and GW method), explaining its common use as insulating layer in 2D material heterostructures. So far, hBN has only found little attention in nanophotonics.

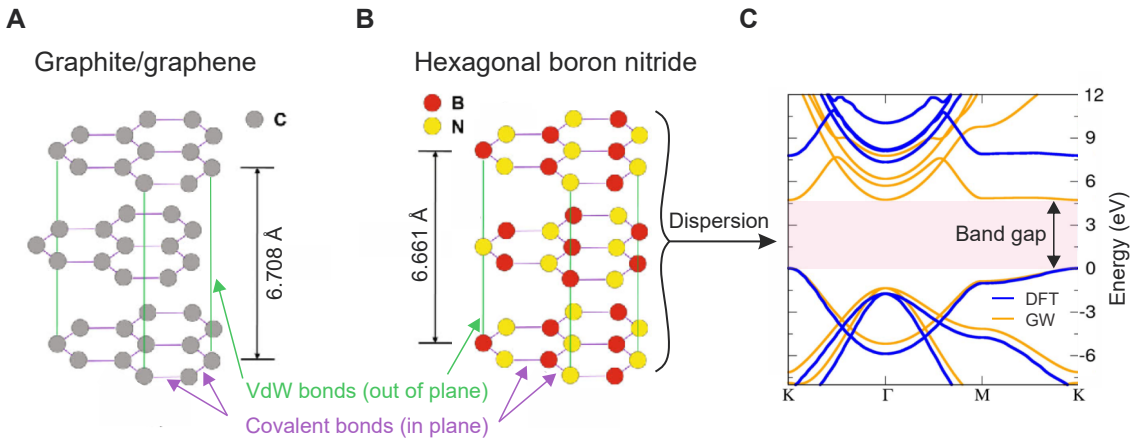

Figure 6.2.: Lattice properties and large band-gap energy in bulk hBN.(**A**) Crystal structure of graphite composed of three graphene layers. (**B**) The crystal structure of bulk hBN shows similarities to graphite only differing in the stacking order and the composition of two different nitrogen and boron atoms. (**C**) The band structure of bulk hBN shows a band-gap of more than 5 eV rendering all-dielectric nanophotonics up to the UV possible. Graphs in (**A**), (**B**) adapted with permission [146]. Copyright 2014, the Authors, published by Nature Springer. (**C**) adapted with permission [147]. Copyright 2019, Optica Publishing group.

6.2. Symmetry-broken BICs in hexagonal boron nitride

All-dielectric materials have recently emerged in nanophotonics as a key ingredient to control the properties of light at the nanoscale, such as the phase [148, 149], near-field amplitude [27, 28], directionality of light scattering [150, 151], spin [152, 153] and orbital angular momentum [132, 111] without the necessity of intrinsic material losses as for metal-based approaches. In particular, applications driven by near-field enhancement, such as biomolecular sensing, rely on high resonance quality ($Q = \lambda_{\mathrm{res}}/\mathrm{FWHM}$) factors and hence high electromagnetic near-field intensities to achieve maximum specimen sensitivity [154, 95]. The inherent correlation between the resonance quality factor and the resonator refractive index [155] known from, *e.g.*, Mie theory, thus led to the advance of all-dielectric nanophotonics based on high refractive index material systems, such as silicon (Si) [156, 157], germanium (Ge) [83, 158], or gallium phosphide (GaP) [31, 159]. Although these materials offer great properties for high-Q resonances in the near-infrared (NIR) and infrared (IR) spectral region, they are accompanied by high material-intrinsic interband absorption losses throughout the visible spectral range due to their intermediate band-gap energies. Owing to these fundamental material limitations, lossless high-index materials throughout the complete visible spectral range are lacking [40, 39, 37]. In particular, for the visible wavelength range, there exists a competition between a large band-gap for lossless photonics and a high refractive index of the material for better optical mode confinement and higher Q factors. This physical limitation is mathematically described by the Hervé equation as [39]

$$n^2 = \varepsilon = 1 + \left(\frac{A}{E_g + B}\right)^2, \tag{6.1}$$

connecting the refractive index n of the material with its band-gap energy E_g, where A (= 13.6 eV) and B (= 3.4 eV) are constants. In order to obtain high-Q resonances in the visible (400 - 800 nm) without substantial material losses, a band-gap of 3.54 eV (≈ 350 nm) is required, limiting the maximum refractive index available to $n = 2.4$ according to eq. 6.1. In fact, due to the lack of high-index and lossless materials in the visible, experimental demonstrations of high-Q resonances in the blue (*i.e.*, below 460 nm) are still missing [160]. Owing to the low refractive index of the materials and thus low quality factors of the associated Mie resonances within these materials, this avenue is mostly unexplored [161, 162].

In addition to intrinsic material loss, resonances in nanostructured dielectrics are affected by a radiative loss channel, which becomes dominant when the refractive index contrast between resonator and the environment decreases. Photonic bound states in the continuum (BICs) provide a unique pathway for tailoring radiative losses in addition to the refractive-index-based effects discussed above. Symmetry-broken quasi-BIC (for simplicity BIC) metasurfaces in particular offer precise and straightforward control over the (radiative) Q factor of the resonances via the geometrical asymmetry of the constituent unit cell building blocks [15, 16], which sets them apart from other BIC realizations based on accidental far-field destructive interference [26, 25] or strong mode coupling [22, 23]. Initiated by the versatility of the BIC concept, they open up a new avenue for the usage of low-index lossless materials, especially for realizing high-Q resonances throughout the visible spectral range.

Hexagonal boron nitride (hBN) [163], a two-dimensional (2D) van der Waals (vdW) material, exhibits an indirect band-gap of 5.95 eV [164] with an average refractive index of $n = 2.0$, potentially enabling photonic applications down to the ultraviolet (UV) range [165, 166]. So far, it was mainly used as insulating or encapsulation layer in electronics and photonics [167, 168, 169] but also found optical applications in a small spectral window (the so-called Reststrahlen band) in the IR due to its strong phononic excitations [170, 171, 172, 173]. The few demonstration in the visible have so far focused on suspended photonic crystal cavities or extended ring resonators [174, 175], which are either affected by strain effects or their large spatial extent and have not demonstrated resonances below 580 nm. Nevertheless, its optical properties along with the monocrystalline material quality and compatibility with other two-dimensional (2D) materials [176] renders hBN invaluable for the realization of photonic resonances throughout the visible as a basis for enhanced light-matter interaction, that has so far been difficult in this spectral range.

Beneficially, mechanically exfoliated bulk hBN is obtained in monocrystalline quality, thus diminishing the need for expensive deposition tools and fine engineering of deposition parameters, while simultaneously boosting the Q factors of the resonant modes due to the reduced intrinsic material losses.

In this chapter, based on a careful analysis of the underlying physics associated with symmetry-broken BICs in low index resonators, it is demonstrated that hBN-based metasurfaces with a low refractive index can support high-Q BIC resonances spanning the whole visible range. The results greatly extend the spectral operation wavelength range

for both hBN and symmetry-broken BIC metasurfaces while realizing all-dielectric high-Q resonances throughout the complete visible spectrum, especially in the blue part for the first time, all within a sample fabricated from a single hBN flake and with constant resonator height. From the numerical investigation, it is found that the resonantly enhanced electric near fields are concentrated inside the resonators. Hence, they are utilized to demonstrate a 388-fold enhancement for the material-intrinsic second harmonic generation (SHG) in bulk hBN. Because of its combination affinity with other 2D materials and general optical and chemical properties, the results provide a new paradigm for vdW nanophotonics.

6.2.1. Numerical investigation of low-index based BIC resonator systems

Owing to its large band-gap energy and thus low losses in the visible spectral regime, the goal is to obtain sharp resonances from hBN in the complete visible and NIR spectral range (400 to 1000 nm). For the description of the hBN optical properties, a model based on Sellmaier's equations is used for both the in-plane n_i and out-of-plane n_o refractive index [177] which accounts for the high material anisotropy. The resulting dispersion for both material axes is depicted on the right-hand side of Fig. 6.3 and is utilized to model the material properties in the numerical calculations.
In order to analyze symmetry-broken BIC metasurfaces composed of hBN, a double rod unit cell is employed. Here, the symmetry breaking is introduced by shortening one rod with respect to the other, such that the geometrical asymmetry is given as $\Delta L = L_2 - L_1$. For the simulation of the transmittance spectra of the metasurfaces, CST microwave Suite is used that allows for the determination of the metasurface response in the frequency domain.

In the simulation, periodic Floquet boundary conditions are utilized to calculate the scattering parameters of the metasurface yielding far-field quantities, such as reflectance and transmittance. Furthermore, plane-wave illumination is assumed and the intrinsic hBN losses are set to zero within the spectral range of interest. The corresponding numerical spectra are shown on the right-hand side of Fig. 6.3. The resonance wavelength of the BIC is controlled via changing the size scaling factor S of the unit cell, which yields spectrally dense and sharp resonances throughout the visible to the NIR region.

Indeed, hBN is an ideal candidate to realize high-Q resonances throughout the complete visible spectral range, outperforming medium refractive index materials, such as titanium dioxide (TiO_2) or silicon nitride (Si_3N_4) in the blue part of the visible spectrum due to its larger band-gap energy. Most importantly, the resonance wavelength of hBN can be scaled to the IR by further increasing the scaling factor of the unit cell as indicated in numerical simulations in Fig. 6.7C.

In order to demonstrate the feasibility of hBN as photonic resonator material for BIC resonances, in-depth numerical simulations are performed, specifically investigating the influence of the refractive index of the dielectric resonator on the near- and far-field

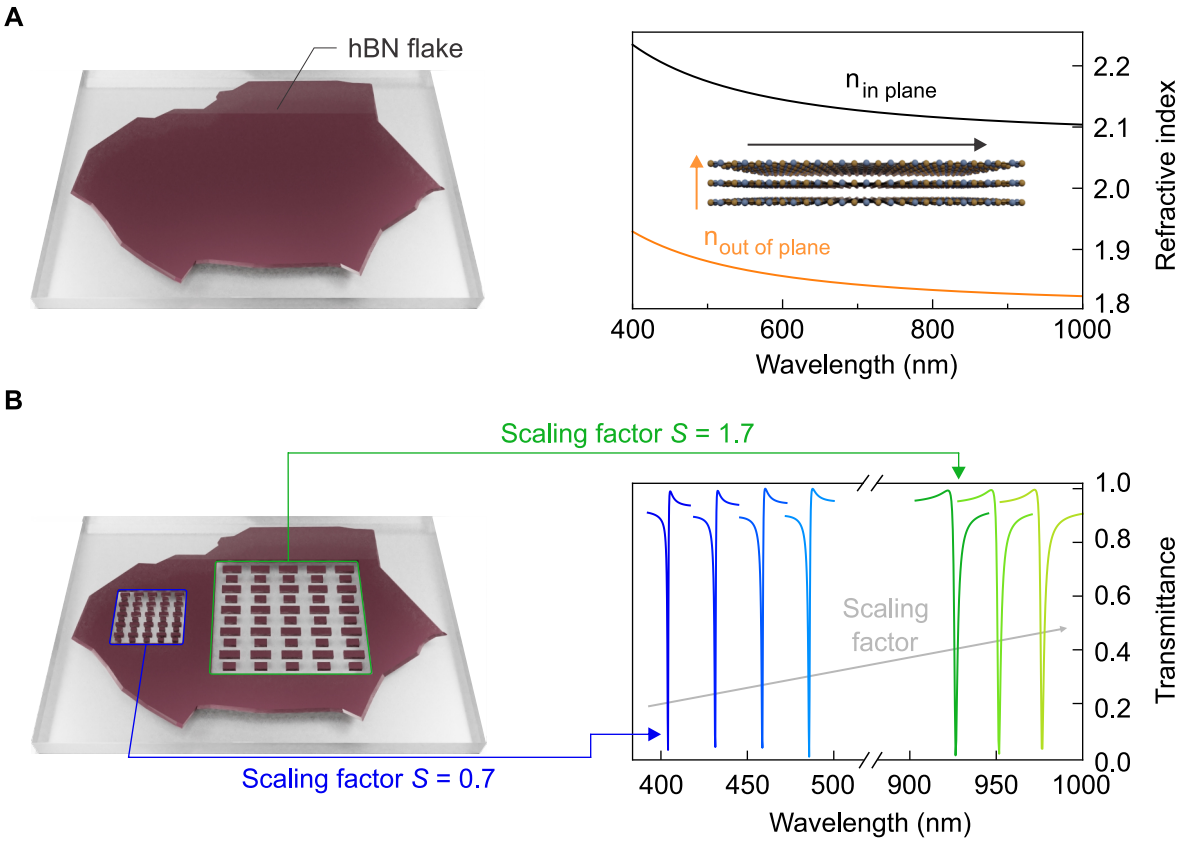

Figure 6.3.: Hexagonal boron nitride metasufaces for high-Q resonances in the visible. Left: Schematic illustration of a bulk hBN flake on an SiO_2 substrate after the exfoliation process. Right: Refractive indices calculated via the Sellmaier equations for the in-plane and out-of-plane direction. (**B**) Left: Sketch of the BIC metasurface based on a double rod unit cell in bulk hBN for different scaling factors S. Right: Numerically obtained transmittance spectra for different unit cell scaling factors showing a linear dependence between the scaling factor and the resonance wavelength.

properties of the BIC resonances. For this purpose, the BIC unit cell with asmmetric rods, as introduced above, is utilized with fixed geometry settings (periodicities $p_y = p_x + 20$ nm $= 430$ nm, resonator height $h = 150$ nm, resonator width $w = 100$ nm). The respective resonators are investigated without a substrate to suppress grating modes that could influence the properties of the BIC resonances, and the resonator material is assumed to be non-dispersive and lossless.

Most importantly, the geometrical asymmetry ΔL of the system is adjusted to the refractive index n of the resonator material to guarantee the same resonance Q factors for all refractive indices, assuming the generalized asymmetry (α) as

$$\alpha = n \cdot \Delta L. \tag{6.2}$$

Uniquely, this Q factor tunability is a defining property of symmetry-broken BIC modes without which the accurate comparison of different resonator materials is infeasible. A pronounced and spectrally isolated BIC mode can be observed for any resonator refractive index under consideration (Fig. 6.4A).

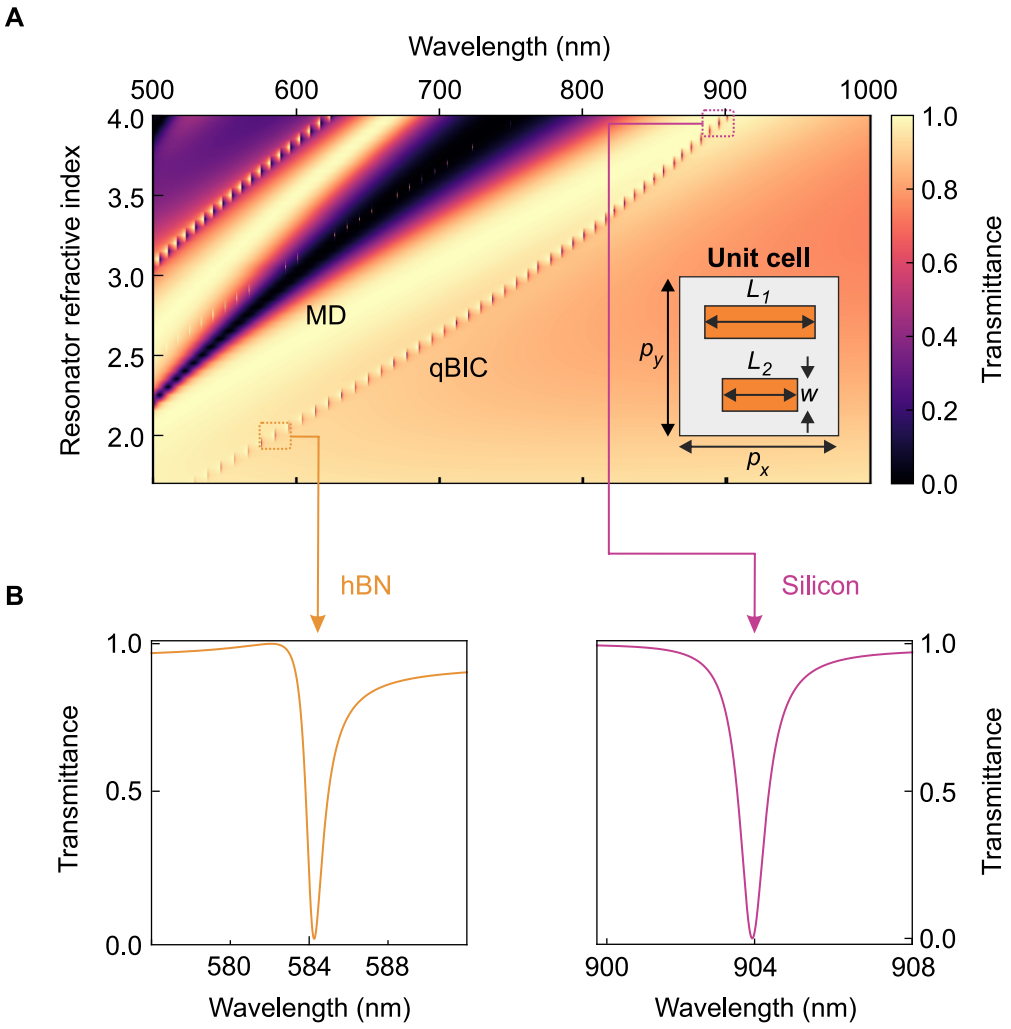

Figure 6.4.: Theoretical analysis of low-index resonators for qBIC metasurfaces. (**A**) Simulated transmittance map for different resonator refractive indices assumming the resonator materials as lossless and dispersion-less and setting $n_{\text{substrate}} = 1$. A pronounced qBIC resonance and a magnetic dipolar (MD) resonance show up. Inset: Sketch of the utilized unit cell with all relevant design parameters. (**B**) Representative qBIC spectra for an hBN- ($n = 2$) and a silicon- ($n = 4$) based resonator with compensated Q factor.

For better comparison, the $n = 4$ index as silicon representative and the $n = 2$ case for hBN are highlighted in more detail with the corresponding BIC spectra depicted in Fig. 6.4B. These BIC resonances are associated with highly enhanced near fields (Fig. 6.5A) with the typical BIC pattern of oppositely oscillating dipoles in the $x - y$ cross section. The maximum value of the electric near-field outside the structures is found to be larger for the Si resonator refractive indices, while the electric field is more distributed and less localized for the case of hBN. By investigating the decay of the normalized electric field E_{norm} away from the structures in z direction, an exponential decay is observed as depicted in Fig. 6.5B for hBN (yellow dots) and silicon (purple dots).

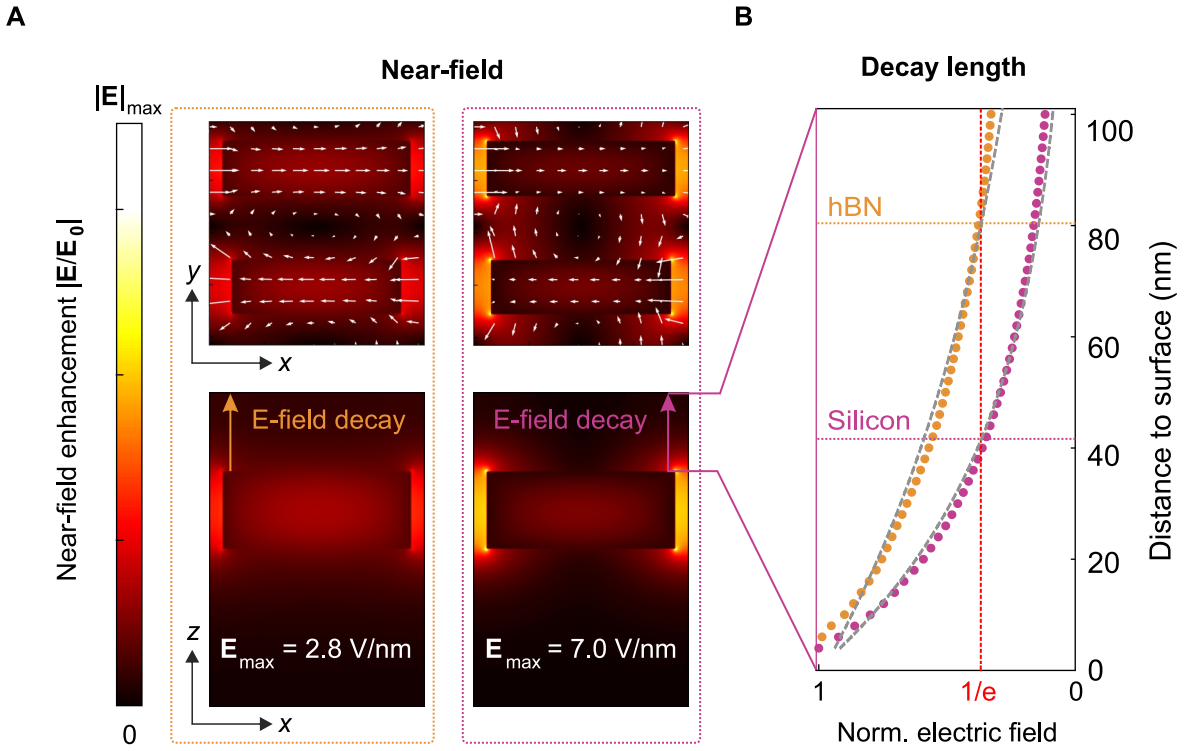

Figure 6.5.: Near-field and decay lengths for low- and high-index based resonators. (**A**) Near-field enhancement of lossless BIC resonators with $n = 2$ (hBN) on the left-hand side and $n = 4$ (silicon) on the right-hand side. (**B**) Exponential decay of the electric near-field in z direction away from the resonator surface. Fitting the exponential decay allows to determine the decay length, for which the near-field decays to $1/e$, showing roughly a factor of 2 between hBN (yellow dots) and silicon (purple dots).

By fitting these data with an exponential decay function

$$E_{\mathrm{norm}}(z) = \exp\left(-\frac{z}{\zeta}\right), \tag{6.3}$$

the decay length ζ is extracted for both resonator materials by determining the distance for which the electric field drops to $1/e$ (red dashed line in Fig. 6.5B) with respect to its value at the resonator surface. Indeed, the decay length for hBN-based resonators is roughly twice as large as for silicon-based resonators indicating that the electric near-field is more confined to the surface of the resonant structures.

For a deeper understanding of the inherent differences between low index and high index-based BIC metasurfaces, the decay length as well as the mean and maximum electric fields inside and outside the resonators are analyzed for a set of different resonator refractive indices as shown in Fig. 6.6. The investigation of the decay lengths shows a monotonous decrease towards a minimum value around 40 nm as obvious from the top panel in Fig. 6.6, related to the stronger confinements for higher index resonators.

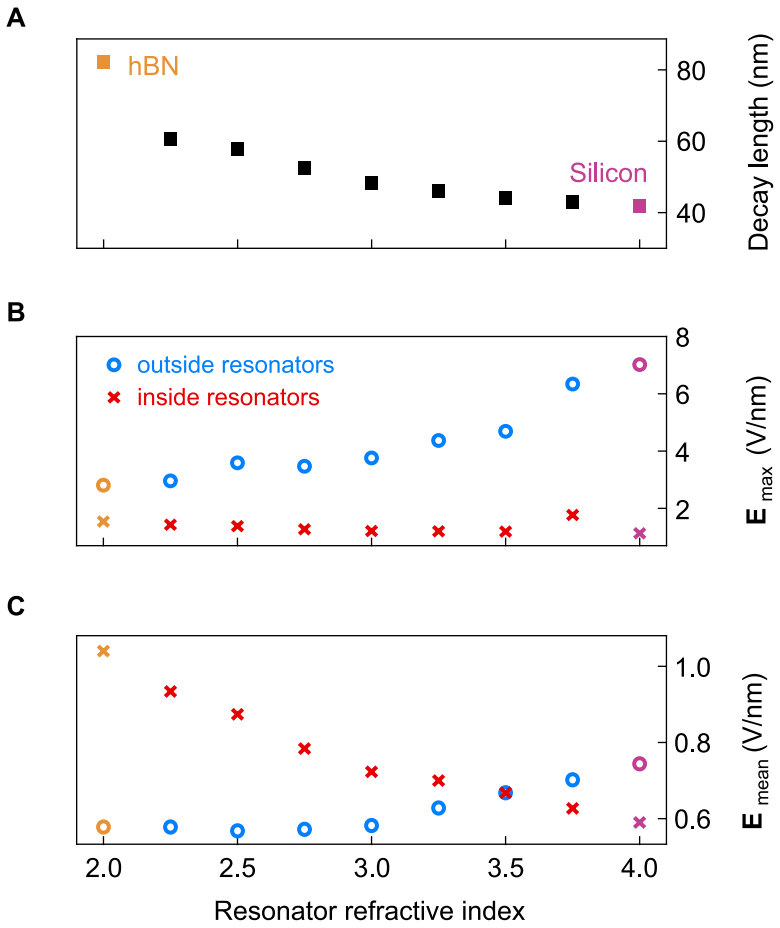

Figure 6.6.: Near-field properties for different resonator refractive indices. (**A**) Decay length for various resonator refractive indices showing a monotonous decrease towards higher indices. (**B**) Maximum electric near-field values inside (crosses) and outside (circles) the resonators showing an increase in the maximum electric fields outside the resonators towards higher refractive indices while the electric field is higher for small refractive indices inside the resonator structures. (**C**) Mean electric field inside and outside the resonators, indicating a better confinement inside (outside) the resonators for low (high) refractive index-based resonators.

For the investigation of the enhanced electric near fields, the total electric near field is split into a part inside and outside the resonators and the mean and the maximum values are calculated, as shown in the middle and bottom panel of Fig. 6.6. Notably, for increasing refractive indices, the electric fields are pushed outside the resonators as obvious from the higher maximum and mean values of the electric near-fields outside the resonators.

On the contrary, for smaller refractive indices, the electric field is rather located inside the resonators, rendering them ideally suited for material-intrinsic processes, such as high-harmonic generation or enhanced light-matter interaction utilizing hBN-encapsulated materials.

Furthermore, due to the dependence of the electric fields on the Q factor, the BIC approach enables a precise tailoring of the electric fields via controlling the geometrical

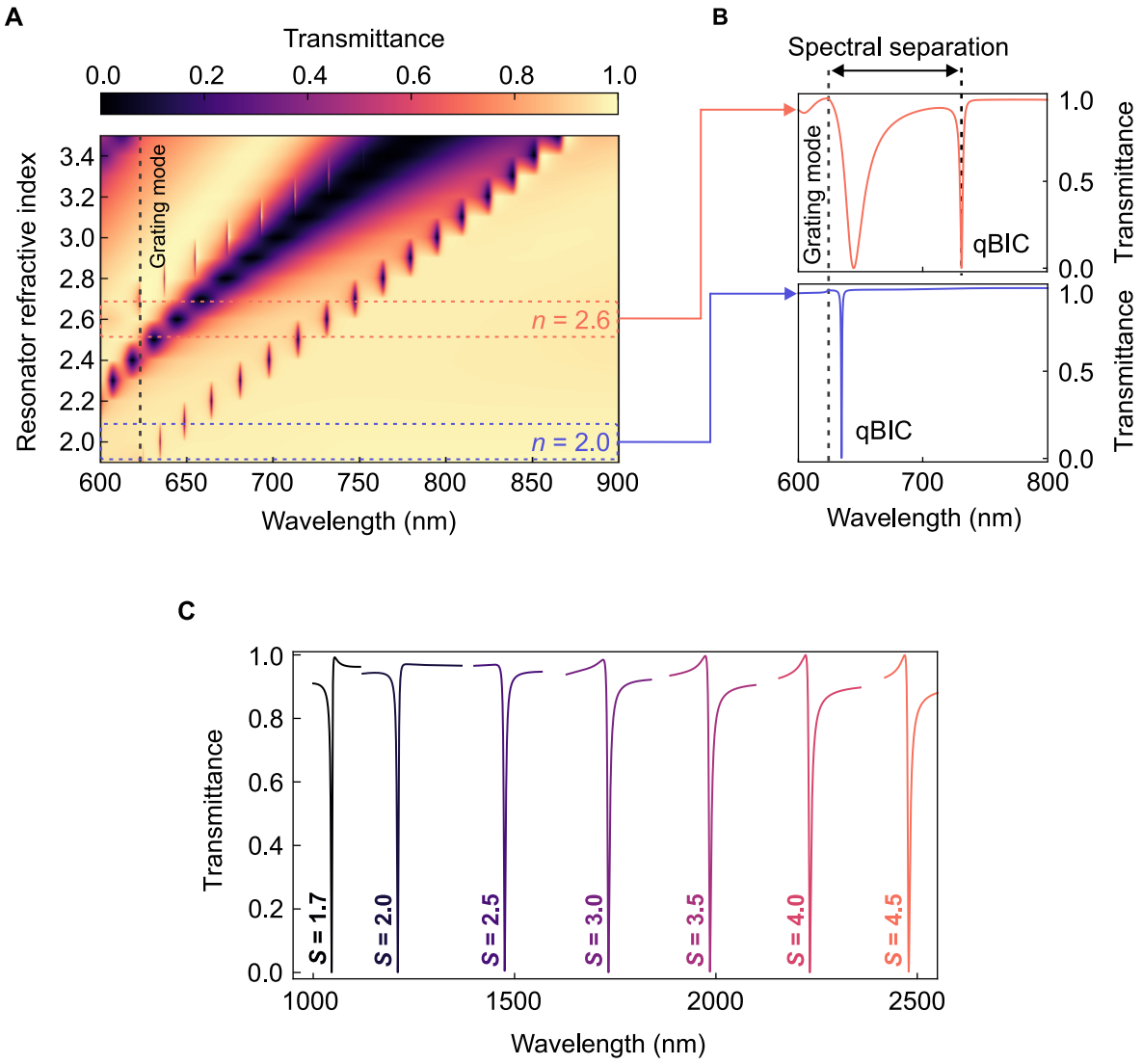

Figure 6.7.: Design constraints for low-index resonators and resonance scaling to the IR. (**A**) Simulated transmittance map taking the substrate refractive index into account $n_{\text{substrate}} = 1.45$. In experiments with a non-vacuum substrate, the grating mode (black dashed line) leads to a vanishing of the qBIC resonance for small refractive indices. (**B**) Close-up of two representative spectra showing the decreased spectral separation between the grating mode and the qBIC for small resonator refractive indices. (**C**) Scaling factor sweep for larger flake height ($h = 400$ nm) and smaller gaps ($g_x = 30$ nm) show a scaling of the qBIC resonance to the IR, up to 2500 nm.

asymmetry of the metasurface. Moreover, BIC metasurfaces based on the low-index materials reduce the requirements on the fabrication accuracy since the same asymmetries ΔL lead to lower values of the generalized asymmetry α (see eq. 6.2).

It should be noted that the metasurface design has to be carefully optimized, since the spectral separation between the grating mode and the BIC mode decreases for smaller resonator refractive indices as shown in Fig. 6.7A and Fig. 6.7B, eventually leading to a vanishing of the BIC mode.

6.2.2. Spectral tunability of hBN-based BIC metasurfaces

Owing to this reason, the design of the unit cell was carefully optimized for the experimental demonstration of hBN BIC metasurfaces. Bulk hBN flakes are mechanically exfoliated from a single crystal onto a silicon dioxide (SiO_2) substrate with a prepatterned marker system. Suitable flakes are identified via optical microscopy and their corresponding thickness is determined with a profilometer. Electron beam lithography (EBL) is utilized, followed by a gold evaporation step which is used as etching mask. A liftoff and subsequent reactive ion etching (RIE) transfers the patterns into the hBN flake, before the remaining gold is removed by wet chemistry (see Methodology for additional details on the fabrication process). Fig. 6.8A shows the corresponding gray-scale microscope image of a patterned hBN flake, where more than 20 arrays were fabricated with varying scaling factor from a single exfoliated crystal.

To characterize the hBN BIC metasurfaces, the sample was illuminated with collimated white light where the transmitted signal was collected with a 50x (NA = 0.8) objective. The light was then coupled to a multimode fiber and a grating based spectrometer where it was detected by a silicon CCD camera. In order to remove any unwanted spectral features from the sample or the beam path, all metasurface transmittance spectra were referenced to the bare SiO_2 substrate.

Fig. 6.8B shows two sharp hBN BIC resonances for a scaling factor of S = 0.65 (upper panel) and S = 1.10 (lower panel) with a spectral separation of almost 300 nm. Uniquely, the BIC resonance is spectrally isolated from any other mode, highly favorable for its usage in sensing applications or light-matter interaction enhancement. As shown in Fig. 6.8B, the tunability of the BIC resonances is demonstrated by sweeping the scaling factor S of the unit cell to obtain a comb of well pronounced BIC resonances throughout the complete visible spectrum extending from 413 nm far into the NIR range to 960 nm as depicted in Fig. 6.8E, only limited by the silicon detector efficiency. This resonance scaling corresponds to a tuning range of 1.71 eV, which is, the broadest BIC-based resonance sweep reported in the literature. Remarkably, the resonant structures are all fabricated from the same flake with a height of 200 nm and the design is optimized for a single wavelength.

To further describe the hBN BIC modes, a coupled mode theory (CMT) approach is utilized to fit the BIC lineshape and extract the corresponding modulation and Q factors for each scaling factor, as shown in 6.8C. In fact, most BIC resonances show Q factors above 200 with some of them exhibiting modulations exceeding 50 percent in the visible range. Moreover, high-Q BIC resonances are observed at 413 nm, a spectral position that has not been reported in the literature for optical resonances in all-dielectric materials.

The extracted modulations and Q factors show a maximum range between S = 0.8 and S = 1.1 while dropping off towards lower or higher scaling factors. This decrease in Q factors and resonance modulations when approaching the NIR and blue spectral range in the visible is attributed to the onset of inter-band absorption in hBN, combined with fabrication intolerances caused by the small geometrical features of the metasurface.

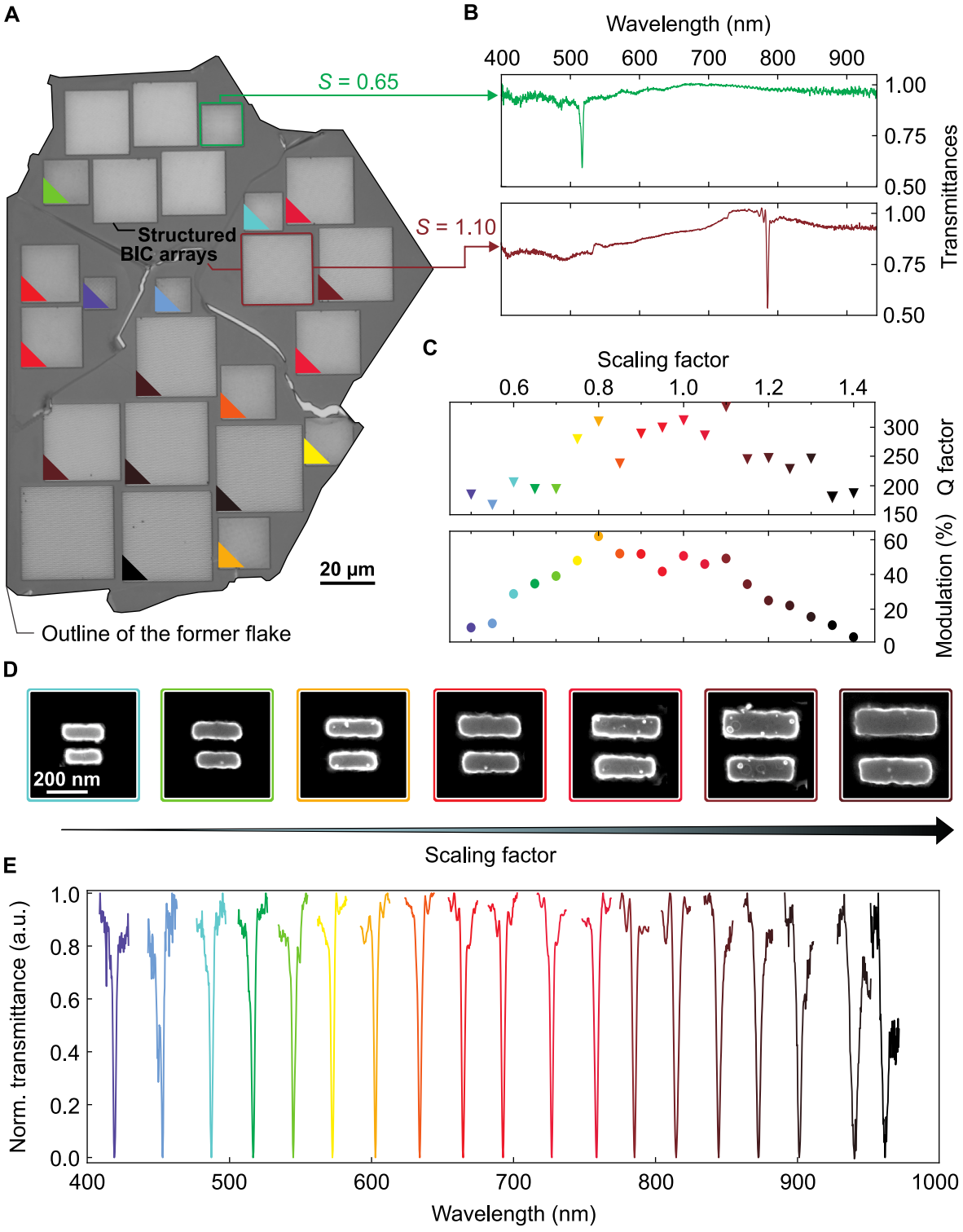

Figure 6.8.: Experimental realization of symmetry-broken qBIC metasurfaces in bulk hBN. (**A**) Optical grayscale micrograph of the former bulk hBN flake along with the nanostructured BIC arrays with different scaling factors S. (**B**) Broad range spectra showing the spectral isolation of the BIC mode for S=0.65 (green curve, upper panel) and for S=1.10 (brown curve, lower panel). (**C**) Q factors (top panel) and modulation depths (lower panel) extracted for each resonance scaling factor (shown in panel (**E**)) indicating an optimum thickness for the utilized design. (**D**) SEM micrographs of BIC unit cells with increasing scaling factor. (**E**) High-Q BIC resonances through the visible to the NIR are obtained from a single hBN flake by increasing the scaling factor of the metasurface.

Similarly, when pushing the resonances further into the NIR, the optical mode volume is mismatched with the resonator volume. Since the height of the flake is fixed, the grating mode will necessarily spectrally shift towards and over the BIC mode, thus reducing the modulation or leading to a vanishing. Nevertheless, these effects could be minimized by optimizing the hBN flake height and unit cell design for each resonance position.

Beyond the scaling of the optical resonances, the flexibility of the BIC design is demonstrated by controlling the coupling of the BIC to the far field by varying the geometrical asymmetry of the metasurface unit cell. As shown in Fig. 6.9A, the Q factor increases for smaller geometrical asymmetries until the quasi-BIC transforms into a dark BIC mode without any far-field coupling for $\Delta L = 0$ nm (black dashed curve), allowing for precise tailoring of the radiative Q factor by controlling the geometrical asymmetry. Furthermore, the straightforward control over the BIC resonance is demonstrated in Fig. 6.9B, where the excitation polarization is changed between parallel ($\mathbf{E}_{\mathrm{par}}$) and perpendicular ($\mathbf{E}_{\mathrm{per}}$) to the rods, effectively switching the resonance on and off.

As a last step, the influence of the resonator height on the BIC resonance position is asessed in Fig. 6.9C. Apart from the red-shift of the resonance induced by the increased resonator volume, the Q factor of the resonances increase towards higher flake thicknesses indicating a better mode formation.

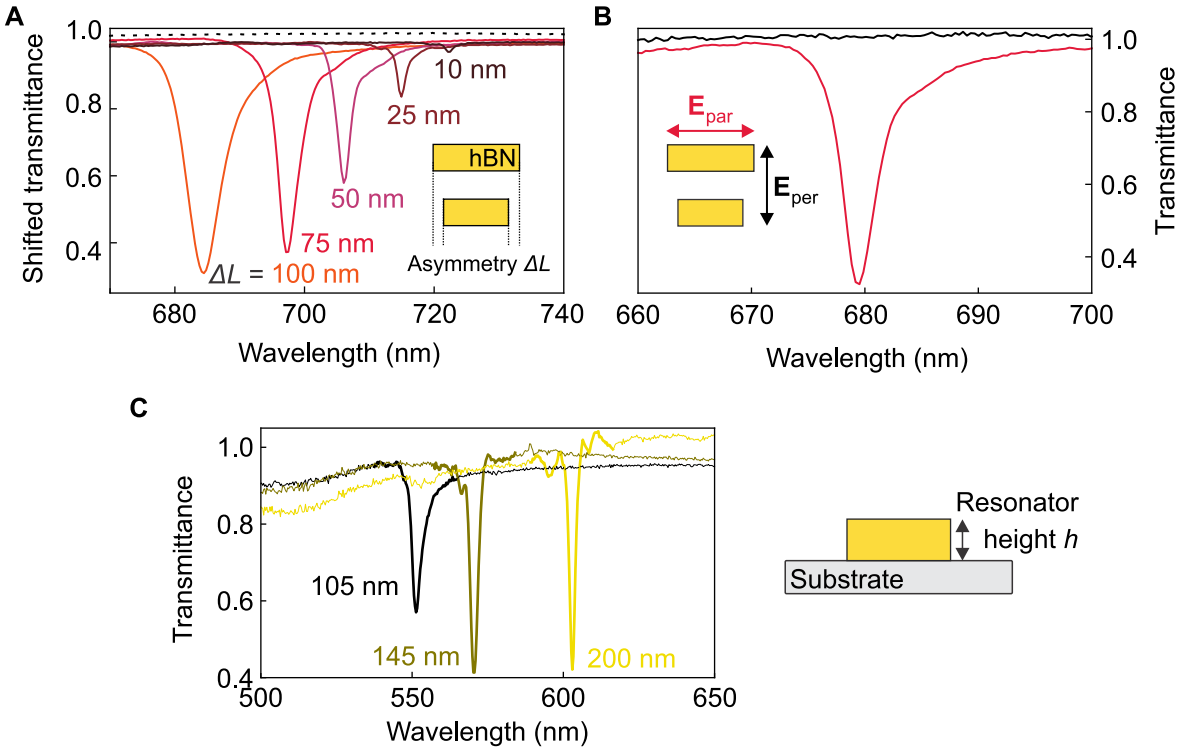

Figure 6.9.: Experimental flexibility of hBN-based qBIC metasurfaces. (**A**) Tailorability of the radiative lifetimes via the geometrical asymmetry ΔL. (**B**) Resonance control via the excitation polarization for light polarized along the long rod axis (E_{par}) or along the short rod axis ((E_{per}). (**C**) Resonance shifts induced by different resonator heights.

6.2.3. Enhanced second harmonic generation

The versatility of the BIC-based resonances is further combined with the highly enhanced electric near fields inside the low-index hBN to demonstrate BIC-enhanced second harmonic generation (SHG) in the UV (Fig. 6.10A).

As shown in Fig. 6.10B, finite-element method (FEM) simulations (COMSOL Multiphysics) are utilized to investigate the SHG efficiency for different geometrical asymmetries. As expected from BIC metasurfaces, higher Q factors are associated with larger near-field enhancements leading to a maximum SHG efficiency for the smallest geometrical asymmetry of $\Delta L = 10$ nm (dark brown curve). Since the experimental Q factors are always limited by fabrication imperfections [131], an asymmetry of $\Delta L = 75$ nm was chosen as a trade-off between a high Q factor and a good resonance modulation to guarantee a large SHG enhancement.

The SHG signal in the fabricated sample was excited using a tunable Ti:Sapphire in a transmission geometry (see Methodology). Fig. 6.11A shows the corresponding SHG signal for an hBN metasurface with $\Delta L = 75$ nm. As apparent from the graph, a 388-fold BIC-induced SHG enhancement is observed by tuning the excitation source to the two different excitation polarizations. Depending on the utilization of parallel or perpendicular polarization, the BIC design provides an "on" and "off" state of the resonance as shown in Fig. 6.9B. For incident light which is linearly polarized along the long rod axis (E_{par}, red curve in Fig. 6.10B), the BIC is excited and promotes the SHG enhancement via its highly enhanced intrinsic near fields. For light perpendicularly polarized to the long rod axis (E_{per}, black curve in Fig. 6.9B) the SHG enhancement is absent. This resonance control provides an important control mechanism to demonstrate BIC-related enhancement effects and allows for the unambiguous extraction of the SHG enhancement factor.

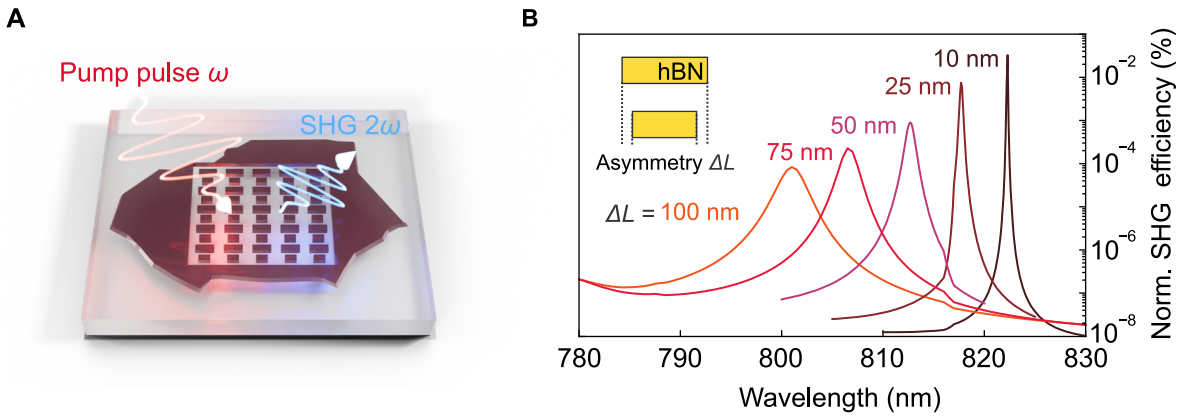

Figure 6.10.: Numerical investigation of BIC-enhanced hBN-intrinsic SHG. (**A**) Schematic setup for the SHG, where a pump pulse with frequency ω is incident on a nanostructured hBN BIC metasurface. Due to the broken inversion symmetry in bulk hBN, SHG at 2ω is observed. (**B**) Numerically obtained and normalized SHG efficiency for different geometrical asymmetries, showing the largest SHG enhancement for $\Delta L = 10$ nm.

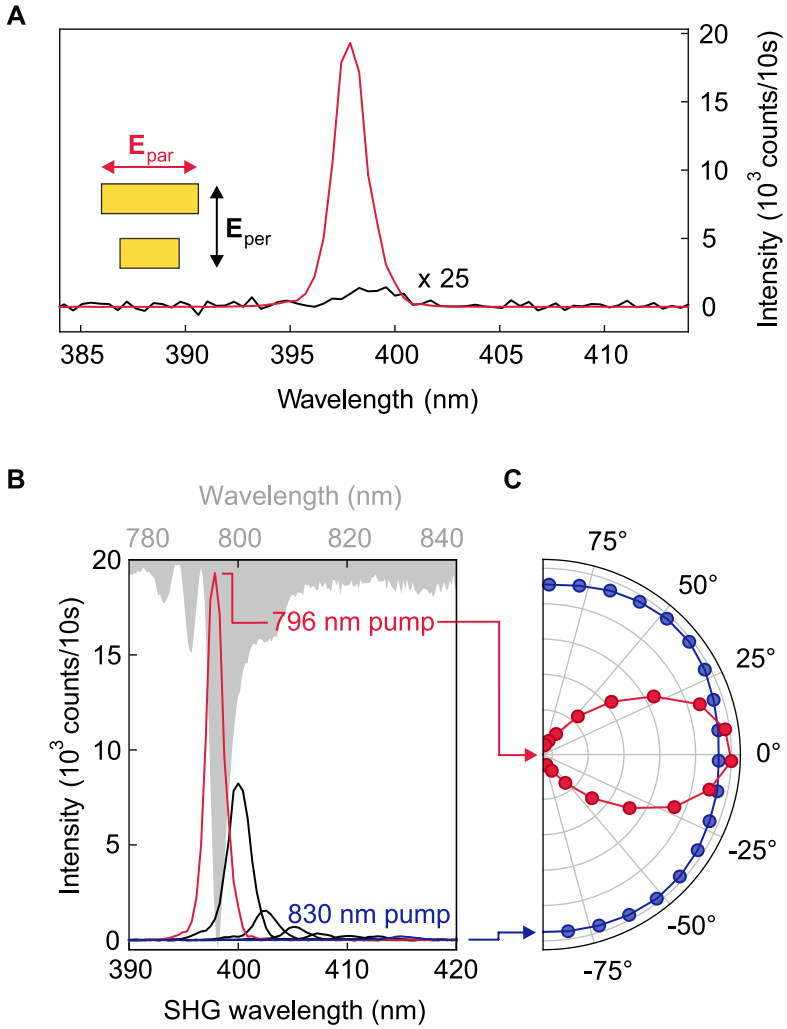

Figure 6.11.: Experimental demonstration of BIC-induced SHG enhancement in bulk hBN. (**A**) The obtained SHG intensities show a 388-fold SHG enhancement when the BIC is excited ($\mathbf{E}_{\mathrm{par}}$) compared to the absence of the BIC ($\mathbf{E}_{\mathrm{per}}$). (**B**) Pump wavelength sweep for the same metasurface as in (**A**), showing the BIC-resonant enhancement of the SHG. Gray scale: Optical transmittance spectrum of the BIC metasurface in arbitrary units. (**C**) Normalized SHG intensities for different excitation polarizations showing a full linear polarization signal for the BIC resonance and no detectable polarization for off-resonant pump.

As a further confirmation of the BIC-related SHG enhancement, the excitation wavelength is swept for the same metasurface and a clear correlation between the BIC resonance (shown in solid gray in Fig. 6.11B) and the SHG signal at twice the BIC resonance is observed for a pump wavelength of 796 nm. By spectrally shifting the excitation wavelength away from the BIC resonance towards 830 nm, the SHG also vanishes underpinning the BIC-resonant enhancement.

As a last step, the excitation polarization dependence of the SHG signal is investigated in Fig. 6.11C for resonant and off-resonant excitation. As expected, when in resonance with the BIC peak, a linearly polarized SHG signal is present, while for the off-resonant excitation the polarization dependence of the SHG signal is absent.

In summary, this chapter demonstrated how, through using the emerging concept of bound states in the continuum, radiative losses in low-index materials are efficiently suppressed. In particular, the lack of suitable materials for high-Q resonances in the visible is solved by employing hexagonal boron nitride (hBN), the backbone of 2D materials research. In this work, the benefits and drawbacks of low refractive index materials as resonator material was analyzed. It was suggested that symmetry-broken quasi bound states in the continuum (qBICs) open up a new avenue for the flexible tailoring of high-Q resonances in the visible regime. As a consequence, hBN was anticipated as photonically active resonator material and several achievements could be accomplished.

First, the fundamental physics of resonant low refractive index metasurfaces was analyzed, showing that symmetry-protected BICs are uniquely capable of producing high-Q resonances from materials with refractive indices as low as 1.9, opening up a completely new material palette for ultrasharp nanophotonics in the visible and the ultraviolet spectral regime.
Second, symmetry-protected multispectral qBICs in nanostructured hBN from a single resonator height were demonstrated with an unprecedented resonance tuning range of 1.71 eV.
Third, the first demonstration of high-Q resonances throughout the complete visible spectral range from 400 to 1000 nm was shown. Especially, the first demonstration of tunable high-Q resonances below 500 nm resonance wavelength with record-high Q factors above 200 was experimentally demonstrated that outperform metal-based and all-dielectric approaches by almost one order of magnitude [178, 179].
Finally, by leveraging the large band-gap energy of hBN, qBIC-induced second harmonic generation in bulk hBN in the UV range with an enhancement factor of 388 was shown.

In total, the implementation of hBN as resonator component not only facilitates low refractive index based photonics to obtain high-Q resonances throughout the complete visible spectral range. As such, the particular reason for the utilization of hBN as resonator subject reaches far beyond its pure optical properties. Since hBN is a key building block in van der Waals heterostructures and hosts room temperature single photon sources, the analysis paves the way for a straightforward realization of nanopatterned van der Waals metasurfaces. Since the hBN-based BIC resonances are ideally suited for enhanced light-matter interaction and quantum optics, the approach could unify the field of two-dimensional materials with nanophotonics. Ultimately, the platform could be used to realize pure hBN-based quantum photonic circuits incorporating enhanced single photon emission and detection through the platform proposed in this chapter.

7. Summary and outlook

Within this work, novel concepts and functionalities were realized for symmetry-broken BIC metasurfaces to improve and overcome physical limitations but also to provide possibilities for further advancing the system. In particular, this work tackled three fundamental limitations associated with BIC metasurfaces, such as the large spatial footprint, the restriction to resonant frequencies mainly located in the infrared spectral region, and the limitation to single functionalities. Utilizing the concepts, which were developed in this thesis, these drawbacks could be overcome and lead to new applications within the realm of high-Q resonant metasurfaces.

Radial BIC metasurface. The restriction to large geometrical footprints has held back BIC metasurfaces from practical on-chip integration. Within this project, approaches were shown how to drastically reduce the spatial extent of the symmetry-broken BIC platform down to 2 μm^2 by employing a semi-infinite annular arrangement. The radial distribution could even boost the Q factor with record values above 500 in the visible regime. The increased performance was confirmed by numerical simulations and experimental implementations, demonstrating a linear polarization-invariant response. In line with this, enhanced light-matter interaction could be proven in terms of higher biomolecular sensitivity and enhanced SHG from an evanescently coupled monolayer of $MoSe_2$. Initiated by the small footprint, the radial BIC platform enables multiplexed on-chip photonics for high harmonic light generation and biomolecular sensing based on silicon resonators. Ultimately, this platform could be used in future work for multiplexed biomolecular sensing for the retrieval of molecular fingerprints in ultra-small footprints.

Chiral BIC metasurface. The limitation of all-dielectric nanophotonics to planar structures has so far hampered the implementation of intrinsically chiral metasurfaces and the realization of multi-functional metasurfaces in general. As a solution, a novel fabrication approach for all-dielectric metasurfaces was introduced, unlocking the height of the individual resonator elements as an accessible parameter and thus enabling out-of-plane symmetry breaking. In particular, the inherent geometrical asymmetry was controlled via the constituent layer thickness and was thus only limited by the deposition accuracy, which can be controlled much more precisely compared to in-plane geometric perturbations. Using the out-of-plane symmetry breaking mechanism, two independent metasurface properties, such as the Q factor and the coupling to circularly polarized light, were independently tuned using this approach and record transmittance differences of $\Delta T = \pm 0.7$ with peak Q factors above 100 were achieved.

Above all, this approach not only unleashes the individual resonator height as accessible parameter but also provides the flexibility for the realization of hybrid metasurfaces with arbitrary number of material and height level combinations within a single meta unit. This variety highly eases the implementation of multi-functional metasurfaces but also provides straightforward access to realize non-Hermitian physics via breaking the underlying *PT*-symmetry of the system.

hBN BIC metasurface. The non-existence of lossless and high refractive index materials for the broadband visible spectral region prevents nanophotonic applications in this regime, such as enhanced light-matter interaction, efficient flat optics, or the realization of bright and clean colors beyond the RGB color gamut for novel displays. In the third project, it was shown that the concept of symmetry-broken qBICs enables the utilization of the low refractive index material hexagonal boron nitride (hBN) as photonically active material through the complete visible spectral range, where it has mostly been omitted so far. Within that work, an unprecedented resonance tuning range from 400 to 1000 nm was shown with Q factors above 200, all fabricated from a single resonator height. Promoted by the large band-gap energy of almost 6 eV, second harmonic generation (SHG) was shown in the UV with an enhancement factor of 388. Owing to the large band-gap energy, future work can be done in the UV region, potentially targeting the characteristic absorption bands of DNA, for instance. Furthermore, the platform can be used for color printing beyond the sRGB color gamut or even for spectrometer-less detectors in the visible.
Most importantly, since hBN is the backbone of 2D materials research and many intriguing quantum emitters have been found in bulk hBN, the hBN-based BIC platform is ideally suited for enhancing the single photon emission from hBN or even assembling completely hBN-based quantum circuits. In addition, owing to the combination affinity of hBN with other 2D materials, the material can be harnessed to enhance light-matter interaction in nanostructured van der Waals heterostructures.

Although the three physical limitations were investigated separately and solutions were proposed independently, future projects could investigate many combination permutations of the approaches, leading to new applications and platforms for each project. Overall, this thesis has demonstrated how to overcome the physical limitations of symmetry-broken BIC platforms and simultaneously provides a rich toolkit for the development of next generation metasurfaces.

A. Nature publisher permission

Nature Portfolio author licence policy

This policy applies to all journals published by Nature Portfolio, including Nature and the journals with "Nature" in their titles. Nature Portfolio's policies are compatible with the vast majority of funders' open access and self-archiving policies.

Nature Portfolio does not require authors of original (primary) research papers to assign the copyright of their published contributions. Authors grant Nature Portfolio an exclusive licence to publish, in return for which they can reuse their papers in their future printed work without first requiring permission from the publisher of the journal.

For non-primary articles (including articles such as Reviews, Perspectives, Comments, News & Views), copyright is retained by Springer Nature. This includes, but is not restricted to, commissioned content and all content published in the *Nature Reviews* journals.

Bibliography

[1] **F. Mitschke**. Fiber Optics. Springer Berlin Heidelberg, Berlin, Heidelberg (2016).

[2] **C. Yeh**. Fiber Optics. Academic Press (1990).

[3] **M. Mirhosseini** *et al.* High-dimensional quantum cryptography with twisted light. *New Journal of Physics* 17, 033033 (2015).

[4] **T. Ito** and **S. Okazaki**. Pushing the limits of lithography. *Nature* **406**, 1027-1031 (2000).

[5] **L. Möckl** and **W. E. Moerner**. Super-resolution Microscopy with Single Molecules in Biology and Beyond–Essentials, Current Trends, and Future Challenges. *Journal of the American Chemical Society* **142**, 17828–17844 (2020).

[6] **P. J. Larkin**. Infrared and Raman Spectroscopy, Elsevier (2018).

[7] **B. H. Stuart**. Infrared Spectroscopy: Fundamentals and Applications. John Wiley & Sons Ltd (2004).

[8] **D. Helm**, **H. Labischinski**, **G. Schallehn**, and **D. Naumann**. Classification and identification of bacteria by Fourier-transform infrared spectroscopy. *Microbiology* **137**, 69–79 (1991).

[9] **J. Lukose**, **S. Chidangil**, and **S. D. George**. Optical technologies for the detection of viruses like COVID-19: Progress and prospects. *Biosensors and Bioelectronics* **178**, 113004 (2021).

[10] **S. H. F. Scafi** and **C. Pasquini**. Identification of counterfeit drugs using near-infrared spectroscopy. *The Analyst* **126**, 2218–2224 (2001).

[11] **T. Y. Poh** *et al.* Inhaled nanomaterials and the respiratory microbiome: clinical, immunological and toxicological perspectives. *Particle and Fibre Toxicology* **15**, 46 (2018). URL: `https://doi.org/10.1186/s12989-018-0282-0`

[12] **S. A. Maier**. Plasmonics: Fundamentals and Applications. Springer US, New York, NY (2007).

[13] **K. Koshelev** and **Y. Kivshar**. Dielectric Resonant Metaphotonics (2021).

[14] **H. Hu** *et al.* Catalytic Metasurfaces Empowered by Bound States in the Continuum. *ACS Nano* **16**, 13057–13068 (2022).

[15] **K. Koshelev**, **S. Lepeshov**, **M. Liu**, **A. Bogdanov**, and **Y. Kivshar**. Asymmetric Metasurfaces with High-Q Resonances Governed by Bound States in the Continuum. *Physical Review Letters* **121**, 193903 (2018). `https://doi.org/10.`

1103/PhysRevLett.121.193903

[16] **S. I. Azzam** and **A. V. Kildishev**. Photonic Bound States in the Continuum: From Basics to Applications. *Advanced Optical Materials* **9**, 2001469 (2021).

[17] **C. W. Hsu**, **B. Zhen**, **A. D. Stone**, **J. D. Joannopoulos**, and **M. Soljačić**. Bound states in the continuum. *Nature Reviews Materials* **1**, 16048 (2016).

[18] **V.-C. Su**, **C. H. Chu**, **G. Sun**, and **D. P. Tsai**. Advances in optical metasurfaces: fabrication and applications. *Optics Express* **26**, 13148 (2018).

[19] **E. Cortés** *et al.* Optical Metasurfaces for Energy Conversion. *Chemical Reviews* (2022).

[20] **J. Valentine** *et al.* Three-dimensional optical metamaterial with a negative refractive index. *Nature* **455**, 376–379 (2008).

[21] **Y. Peng** and **S. Liao**. Bound States in Continuum and Zero-Index Metamaterials: A Review pages 1–14 (2020).

[22] **M. V. Rybin** *et al.* High-Q Supercavity Modes in Subwavelength Dielectric Resonators. *Physical Review Letters* **119**, 243901 (2017).

[23] **K. Koshelev** *et al.* Subwavelength dielectric resonators for nonlinear nanophotonics. *Science* **367**, 288–292 (2020).

[24] **C. W. Hsu** *et al.* Observation of trapped light within the radiation continuum. *Nature* **499**, 188–191 (2013).

[25] **S. T. Ha** *et al.* Directional lasing in resonant semiconductor nanoantenna arrays. *Nature Nanotechnology* **13**, 1042–1047 (2018).

[26] **A. Kodigala** *et al.* Lasing action from photonic bound states in continuum. *Nature* **541**, 196–199 (2017).

[27] **A. Tittl** *et al.* Imaging-based molecular barcoding with pixelated dielectric metasurfaces. *Science* **360**, 1105–1109 (2018).

[28] **F. Yesilkoy** *et al.* Ultrasensitive hyperspectral imaging and biodetection enabled by dielectric metasurfaces. *Nature Photonics* **13**, 390–396 (2019).

[29] **N. Bernhardt** *et al.* Quasi-BIC Resonant Enhancement of Second-Harmonic Generation in WS_2 Monolayers. *Nano Letters* **20**, 5309–5314 (2020).

[30] **Z. Liu** *et al.* Giant Enhancement of Continuous Wave Second Harmonic Generation from Few-Layer GaSe Coupled to High- Q Quasi Bound States in the Continuum. *Nano Letters* (2021).

[31] **A. P. Anthur** *et al.* Continuous Wave Second Harmonic Generation Enabled by Quasi-Bound-States in the Continuum on Gallium Phosphide Metasurfaces. *Nano Letters* **20**, 8745–8751 (2020).

[32] **X. Zhang**, **Y. Liu**, **J. Han**, **Y. Kivshar**, and **Q. Song**. Chiral emission from resonant metasurfaces. *Science* **377**, 1215–1218 (2022).

[33] **N. Muhammad**, **Y. Chen**, **C.-W. Qiu**, and **G. P. Wang**. Optical Bound

States in Continuum in MoS_2-Based Metasurface for Directional Light Emission. *Nano Letters* **21**, 967–972 (2021).

[34] **Z. Liu** *et al.* High-Q Quasibound States in the Continuum for Nonlinear Metasurfaces. *Physical Review Letters* **123**, 253901 (2019).

[35] **P. Lodahl** *et al.* Chiral quantum optics. *Nature* **541**, 473–480 (2017).

[36] **H. S. Khaliq** *et al.* Broadband Chiro-Optical Effects for Futuristic Meta-Holographic Displays. *Advanced Optical Materials* **2201175**, 2201175 (2022).

[37] **J. B. Khurgin**. Expanding the Photonic Palette: Exploring High Index Materials. *ACS Photonics* **9**, 743–751 (2022).

[38] **H. Shim**, **F. Monticone**, and **O. D. Miller**. Fundamental Limits to the Refractive Index of Transparent Optical Materials. *Advanced Materials* **33**, 2103946 (2021).

[39] **P. Hervé** and **L. Vandamme**. General relation between refractive index and energy gap in semiconductors. *Infrared Physics & Technology* **35**, 609–615 (1994).

[40] **T. S. Moss**. Relations between the Refractive Index and Energy Gap of Semiconductors. *physica status solidi (b)* **131**, 415–427 (1985).

[41] **D. G. Baranov** *et al.* All-dielectric nanophotonics: the quest for better materials and fabrication techniques. *Optica* **4**, 814 (2017).

[42] **T. T. Tran**, **K. Bray**, **M. J. Ford**, **M. Toth**, and **I. Aharonovich**. Quantum emission from hexagonal boron nitride monolayers. *Nature Nanotechnology* **11**, 37–41 (2016).

[43] **N. Mendelson** *et al.* Identifying carbon as the source of visible single-photon emission from hexagonal boron nitride. *Nature Materials* **20**, 321–328 (2021).

[44] **C. F. Bohren**. Absorption and scattering of light by small particles. Wiley-VCH Verlag GmbH & Co. KGaA, Weinheim, Germany (1983).

[45] **J. D. Jackson**. Classical Electrodynamics. Wiley-VCH Verlag GmbH & Co. KGaA, Weinheim, Germany (1998).

[46] **G. Mie**. Beiträge zur Optik trüber Medien, speziell kolloidaler Metallösungen. *Annalen der Physik* **330**, 377–445 (1908).

[47] **A. C. Overvig**, **S. C. Malek**, **M. J. Carter**, **S. Shrestha**, and **N. Yu**. Selection rules for quasibound states in the continuum. *Physical Review B* **102**, 035434 (2020).

[48] **J. P. Gordon**, **H. J. Zeiger**, and **C. H. Townes**. The Maser—New Type of Microwave Amplifier, Frequency Standard, and Spectrometer. *Physical Review* **99**, 1264–1274 (1955).

[49] **H. Walther**, **B. T. H. Varcoe**, **B.-G. Englert**, and **T. Becker**. Cavity quantum electrodynamics. *Reports on Progress in Physics* **69**, 1325–1382 (2006).

[50] **J. von Neuman** and **E. P. Wigner**. Über merkwürdige diskrete Eigenwerte.

Phys. Z. **30**, 465–467 (1929).

[51] **L. Huang** *et al.* Sound trapping in an open resonator. *Nature Communications* **12**, 4819 (2021).

[52] **H. Tong**, **S. Liu**, **M. Zhao**, and **K. Fang**. Observation of phonon trapping in the continuum with topological charges. *Nature Communications* **11**, 5216 (2020).

[53] **C. Linton** and **P. McIver**. Embedded trapped modes in water waves and acoustics. *Wave Motion* **45**, 16–29 (2007).

[54] **Y. Plotnik** *et al.* Experimental Observation of Optical Bound States in the Continuum. *Physical Review Letters* **107**, 183901 (2011).

[55] **D. C. Marinica**, **A. G. Borisov**, and **S. V. Shabanov**. Bound States in the Continuum in Photonics. *Physical Review Letters* **100**, 183902 (2008).

[56] **J. Lee** *et al.* Observation and Differentiation of Unique High-Q Optical Resonances Near Zero Wave Vector in Macroscopic Photonic Crystal Slabs. *Physical Review Letters* **109**, 067401 (2012).

[57] **D. R. Abujetas**, **J. Olmos-Trigo**, and **J. A. Sánchez-Gil**. Tailoring Accidental Double Bound States in the Continuum in All-Dielectric Metasurfaces. *Advanced Optical Materials* **10**, 2200301 (2022).

[58] **E. Noether**. Invariante Variationsprobleme. *Nachrichten von der Gesellschaft der Wissenschaften zu Göttingen* (1918).

[59] **S. D. Krasikov**, **A. A. Bogdanov**, and **I. V. Iorsh**. Nonlinear bound states in the continuum of a one-dimensional photonic crystal slab. *Physical Review B* **97**, 224309 (2018). `https://doi.org/10.1103/PhysRevB.97.224309`

[60] **G. Q. Moretti** *et al.* Introducing a Symmetry-Breaking Coupler into a Dielectric Metasurface Enables Robust High-Q Quasi-BICs. *Advanced Photonics Research* **2200111**, 2200111 (2022).

[61] **U. Fano**. Effects of Configuration Interaction on Intensities and Phase Shifts. *Physical Review* **124**, 1866–1878 (1961).

[62] **M. F. Limonov**, **M. V. Rybin**, **A. N. Poddubny**, and **Y. S. Kivshar**. Fano resonances in photonics. *Nature Photonics* **11**, 543–554 (2017).

[63] **B. Gallinet**, **J. Butet**, and **O. J. F. Martin**. Numerical methods for nanophotonics: standard problems and future challenges. *Laser & Photonics Reviews* **9**, 577–603 (2015).

[64] **J. Labille** *et al.* Finite Element Methods for Computational Nano-optics. In Encyclopedia of Nanotechnology, pages 837–843. Springer Netherlands, Dordrecht (2012).

[65] Polyteknik. https://www.polyteknik.com/technology/electron-beam-evaporation/, accessed Sept. 2022.

[66] Oxford Instruments https://plasma.oxinst.com/technology/pecvd?gclid=CjwKC

Ajws8yUBhA1EiwAi_tpEUCtDea09PzMwTUs2BdqYFJEr5BQ8DaTWXrDWoY qFhwI6fWLuiHhihoCD_8QAvD_BwE, accessed Sept. 2022

[67] **T. Taniguchi** and **K. Watanabe**. Synthesis of high-purity boron nitride single crystals under high pressure by using Ba–BN solvent. *Journal of Crystal Growth* **303**, 525–529 (2007).

[68] **K. S. Novoselov** and **A. H. Castro Neto** Two-dimensional crystals-based heterostructures: materials with tailored properties. *Phys Scr.* **T146**, 014006 (2012). http://dx.doi.org/10.1088/0031-8949/2012/T146/014006

[69] **A. Splendiani** *et al.* Emerging Photoluminescence in Monolayer MoS_2. *Nano Letters* **10**, 1271–1275 (2010).

[70] **E. M. Alexeev** *et al.* Imaging of Interlayer Coupling in van der Waals Heterostructures Using a Bright-Field Optical Microscope. *Nano Letters* **17**, 5342–5349 (2017).

[71] **L. Sortino**. Enhanced light-matter interaction in atomically thin semiconductors coupled with dielectric nano-antennas. Ph.D. thesis, University of Sheffield (2020).

[72] **T. Weber**. Strong light-matter interaction in nanoscopic transition metal dichalcogenide metasurfaces using optical bound states in the continuum. Master thesis, Ludwig-Maximilians-University Munich (2021).

[73] **S. Fan**, **W. Suh**, and **J. D. Joannopoulos**. Temporal coupled-mode theory for the Fano resonance in optical resonators. *Journal of the Optical Society of America A* **20**, 569 (2003).

[74] **Wonjoo Suh**, **Zheng Wang**, and **Shanhui Fan**. Temporal coupled-mode theory and the presence of non-orthogonal modes in lossless multimode cavities. *IEEE Journal of Quantum Electronics* **40**, 1511–1518 (2004).

[75] **L. Kühner** *et al.* Radial bound states in the continuum for polarization-invariant nanophotonics. *Nature Communications* **13**, 4992 (2022).

[76] **R. W. Boyd**. Nonlinear Optics. Academic Press, 3rd editio edition (2008).

[77] **Y. Jahani** *et al.* Imaging-based spectrometer-less optofluidic biosensors based on dielectric metasurfaces for detecting extracellular vesicles. *Nature Communications* **12**, 3246 (2021).

[78] **D. Lin**, **P. Fan**, **E. Hasman**, and **M. L. Brongersma**. Dielectric gradient metasurface optical elements. *Science* **345**, 298–302 (2014).

[79] **A. Silva** *et al.* Performing Mathematical Operations with Metamaterials. *Science* **343**, 160–163 (2014).

[80] **K. Koshelev**, **G. Favraud**, **A. Bogdanov**, **Y. Kivshar**, and **A. Fratalocchi**. Nonradiating photonics with resonant dielectric nanostructures. *Nanophotonics* **8**, 725–745 (2019).

[81] **R. Parker**. Resonance effects in wake shedding from parallel plates: Some

experimental observations. *Journal of Sound and Vibration* **4**, 62–72 (1966).

[82] **N. Cumpsty** and **D. Whitehead**. The excitation of acoustic resonances by vortex shedding. *Journal of Sound and Vibration* **18**, 353–369 (1971).

[83] **A. Leitis** *et al.* Angle-multiplexed all-dielectric metasurfaces for broadband molecular fingerprint retrieval. *Science Advances* **5**, eaaw2871 (2019).

[84] **M.-s. Hwang** *et al.* Ultralow-threshold laser using super-bound states in the continuum. *Nature Communications* **12**, 4135 (2021).

[85] **C. Huang** *et al.* Ultrafast control of vortex microlasers. *Science* **367**, 1018–1021 (2020).

[86] **K. Koshelev** *et al.* Nonlinear Metasurfaces Governed by Bound States in the Continuum. *ACS Photonics* **6**, 1639–1644 (2019).

[87] **V. Kravtsov** *et al.* Nonlinear polaritons in a monolayer semiconductor coupled to optical bound states in the continuum. *Light: Science and Applications* **9** (2020).

[88] **Z. F. Sadrieva** *et al.* Experimental observation of a symmetry-protected bound state in the continuum in a chain of dielectric disks. *Physical Review A* **99**, 053804 (2019).

[89] **E. N. Bulgakov** and **A. F. Sadreev**. Nearly bound states in the radiation continuum in a circular array of dielectric rods. *Physical Review A* **97**, 033834 (2018).

[90] **H.-L. Han**, **H. Li**, **H.-b. Lü**, and **X. Liu**. Trapped modes with extremely high quality factor in a circular array of dielectric nanorods. *Optics Letters* **43**, 5403 (2018).

[91] **J. Liu** *et al.* A solid-state source of strongly entangled photon pairs with high brightness and indistinguishability. *Nature Nanotechnology* **14**, 586–593 (2019).

[92] **A. Sayanskiy**, **M. Danaeifar**, **P. Kapitanova**, and **A. E. Miroshnichenko**. All-Dielectric Metalattice with Enhanced Toroidal Dipole Response. *Advanced Optical Materials* **6**, 1800302 (2018).

[93] **B. Špačková**, **P. Wrobel**, **M. Bocková**, and **J. Homola**. Optical Biosensors Based on Plasmonic Nanostructures: A Review. *Proceedings of the IEEE* **104**, 2380–2408 (2016).

[94] **A. A. Yanik** *et al.* Seeing protein monolayers with naked eye through plasmonic Fano resonances. *Proceedings of the National Academy of Sciences* **108**, 11784–11789 (2011).

[95] **Y. Yang**, **I. I. Kravchenko**, **D. P. Briggs**, and **J. Valentine**. All-dielectric metasurface analogue of electromagnetically induced transparency. *Nature Communications* **5**, 5753 (2014).

[96] **H. Altug**, **S.-H. Oh**, **S. A. Maier**, and **J. Homola**. Advances and applications of nanophotonic biosensors. *Nature Nanotechnology* **17**, 5–16 (2022).

[97] **A. Ndao** *et al.* Differentiating and quantifying exosome secretion from a single cell using quasi-bound states in the continuum. *Nanophotonics* **9**, 1081–1086 (2020).

[98] **B. Tilmann** *et al.* Nanostructured amorphous gallium phosphide on silica for nonlinear and ultrafast nanophotonics. *Nanoscale Horizons* **5**, 1500–1508 (2020).

[99] **C. Janisch** *et al.* Extraordinary Second Harmonic Generation in Tungsten Disulfide Monolayers. *Scientific Reports* **4**, 5530 (2015).

[100] **K. L. Seyler** *et al.* Electrical control of second-harmonic generation in a WSe_2 monolayer transistor. *Nature Nanotechnology* **10**, 407–411 (2015).

[101] **L. Sortino** *et al.* Enhanced light-matter interaction in an atomically thin semiconductor coupled with dielectric nano-antennas. *Nature Communications* **10**, 5119 (2019).

[102] **L. Kang**, **H. Bao**, and **D. H. Werner**. Efficient second-harmonic generation in high Q-factor asymmetric lithium niobate metasurfaces. *Optics Letters* **46**, 633 (2021).

[103] **S. Psilodimitrakopoulos** *et al.* Twist Angle mapping in layered WS_2 by Polarization-Resolved Second Harmonic Generation. *Scientific Reports* 9, 14285 (2019).

[104] **K. Wang** *et al.* Strain tolerance of two-dimensional crystal growth on curved surfaces. *Science Advances* **5**, eaav4028 (2019).

[105] **Y. Hu** *et al.* All-dielectric metasurfaces for polarization manipulation: principles and emerging applications. *Nanophotonics* **9**, 3755–3780 (2020).

[106] Metalenz PolarEyes https://www.metalenz.com/, accessed Sept. 2022

[107] **N. Yu** and **F. Capasso**. Flat optics with designer metasurfaces. *Nature materials* **13**, 139–50 (2014).

[108] **B. Luk'yanchuk** *et al.* The Fano resonance in plasmonic nanostructures and metamaterials. *Nature Materials* **9**, 707–715 (2010).

[109] **P. Genevet** and **F. Capasso**. Holographic optical metasurfaces: a review of current progress. *Reports on Progress in Physics* **78**, 024401 (2015).

[110] **R. Zhao**, **L. Huang**, and **Y. Wang**. Recent advances in multi-dimensional metasurfaces holographic technologies. *PhotoniX* **1**, 20 (2020).

[111] **H. Ren** *et al.* Complex-amplitude metasurface-based orbital angular momentum holography in momentum space. *Nature Nanotechnology* **15**, 948–955 (2020).

[112] **K. Weber** *et al.* Single mode fiber based delivery of OAM light by 3D direct laser writing. *Optics Express* **25**, 19672 (2017).

[113] **L. A. Warning** *et al.* Nanophotonic Approaches for Chirality Sensing. *ACS Nano* **15**, 15538–15566 (2021).

[114] **M. Schäferling**. Chiral Nanophotonics, volume 205 (2017).

[115] **T. Shi** *et al.* Planar chiral metasurfaces with maximal and tunable chiroptical response driven by bound states in the continuum. *Nature Communications* **13**, 4111 (2022).

[116] **A. Overvig**, **N. Yu**, and **A. Alù**. Chiral Quasi-Bound States in the Continuum. *Physical Review Letters* **126**, 073001 (2021).

[117] **M. V. Gorkunov**, **A. A. Antonov**, and **Y. S. Kivshar**. Metasurfaces with Maximum Chirality Empowered by Bound States in the Continuum. *Physical Review Letters* **125**, 93903 (2020).

[118] **J. Dixon**, **M. Lawrence**, **D. R. Barton**, and **J. Dionne**. Self-Isolated Raman Lasing with a Chiral Dielectric Metasurface. *Physical Review Letters* **126**, 123201 (2021).

[119] **M. V. Gorkunov**, **A. A. Antonov**, **V. R. Tuz**, **A. S. Kupriianov**, and **Y. S. Kivshar**. Bound States in the Continuum Underpin Near-Lossless Maximum Chirality in Dielectric Metasurfaces. *Advanced Optical Materials* **9**, 2100797 (2021).

[120] **A. S. Kupriianov** *et al.* Metasurface Engineering through Bound States in the Continuum. *Physical Review Applied* **12**, 014024 (2019).

[121] **C. Menzel**, **C. Rockstuhl**, and **F. Lederer**. Advanced Jones calculus for the classification of periodic metamaterials. *Physical Review A* **82**, 053811 (2010).

[122] **I. Fernandez-Corbaton**, **M. Fruhnert**, and **C. Rockstuhl**. Objects of Maximum Electromagnetic Chirality. *Physical Review X* **6**, 031013 (2016).

[123] **A. V. Kondratov** *et al.* Extreme optical chirality of plasmonic nanohole arrays due to chiral Fano resonance. *Physical Review B* **93**, 195418 (2016).

[124] **J. Kaschke**, **J. K. Gansel**, **J. Fischer**, and **M. Wegener**. Metamaterial Circular Polarizers Based on Metal N-Helices. In CLEO: 2013, volume 20, page QTu1A.4. OSA, Washington, D.C. (2013).

[125] **M. V. Gorkunov**, **A. A. Ezhov**, **V. V. Artemov**, **O. Y. Rogov**, and **S. G. Yudin**. Extreme optical activity and circular dichroism of chiral metal hole arrays. *Applied Physics Letters* **104**, 221102 (2014).

[126] **K. Tanaka** *et al.* Chiral Bilayer All-Dielectric Metasurfaces. *ACS Nano* **14**, 15926–15935 (2020).

[127] **I. V. Lindell**, **A. Sihvola**, **S. A. Tretyakov**, and **A. J. Viitanen**. Electromagnetic Waves in Chiral and Bi-Isotropic Media. Artech House Publishers (1994).

[128] **E. Plum** and **N. I. Zheludev**. Chiral mirrors. *Applied Physics Letters* **106**, 221901 (2015).

[129] **B. Semnani**, **J. Flannery**, **R. Al Maruf**, and **M. Bajcsy**. Spin-preserving chiral photonic crystal mirror. *Light: Science & Applications* **9**, 23 (2020).

[130] **K. Voronin**, **A. S. Taradin**, **M. V. Gorkunov**, and **D. G. Baranov**. Single-

Handedness Chiral Optical Cavities. *ACS Photonics* **9**, 2652–2659 (2022).

[131] **J. Kühne** *et al.* Fabrication robustness in BIC metasurfaces. *Nanophotonics* **10**, 4305–4312 (2021).

[132] **H. Ren** *et al.* Metasurface orbital angular momentum holography. *Nature Communications* **10**, 2986 (2019).

[133] **M. Bernardi**, **M. Palummo**, and **J. C. Grossman**. Extraordinary Sunlight Absorption and One Nanometer Thick Photovoltaics Using Two-Dimensional Monolayer Materials. *Nano Letters* **13**, 3664–3670 (2013).

[134] **M.-l. Tsai** *et al.* Monolayer MoS_2 Heterojunction Solar. *ACS Nano* **8**, 8317–8322 (2014).

[135] **G. Konstantatos**. Current status and technological prospect of photodetectors based on two-dimensional materials. *Nature Communications* **9**, 5266 (2018).

[136] **S. Wu** *et al.* Monolayer semiconductor nanocavity lasers with ultralow thresholds. *Nature* **520**, 69–72 (2015).

[137] **Y. Ye** *et al.* Monolayer excitonic laser. *Nature Photonics* **9**, 733–737 (2015).

[138] **Y. Cao** *et al.* Unconventional superconductivity in magic-angle graphene superlattices. *Nature* **556**, 43–50 (2018).

[139] **H. Zhou**, **T. Xie**, **T. Taniguchi**, **K. Watanabe**, and **A. F. Young**. Superconductivity in rhombohedral trilayer graphene. *Nature* **598**, 434–438 (2021).

[140] **A. Dankert** and **S. P. Dash**. Electrical gate control of spin current in van der Waals heterostructures at room temperature. *Nature Communications* **8**, 16093 (2017).

[141] **K. S. Novoselov** *et al.* Electric Field Effect in Atomically Thin Carbon Films. *Science* **306**, 666–669 (2004).

[142] **K. S. Novoselov** *et al.* A roadmap for graphene. *Nature* **490**, 192–200 (2012).

[143] **A. K. Geim** and **K. S. Novoselov**. The rise of graphene. *Nature Materials* **6**, 183–191 (2007).

[144] **K. v. Klitzing**, **G. Dorda**, and **M. Pepper**. New Method for High-Accuracy Determination of the Fine-Structure Constant Based on Quantized Hall Resistance. *Physical Review Letters* **45**, 494–497 (1980).

[145] **A. Castellanos-Gomez**. Why all the fuss about 2D semiconductors? *Nature Photonics* **10**, 202–204 (2016).

[146] **K. K. Kim**, **S. M. Kim**, and **Y. H. Lee**. A new horizon for hexagonal boron nitride film. *Journal of the Korean Physical Society* **64**, 1605–1616 (2014). `https://link.springer.com/article/10.3938/jkps.64.1605`

[147] **F. Ferreira**, **A. J. Chaves**, **N. M. R. Peres**, and **R. M. Ribeiro**. Excitons in hexagonal boron nitride single-layer: a new platform for polaritonics in the ultraviolet. *Journal of the Optical Society of America B* **36**, 674 (2019). `https:`

//doi.org/10.1364/JOSAB.36.000674

[148] **M. Lawrence** *et al.* High quality factor phase gradient metasurfaces. *Nature Nanotechnology* **15**, 956–961 (2020).

[149] **A. C. Overvig** *et al.* Dielectric metasurfaces for complete and independent control of the optical amplitude and phase. *Light: Science & Applications* **8**, 92 (2019).

[150] **T. Shibanuma** *et al.* Experimental Demonstration of Tunable Directional Scattering of Visible Light from All-Dielectric Asymmetric Dimers. *ACS Photonics* **4**, 489–494 (2017).

[151] **J. Karst** *et al.* Electrically switchable metallic polymer nanoantennas. *Science* **374**, 612–616 (2021).

[152] **Y. Bao** *et al.* On-demand spin-state manipulation of single-photon emission from quantum dot integrated with metasurface. *Science Advances* **6**, 1–8 (2020).

[153] **P. Huo** *et al.* Photonic Spin-Multiplexing Metasurface for Switchable Spiral Phase Contrast Imaging. *Nano Letters* **20**, 2791–2798 (2020).

[154] **W. Wang** and **X. Ma**. Achieving extreme light confinement in low-index dielectric resonators through quasi-bound states in the continuum. *Optics Letters* **46**, 6087 (2021).

[155] **D. G. Baranov** *et al.* All-dielectric nanophotonics: the quest for better materials and fabrication techniques. *Optica* **4**, 814 (2017).

[156] **I. Staude** and **J. Schilling**. Metamaterial-inspired silicon nanophotonics. *Nature Photonics* **11**, 274–284 (2017).

[157] **C. Wu** *et al.* Spectrally selective chiral silicon metasurfaces based on infrared Fano resonances. *Nature Communications* **5**, 3892 (2014).

[158] **S. Campione** *et al.* Broken Symmetry Dielectric Resonators for High Quality Factor Fano Metasurfaces. *ACS Photonics* **3**, 2362–2367 (2016).

[159] **L. Hüttenhofer** *et al.* Metasurface Photoelectrodes for Enhanced Solar Fuel Generation. *Advanced Energy Materials* **11**, 2102877 (2021).

[160] **S. Sun** *et al.* All-Dielectric Full-Color Printing with TiO_2 Metasurfaces. *ACS Nano* **11**, 4445–4452 (2017).

[161] **C. Zhang** *et al.* Low-loss metasurface optics down to the deep ultraviolet region. *Light: Science & Applications* **9**, 55 (2020).

[162] **K.-H. Kim** and **I.-P. Kim**. Quasi-bound states in the continuum with high Q -factors in metasurfaces of lower-index dielectrics supported by metallic substrates. *RSC Advances* **12**, 1961–1967 (2022).

[163] **B. Gil**, **G. Cassabois**, **R. Cusco**, **G. Fugallo**, and **L. Artus**. Boron nitride for excitonics, nano photonics, and quantum technologies. *Nanophotonics* **9**, 3483–3504 (2020).

[164] **G. Cassabois**, **P. Valvin**, and **B. Gil**. Hexagonal boron nitride is an indirect bandgap semiconductor. *Nature Photonics* **10**, 262–266 (2016).

[165] **F. Ferreira**, **A. J. Chaves**, **N. M. R. Peres**, and **R. M. Ribeiro**. Excitons in hexagonal boron nitride single-layer: a new platform for polaritonics in the ultraviolet. *Journal of the Optical Society of America B* **36**, 674 (2019).

[166] **H. Xu** *et al.* Magnetically tunable and stable deep-ultraviolet birefringent optics using two-dimensional hexagonal boron nitride. *Nature Nanotechnology* (2022).

[167] **C. R. Dean** *et al.* Boron nitride substrates for high-quality graphene electronics. *Nature Nanotechnology* **5**, 722–726 (2010).

[168] **S. J. Haigh** *et al.* Cross-sectional imaging of individual layers and buried interfaces of graphene-based heterostructures and superlattices. *Nature Materials* **11**, 764–767 (2012).

[169] **Y. Liu** *et al.* Van der Waals heterostructures and devices. *Nature Reviews Materials* **1**, 16042 (2016).

[170] **M. Autore** *et al.* Boron nitride nanoresonators for phonon-enhanced molecular vibrational spectroscopy at the strong coupling limit. *Light: Science & Applications* **7**, 17172–17172 (2018).

[171] **M. Autore** *et al.* Enhanced Light–Matter Interaction in ^{10}B Monoisotopic Boron Nitride Infrared Nanoresonators. *Advanced Optical Materials* **9**, 2001958 (2021).

[172] **J. D. Caldwell** *et al.* Photonics with hexagonal boron nitride. *Nature Reviews Materials* **4**, 552–567 (2019).

[173] **J. D. Caldwell** *et al.* Sub-diffractional volume-confined polaritons in the natural hyperbolic material hexagonal boron nitride. *Nature Communications* **5**, 5221 (2014).

[174] **S. Kim** *et al.* Photonic crystal cavities from hexagonal boron nitride. *Nature Communications* **9**, 2623 (2018).

[175] **J. E. Fröch**, **Y. Hwang**, **S. Kim**, **I. Aharonovich**, and **M. Toth**. Photonic Nanostructures from Hexagonal Boron Nitride. *Advanced Optical Materials* **7**, 1–6 (2019).

[176] **A. K. Geim** and **I. V. Grigorieva**. Van der Waals heterostructures. *Nature* **499**, 419–425 (2013).

[177] **Y. Rah**, **Y. Jin**, **S. Kim**, and **K. Yu**. Optical analysis of the refractive index and birefringence of hexagonal boron nitride from the visible to near-infrared. *Optics Letters* **44**, 3797 (2019).

[178] **X. Zhu** *et al.* Beyond Noble Metals: High Q -Factor Aluminum Nanoplasmonics. *ACS Photonics* **7**, 416–424 (2020).

[179] **M. Semmlinger** *et al.* Vacuum Ultraviolet Light-Generating Metasurface. *Nano Letters* **18**, 5738–5743 (2018).

Acknowledgments

At first, I would like to thank my supervisor **Dr. Andreas Tittl** for hosting me as PhD student, all the fruitful but also funny discussions we had and, above all, the great time that I had working with you in times which were marked by long periods of home office and very limited access to the lab.
At the same time, I would like to thank **Prof. Dr. Stefan Maier** for bringing me back to nanophotonics research and hosting me in my second PhD year, all the stimulating discussions and help I got from you but also for teaching me how to do a scientific two-minute elevator pitch.
Furthermore, I would like to thank **Prof. Dr. Thomas Weitz** for hosting me during my first PhD year and introducing me to the topic of charge transport in 2D materials. Although our ways have parted, I will always remember the nice time I had with you and your group.
Next, I would like to thank my PhD commitee, especially **Prof. Dr. Thomas Taubner**, **Prof. Dr. Jan von Delft**, **Dr. Bert Nickel**, **Prof. Dr. Tim Liedl**, and **Prof. Dr. Joachim Rädler**.
Another big thanks goes my seat mates, in particular **Thomas Weber**, **Dr. Ludwig Hüttenhofer**, and **Fabian Geisenhof** for always listening to my complaints and cheering with me in cases of success, but also thanks to all my other office mates **Benjamin Tilmann**, **Haiyang Hu**, **Dr. Juan Wang**, **Dr. Alexander Berestennikov**, **Andrea Mancini**, **Dr. Jakob Lenz**, **Dr. Felix Winterer**, **Lisa Walter**, and **Anna Seiler**.
I would like to thank **Dr. Luca Sortino** and **Dr. Fedja Wendisch** for your scientific support but also for your PhD wisdoms and the great evenings we had after some hard working days.
Moreover, I would like to thank the whole Chair in Hybrid Nanosystems for the great working atmosphere, it has been a pleasure working and doing non-work related stuff with you.
A big thanks goes to **Martina Edenhofer**, **Reinhold Rath**, and **Namvar Jahanmehr**, who kept the whole institute running very smoothly and who always had an open ear when things were not running smoothly.
Another big thanks goes to **Philipp Altpeter** and **Christian Obermayer** for your consultation with nanofabrication and cleanroom advices in general, which has probably saved me months of work.
Additionally, I would like to thank all of our collaborators during my PhD thesis, in particular **Prof. Dr. Yuri Kivshar**, **Dr. Haoran Ren**, **Dr. Maxim Gorkunov**, **Dr. Rodrigo Berté**, and **Alexander Antonov**.

Without my family and friends, this thesis would not have been possible. So, I would deeply like to thank my family and friends for their love and support, special thanks goes to **Dr. Julian Karst** who was not only the best friend and host one can imagine but also for cheering me up when things did not work at all.
Finally, I would like to thank my wonderful wife **Lea**, who has patiently endured all my emotional highs and lows and always gave me the confidence and power to move on with all the research.